SIMULATION OF TRANSMEMBRANE POTENTIAL PROPAGATION IN THREE DIMENSIONAL VENTRICULAR TISSUE USING ALIEV PANFILOV MODEL

A THESIS SUBMITTED TO
THE GRADUATE SCHOOL OF NATURAL AND APPLIED SCIENCES
OF
MIDDLE EAST TECHNICAL UNIVERSITY

MIRMEHDI SEYEDEBRAHIMI

IN PARTIAL FULFILLMENT OF THE REQUIREMENTS
FOR
THE DEGREE OF MASTER OF SCIENCE
IN
BIOMEDICAL ENGINEERING

FEBRUARY 2015

Approval of the thesis:

SIMULATION OF TRANSMEMBRANE POTENTIAL PROPAGATION IN THREE DIMENSIONAL VENTRICULAR TISSUE USING ALIEV PANFILOV MODEL

submitted by **MIRMEHDI SEYEDEBRAHIMI** in partial fulfillment of the requirements for the degree of **Master of Science in Biomedical Engineering Department, Middle East Technical University** by,

Prof. Dr. Gülbin Dural Ünver
Dean, Graduate School of **Natural and Applied Sciences** _____

Prof. Dr. Hakan I. Tarman
Head of Department, **Biomedical Engineering** _____

Assoc. Prof. Dr. Yeşim Serinağaoglu Doğrusöz
Supervisor, **Electrical and Electronics Eng. Dep., METU** _____

Dr. Ferhat Eyyüpkoca
Co-supervisor, **Ankara Sincan Dr. Nafiz Körez Devlet Hastanesi Kardiyoloji Kliniği** _____

Examining Committee Members:

Assist. Prof. Dr. Ergin Tönük
Mechanical Engineering Department, METU _____

Assoc. Prof. Dr. Yeşim Serinağaoğlu Doğrusöz
Electrical and Electronics Engineering Department, METU _____

Assoc. Prof. Dr. Lale Alatan
Electrical and Electronics Engineering Department, METU _____

Prof. Dr. Tolga Çiloğlu
Electrical and Electronics Engineering Department, METU _____

Assoc. Prof. Dr. Çağdaş D. Son
Biology Department, METU _____

Date: _____

I hereby declare that all information in this document has been obtained and presented in accordance with academic rules and ethical conduct. I also declare that, as required by these rules and conduct, I have fully cited and referenced all material and results that are not original to this work.

Name, Last Name: MIRMEHDI SEYEDEBRAHIMI

Signature :

ABSTRACT

SIMULATION OF TRANSMEMBRANE POTENTIAL PROPAGATION IN THREE DIMENSIONAL VENTRICULAR TISSUE USING ALIEV PANFILOV MODEL

Seyedebrahimi, MirMehdi
M.S., Department of Biomedical Engineering
Supervisor : Assoc. Prof. Dr. Yeşim Serinağaoglu Doğrusöz
Co-Supervisor : Dr. Ferhat Eyyüpkoca

February 2015, 104 pages

Heart is a muscular tissue that circulates blood through the circulatory system, and has a role in providing oxygen and nutrition to body organs and removal of wastes from them. Any disorder in the function of this organ can lead to severe diseases, and even death. Thus, characterization of these diseases and their mechanisms is important, and helps the clinicians diagnose, treat, and predict these diseases. The contraction of heart muscle is dependent on its electrical activity, and determination of this activity could provide information about the functional state of the heart. Majority of these diseases can be diagnosed using clinical methods ranging from 12-lead electrocardiography (ECG) to open surgery. However, most of these methods either are considered to be invasive, or provides information at limited spatio-temporal resolution. Moreover, ethical permission problems, and fast electro-physiological changes constrain their application for investigation purposes.

The main objective of this study is to mathematically model the heart's electrical activity for understanding the details of its function, and developing methods for prediction, diagnosis and treatment of various heart diseases. High spatio-temporal resolution maps, simple application could supply researchers and physicians necessary information that could not be acquired with other methods. In this work, we modelled the electrical activity of the heart in the three dimensional (3D) ventricular geometry based on transmembrane potential (TMP) distributions using anatomical information of the heart such as; property of myocardium, fiber orientation. etc. We also use Aliev-Panfilov model to describe electrical activity of the heart at tissue level, which focuses on the potential wavefront propagation. In this model, it is also possible to include the anisotropy of the heart muscle. We first focused on anisotropic tissue assumption, comparing it to isotropic assumption of cardiac tissue. Second, effects of fiber orientation variance representing geometrical errors was investigated. Third, we suggested a new method for simple, and reliable modelling of electrical activity of the heart by transferring cardiac information from a known heart to an unknown one. Then, using similar method of simulation, 3 dimensional mapping of TMP distribution and propagation of different functional states of the heart was simulated. First, propagation in the normal heart tissue based on normal and ectopic heart beats were modelled. Second, based on action potential morphology changes in a tissue with ischemia, we derived ischemic weight values and equation parameters for our model. Then by introducing ischemic regions on the ventricular geometry and using ischemic tissue properties and weight values, we simulated TMP distribution and propagation in ventricular geometry with partial ischemia. Finally, by introducing an abnormal conduction pathway, a heart with a pre-excitation disorder called Wolf-Parkinson-White syndrome was simulated. Our results of simulation were similar to previous clinical and simulation models. It was also shown that isotropic assumption of cardiac tissue can affect TMP simulation results significantly. This alteration was shown chiefly in TMP wavefront propagation velocity, TMP potential value of each points and more importantly action potential duration. In contrast, it was shown that DTI based images in spite of additional micro-structural errors are the most reliable method for simulating the electrical activity of the heart.

Keywords: Aleiv Panfilov Model, Anisotropy, Transmembrane Potential, Normal and Ischemic Tissue, Wolf-Parkinson-White, Ectopic arrhythmia

ÖZ

ALİEV-PANFİLOV MODELİ KULLANILARAK 3 BOYUTLU VENTRİKULER DOKUDA TRANSMEMBRAN POTANSİYELLERİNİN YAYILIMININ SİMÜLASYONU

Seyedebrahimi, MirMehdi
Yüksek Lisans, Biyomedikal Mühendisliği Bölümü
Tez Yöneticisi : Doç. Dr. Yeşim Serinağaoglu Doğrusöz
Ortak Tez Yöneticisi : Dr. Ferhat Eyyüpkoca

Şubat 2015 , 104 sayfa

Kalp, dolaşım sistemi yoluyla kanı vücutta dolaştıran bir kas dokusudur ve vücuttaki organların oksijen ve besin ihtiyacını karşıladığı gibi atıklarını uzaklaştırmak ile görevlidir. Kalp fonksiyonundaki herhangi bir bozukluk, birçok hastalığa ve hatta ölüme sebep olabilir. Bu nedenle, bu hastalıkların ve mekanizmalarının tanımlanması klinisyenlerin bu hastalıkları teşhisi, tahmini ve tedavisine yardımcı olması açısından önemlidir. Kalp kasının kasılmaları elektrik aktivitesine bağlıdır ve bu elektriksel aktivitenin belirlenmesi kalbin fonksiyonel durumu hakkında bilgi verebilir. Bu hastalıkların çoğunluğunun teşhisi , 12 kanallı EKG ‘den açık kalp ameliyatına kadar birçok klinik metotla sağlanabilir. Ancak, bu yöntemlerin invaziv olduğu ve sınırlı uzay-zamansal çözünürlükte bilgi sağladığı düşünülmektedir. Ayrıca, etik izin sorunları ve elektro-fizyolojik değişimlerinin hızlı olması, araştırma amaçlı olan uygulamaları sınırlandırmaktadır.

Bu çalışmanın temel amacı; fonksiyonunun detaylarını anlamak için kalbin elektriksel aktivitesinin matematiksel modellemesini yapmak ve çeşitli kalp hastalıklarının tahmin, tanı ve tedavi yöntemleri geliştirmektir. Yüksek uzay-zamansal çözünürlükteki haritalar, araştırmacılara ve hekimlere diğer yöntemler ile ulaşamadıkları gerekli bilgileri sağlayabilir. Bu çalışmada, transmembran potansiyel (TMP) dağılımlarına dayanarak ve miyokard özelliği, lif oryantasyonu gibi kalbin anatomik bilgilerini kullanarak, kalbin elektriksel aktivitesinin üç boyutlu (3D) ventriküler geometrisini modelledik. Ayrıca, kalbin elektriksel aktivitesini doku düzeyinde tanımlamak için potansiyel dalga şekli yayılmasına dayanan Aliev –Panfilov modelini kullandık. Bu modelde, kalp kasının eşyönsüzlüğünü dahil edilmesi de mümkündür. İlk olarak, eşyönsüz doku varsayımına odaklanarak kardiyak doku eşyönlü varsayımı ile karşılaştırdık. Sonrasında fiber oryantasyon varyansı ifade eden geometrik hataların etkileri araştırdık. Daha sonra, kolaylık için yeni bir metod önerdik ve bir kalbin fiber yönlerinin bilgilerini kullanarak başka bir kalbin elektiriksel aktivitesini tahmin ettik. Ardından, benzer simülasyon yöntemi kullanarak, TMP dağıtımının 3 boyutlu haritalaması ve kalbin farklı fonksiyonel durumunun yayılımı simüle edildi. Önce, normal ve ektopik kalp atımına dayalı normal kalp dokusunda yayılım modellenmiştir. Daha sonra, iskemik bir dokudaki aksiyon potentisellerinin morfolojik değişimlerine dayanarak, modelimiz için iskemik ağırlık değerleri ve denklem parametreleri türettik. Ve ardından, ventroküler dokuya iskemik bir bölge tanımlayarak ve iskemik dokunun özelliklerini ve ağırlık değerlerini kullanarak TMP dağılımı ve yayılımını bu dokuda simüle ettik. Son olarak, anormal bir iletim yolunu tanıtarak, Wolf-Parkinson-White sendromu olarak tanımlanan bir ön-uyarı bozukluğu olan kalp simüle edildi. Bu araştırmadaki simülasyon sonuçlarının daha önceki klinik metod ve simülasyon modelleri ile benzer olduğunu gözlemledik. Aynı zamanda kalp dokusunun izotropik varsayımının TMP simülasyon sonuçlarına önemli ölçüde etki edebildiğini gördük. Bu değişiklik öncelikle TMP dalga şeklinin yayılma hızında, her bir noktadaki TMP potansiyel değerinde ve daha da önemlisi aksiyon potansiyeli süresince gösterilmiştir. Buna karşılık, ek mikro-yapısal hatalara rağmen DTI tabanlı görüntülerin kalbin elektriksel aktivitesinin simülasyonu için en güvenilir yöntem olduğu gösterilmiştir.

Anahtar Kelimeler: Aleiv Panfilov Model, Anizotropi, Transmembran potansiyel, Normal ve kısmi Iskemik doku, Wolf-Parkinson-White, Ektopic aritmi

To my family

ACKNOWLEDGMENTS

I would like to express my sincere gratitude to my supervisor Assoc. Prof. Dr. Yeşim Serinağaoğlu Doğrusöz for her guidance, advice, encouragements and support throughout the research. As a national Master of Science student, I was supported by Turkish Scientific and Technological Research Council (project no: 111E258), I also want to thank them for their support. I would like to thank my laboratory mates and friends Mohammadreza Robaei, Gizem Bedir, Ugur Cunedioglu, and Ceren Bora for their friendship and support throughout my study. I also would like to express my appreciation to my colleagues in Graduate School of Natural and Applied Sciences, for the enthusiastic support throughout the development of this thesis. I also wish to thank to my friends: Kaveh Gharabaghi, Bedia Ovec, and Yaser Mohammadi for all valuable memories and for their encouragements during my studies. Special thanks to Maryam Karimi, for her endless support, patience and love from the moment we met. He always believes in me more than I do. More than all, I would like to express very special thanks to my dear parents for their endless support and love throughout my education. I would not be able to finish my Master studies without their full support. Their support, confidence, and love make everything easier.

TABLE OF CONTENTS

APPENDICES

LIST OF TABLES

TABLES

LIST OF FIGURES

FIGURES

LIST OF ABBREVIATIONS

AHM	Auckland heart model
AP	Action potential
APD	action potential duration
AT	Activation time
AV	Atrai-Ventricular
bpm	Beat per minute
CCAT	Correlation coefficient of activation time
CCRT	Correlation coefficient of recovery time
CCAPD	Correlation coefficient of action potential duration
CT	Computed tomography
CVD	Cradiovascular disease
CVS	Cardiovascular system
DTI	Diffusion tensor imaging
DWI	Diffusion weighting imaging
ECG	Electrocardiography
FHN	FitzHugh-Nagumo
FD	FİnIte difference
HP	haemodialysis
LA	Left atria
LRI	Leo-Rudy I
LRII	Leo-Rudy II
LV	Left ventricular
MAE	Mean absolute error
MCCTMP	Mean correlation coefficient of transmembrane potential
MCCAP	Mean correlation coefficient of action potential
MNE	Mean norm error
PPH	plateau phase
RA	Right Atria

RT	Recovery time
RV	Right ventricle
SA	sinoatrial node
TMP	Transmembrane potential
UHM	Utah heart model
WFST	Wavefront span time
WHO	World health organization
WPW	Wolf-Parkinson-White
3D	Three dimensional

CHAPTER 1

INTRODUCTION

According to World Health Organization (WHO), An estimated 17.3 million people died from cardiovascular diseases (CVDs) in 2008 and by the year 2030 over 23 million people are estimated to die by CVDs annually [3]. In addition, according to another study among patients with chronic haemodialysis (HD) [30], it was shown that 39.9% of mortality is due to cardiac failure. The main causes of death were due to ischemic heart diseases (61.5%), arrhythmias (17.2%), congestive heart failure (10.5%), and cardiac sudden death ($\sim$ 25%). For diagnosis, treatment and prognosis of these cardiac diseases, understanding and characterisation of their mechanism is a matter of importance.

Cardiac function can be investigated through electrical and mechanical activities of the heart, which have reciprocal effect on each other. Therefore, by understanding the underlying electrical activity of the heart, one can describe all functional states of the heart. Current methods for obtaining spatial or spatio-temporal information about the electrical activity of the heart ranges from 12 lead ECG and catheterization to open chest surgeries. The classical method of 12- lead electrocardiography (ECG) by measuring electrical activity of the heart using electrodes on the body surface can be used for diagnosis purposes. However, its low resolution limits this technique's benefits: For example, precise localization of some arrhythmias such as myocardial infarcts is not possible using 12-lead ECG [101], and approximately 60% of acute inferior myocardial infarctions can be diagnosed using 12-lead ECG method [87]. Moreover, 12-lead ECG results can be influenced by inhomogeniety within the thorax, Brody and respiration effects [85]. Recently, some cardiac maps are obtained

using endocardial and epicardial multielectrode catheters, which represent an estimation of electrical activity of the whole heart by using a interpolation and linear least square functions [75]. However, this method is considered as an invasive method, and also yields information at subendocardial or subepicardial levels and the development of the technique is still incomplete. There are also some other methods to monitor the electrical activity of the heart; namely, open surgery, cardiac computed tomography (CT), nuclear imaging, stress electrocardiography and echocardiography. However, these methods either are highly invasive or yield restricted spatio-temporal information. Moreover, some lethal functional states of the heart such as ischemia, and myocardial infarction associated with ischemia, are difficult and sometimes impossible to be investigated by clinical studies on patients, due to fast electro-physiological alteration to be followed by clinical studies [75]. In addition, during these lethal cardiac functional states, the primary concern is resuscitation of patients life, rather than doing any researches.

To overcome these problems, mathematical modelling of the heart, which provides a quantitative data with qualitative understanding, can be applied. Cardiac models provide a simplified description of the heart and can exist in a physical and mathematical representation. Some advantages of using this type of electrocardiograph, monitoring are:

- Noninvasive monitoring,
- Information at epicardial, endocardial and myocardial level of the heart muscle,
- The possibility of further study of disease mechanism and properties,
- Screening of people that have higher risks for arrhythmia,
- Determining the optimal location and size of the diseased tissue for ablation and drug delivery,
- High spatio-temporal resolution.

Due to aforementioned advantages, and advances in computer technology, the studies on different cardiac functional states continue faster than ever before,

and the main motivation of thesis is to make contribution to those efforts.

1.1 Scope of Thesis

This thesis is done to model electrical activity at macroscopic level in normal functional state, and some pathological states of the heart. The simulations represent cardiac cycle through depolarization, repolarization and plateau phase of each cell.

Aliev-Panfilov model was chosen for modelling 3D TMP distribution and propagation on the ventricular tissue. The model using definition from FHN model and addition of extra features is able to obtain electrical activity information at tissue level.

Two realistic heart models were used in this work. These models are from dog hearts, where geometry and fiber orientation information were acquired via two different methods; (1) experimentally, where the information were obtained through a histologically sectioning of cardiac tissue (2) by using medical imaging techniques.

1.2 Contribution of thesis

The main motivation of this study is to simulate transmembrane potential (TMP) on three dimensional (3D) ventricular tissue using Aliev-Panfilov model, which is a modified version of FitzHugh-Nagumo (FHN) model. In addition to the main objective of this study, we also aim to study:

- Distributions of activation time (AT), recovery time (RT), and action potential duration (APD) maps of myocardium cells,
- The effects of anisotropic nature of cardiac conduction, when compared to isotropic assumption of cardiac conductivities,
- The effects of fiber orientation errors on the simulation results,
- Estimation of electrical activity in a heart, using fiber orientation

information of another heart,

• Simulation of different normal and abnormal functional states of the heart.

1.3 Organization

This thesis is organized in a way that, after the 1^{st} Chapter, the introduction of thesis, Chapter 2 is devoted to background information. In this Chapter, first anatomy and physiology of the heart are described. second, most common cardiac diseases are explained. Next, different methods for cardiac mapping are given. Then, different cellular and tissue models are explained for modelling of cardiac electrical activity along with literature survey on these topics. Finally, the chapter is concluded with a section on validation of investigations on ventricular electrophysiological modelling and applications.

The third chapter contains definition, theory, and geometry models for simulation of electrical activity of the heart. In this Chapter, after defining Aliev-Panfilov equations, numerical implementation of the model in 3D geometry is described. Next, after defining cardiac geometry models, two geometry refinement methods were explained, in which one of them is for preparing geometries proper for finite difference (FD) based solution of Aliev-Panfilov equations, and the other method is for transferring information from a known heart to an unknown one.

Chapter 4, using the application details of theory given in Chapter 3, anisotropic nature of cardiac tissue is investigated. First, anisotropy simulation of cardiac tissue was compared to isotropic one. Next, effect of fiber orientation variance representing geometry error, is investigated. Finally, a new method, suggesting an accurate and easy method for simulation anisotropic nature of the heart is done.

Chapter 5, results of simulation based on MR images are represented. In this Chapter, normal and abnormal functional states of the heart are investigated. These functional states focuses on functional state of the heart during normal heart beats and ectopic heart beats, heart with partially ischemia, and Wolf-Parkinson-White (WPW) Syndrome separately.

In last Chapter, conclusions of this study are presented.

CHAPTER 2

BACKGROUND INFORMATION

2.1 The Heart

The heart is a muscular tissue, capable of spontaneous contraction with inbuilt electrical system. This organ is central part of cardiovascular system (CVS), which located slightly to the left of the midline in the chest, and behind breast-bone. It weighs less than 500 grams, and beats normally 60 to 70 times per minute, which pumps almost 5 liters of blood per minute. The purpose of electro-mechanical function of it, is to provide body organs with nutrition and oxygen and removal of waste materials from them through blood.

2.2 Cardiac Anatomy

The heart internally has divided to four sections; two atria, and two ventricles. The wall between these sections is called septa. Atria are connected to ventricles through valves, that allow to flow of blood in certain direction. The valve between right atria (RA) and right ventricle (RV) is called tricuspid valve, and the valve between left atria (LA) and left ventricle (LV) is called mitral valve. Blood vessels that conduct blood into the heart are called veins, and those that conduct blood outside, are called arteries. The outflow of blood from LV is conducted trough aortic valve to aorta, and outflow of blood from RV is through pulmonary artery to pulmonary valve. The location of heart components is shown in Figure (2.1).

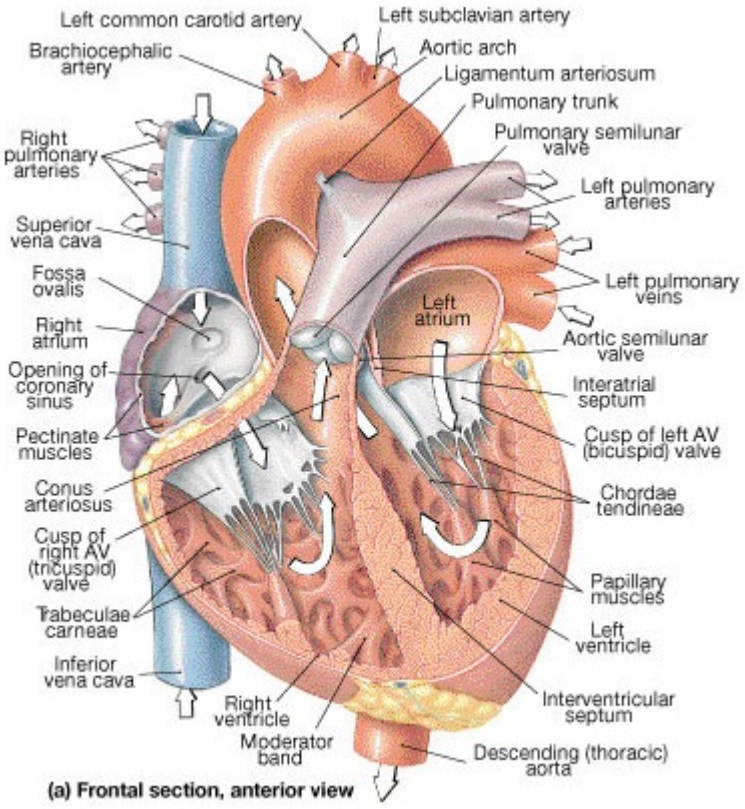

Figure 2.1: Main components of the heart [1]

The cardiac tissue is enclosed with the pericardium. The region between the heart and pericardium is filled with fluids serving as lubrication materials avoiding problems that can occur during cardiac movement [130]. Discarding pericardium, cardiac tissue consists of three layers namely: epicardium, myocardium and endocardium as shown in Figure (2.2). Epicardium layer is located in outer layer of the heart. Many investigations uses potential values on this layer as the main source for solving forward and inverse problems of electrocardiography. Endocardial layer, lines the chambers of the heart, consists enormous part of cardiac tissue. The layer's electrical potential is used in most of electrocardiography imaging, in particular catheter based studies as the cardiac source. Finally, myocardium is the actual cardiac layer containing myocytes (straight muscle cells), responsible for cardiac contraction, and relaxation during pumping of the blood. This layer is located between epicardium and endocardium of cardiac tissue, and is the main objective of electrocardiographic imaging studies.

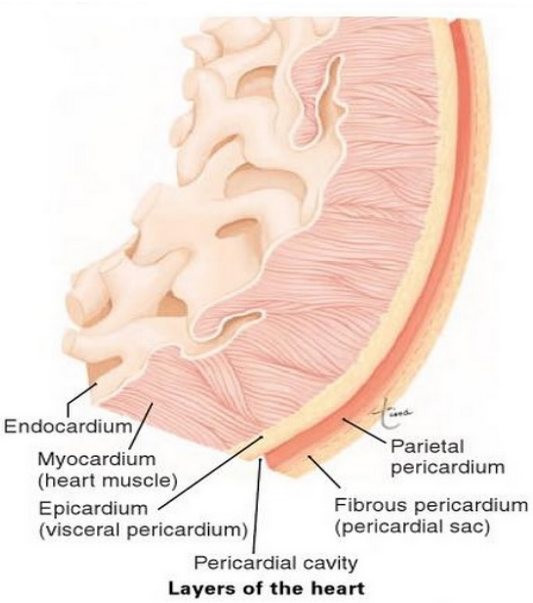

Figure 2.2: Layers of cardiac tissue [67]

2.3 Cardiac Physiology

The blood flow into RA through superior and inferior cavae, which then passes to RV through tricuspid valve. The blood will be then pumped into pulmonary valves and pulmonary arteries, which will conduct it to lungs. After exchanging gas in lungs, the oxygenated blood will flow into LA through right and left pulmonary veins, which will be conducted to LV through mitral valve. This blood will be pumped into coronary arteries and peripheral circulation by passing though aortic valve [67].

2.3.1 Cardiac Conduction System

The electrical conduction of normal heart, starts from sinoatrial (SA) node, with spontaneous excitation ability and rate of 60 to 100 beats per minute (bpm). Then reaches the atria-ventricles (AV) node of atrium. AV node is the only electrical conduction pathway between atria and ventricles. This node also has spontaneous excitation, but with rate of 40 to 60 bpm, which cause to lower the electrical conduction velocity. The delay at AV node has two advantages: (1) intercept synchronous depolarization of ventricles and atria (2) controls the fre-

quency and prevents ventricles from atrial flutter [73]. The electrical conduction then will be conducted to left and right bundle branches through bundle of His, where the conduction velocity increases. The wavefront then will be conducted to purkinje fibers, which cause induction velocity to increase even more, and lastly distributes in ventricular myocytes.

The different conduction features of electrical conduction pathway is shown in Figure (2.3). In spite of self excitation ability of SA node, AV node, bundle of His, bundle branches, and purkinje fibers have also self excitation ability. However, their activation frequency are lower than SA node, and they follow higher excitation frequency, which prevent lethal consequences that might be occurred due to problem in SA node.

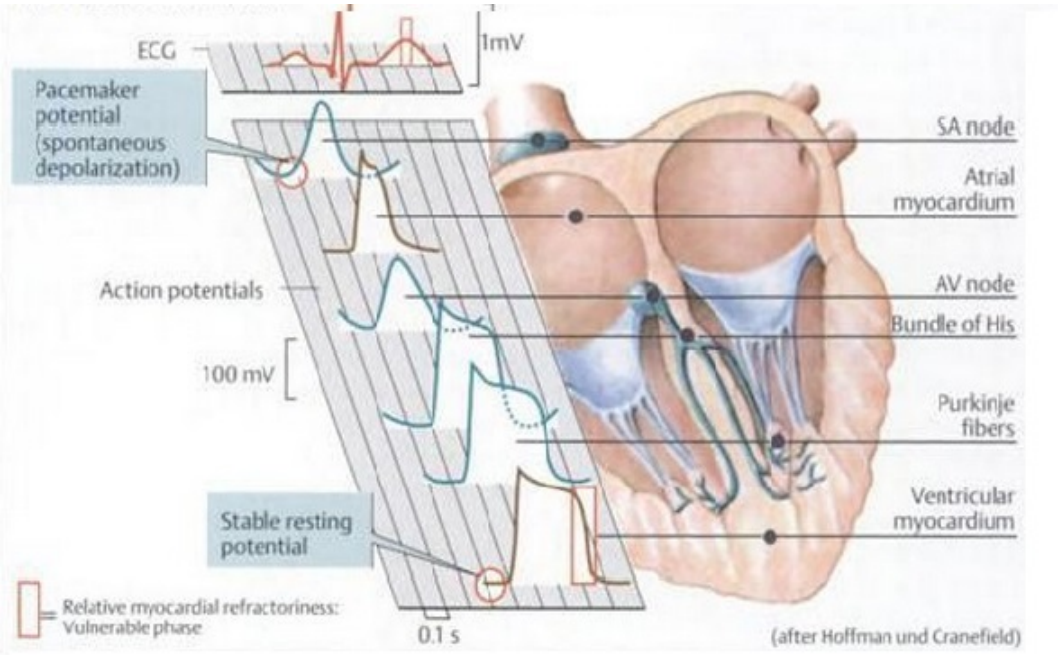

Figure 2.3: The different wavefront for each of specialized cardiac cell [38]

2.3.2 Cardiac Action Potential

Action potential (AP) of a cell can be defined as alteration in potential value of that cell, in which electrical potential values rapidly increases and falls following

relatively constant trajectory. Generation of AP is due to alteration of sub-cellular dynamics, which can be described as below:

Phase 0: quick opening of Na^+ channels, and inward influx of sodium ions, which cause the membrane potential to have positive value from its previously negative value (resting potential), called depolarization.

Phase 1: opening of slower K^+ channels, which stops the rising potential due to outward influx of potassium ions.

phase 2: closure of Na^+ channels, while K^+ channels are still open.

phase 3: opening of slow Ca^{++} channels for approximately $20ms$, which cause inward influx of these ions, and leading to the plateau in membrane potential.

phase 4: Closure of Ca^{++} channels and alteration of membrane potential to resting value, which is called repolarization.

A typical ventricular myocyte AP is shown in Figure (2.4).The shape of AP in cardiac tissue is different from rest of body cells, because existing of Ca^{++} channels in cardiac myocytes cause them to have plateau phase which continues between $200ms$ to $300ms$.

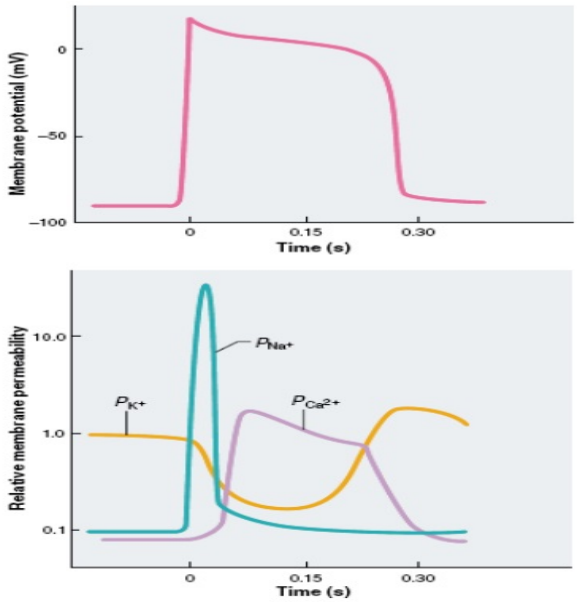

Figure 2.4: Typical ventricular AP (upper figure), and its sub-cellular ions permeabilities (lower figure) [130].

2.3.3 Electrocardiography

The classical electrocardiography (ECG) is summation of cardiac action potentials. As shown in Figure (2.5), A typical ECG signal consists of three main peaks namely: P, QRS, and T. The P peak describes atrial depolarization, QRS interval is parallel with ventricular depolarization and atria repolarization, and finally T peak represents ventricular repolarization. The detailed correspondence of ECG in cardiac impulse conduction can be seen through Figure (2.6)

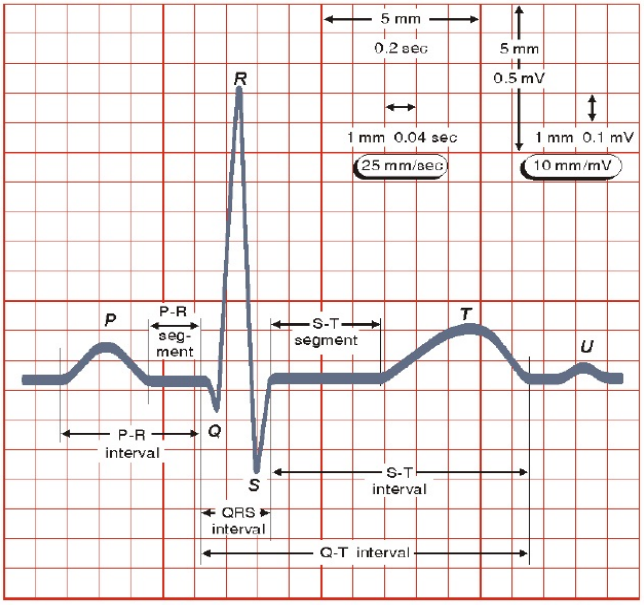

Figure 2.5: A typical ECG signal [85]

2.4 Cardiac Diseases

There are large number of diseases relating to heart disorder such as cardiovascular diseases, coronary artery disease, atherosclerosis. etc. However, in this section only some of cardiac diseases, that affect electrical activity in cardiac myocardium, particularly ventricular myocardium muscle will be explained.

2.4.1 Cardiomyopathy

This kind of disease refer to deterioration in ability of myocardium in contraction. There are three main types of cardiomyopathes namely: dilated, hyper-

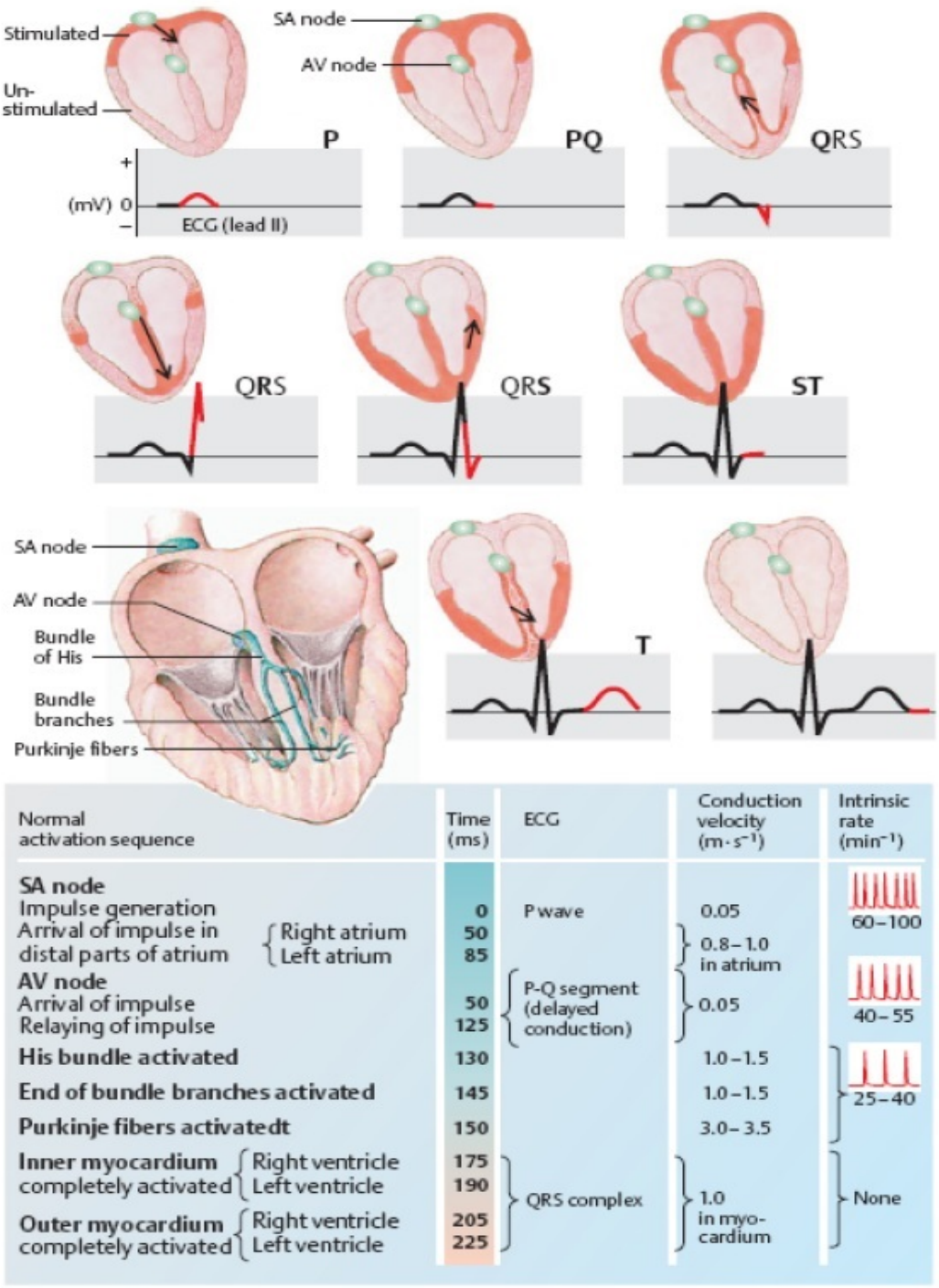

Figure 2.6: Correspondent of ECG at each step of cardiac impulse propagation [38].

trophic and restrictive cardiomyopathies. The worse the cardiomyopathy is, the weaker heart pumps. This can lead to deteriorated (delated) response of underlying tissue and cause irregular heart beats (arrhythmia), or heart failure.

2.4.2 Cardiac Arrhythmias

The heart is two stage electromechanical pump, that beats with 60 to 70 bpm in rest, which can reach to maximally 250 bpm with maximal exercise. However, there would be an abnormality if the frequency of pumping alters due to cardiac internal conduction system disorder, which is called arrhythmia. There are several kind of arrhythmias to explain some of them: SA impulse arrhythmia, is change in electrical impulses generation with higher rate (Tachycardia), or lower rate (bradycardia), Ectopic pacemaker is the other kind of arrhythmia in which stimulation of myocardium starts from a region other than SA node, which can be atrium, AV node, or ventricle.

2.4.3 Ventricular Tachycardia

The ventricular tachycardia, is a kind of cardiac arrhythmia, in which excitation starts from ventricles rather than SA node. The disease starts with an extra contraction in left ventricle, and cause reduction in stroke (ejection of blood to body) volume [38].

2.4.4 Ventricular Fibrillation

Ventricular fibrillation is the most severe cardiac arrhythmia, and if not treated within 1 to 3 minutes, can cause death. During the disease ventricular muscle twitch irregularly and mostly do vibration rather than complete contraction. Ventricular fibrillation is due to abnormal atomicity, in which muscle can be stimulated by several pacemakers [60].

2.4.5 Wolf-Parkinson-White Syndrome

Wolf-Parkinson-White (WPW) is one of preexcitation syndromes occurs due to abnormal electrical pathway between atria and ventricular chambers. The syndrome cause premature contraction of ventricular tissue, and lead to a type of tachyarrhythmias. The ECG of a patient with WPW syndrome is shown

in Figure (2.7). It can be seen that WPW syndrome is mostly known with ECG signal with decreased PR segment, and wide QRS complex with slurred initial segment QRS complex, which is called delta wave. Moreover, altered ST segments, and T wave reflects secondary repolarization changes. [106].

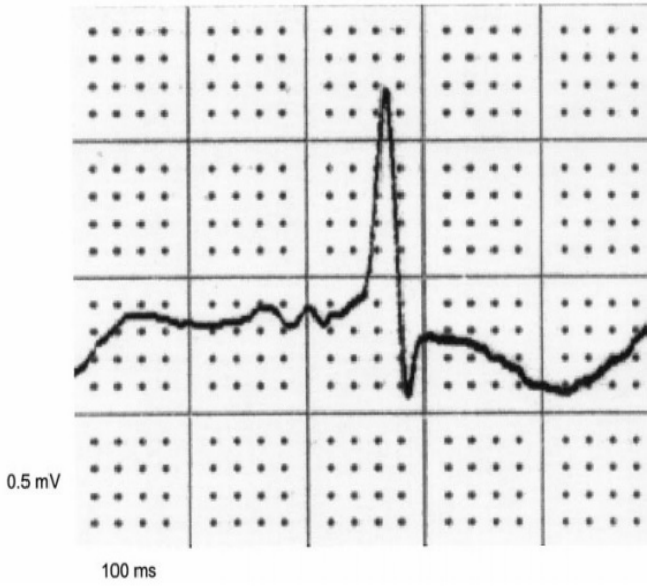

Figure 2.7: ECG signal of a patient with WPW syndrome [69]

2.4.6 Ischemia

Myocardial ischemia is one of the major causes of sudden cardiac death. Acute myocardial ischemia, obstructs coronary outputs and prevents oxygen and glucose flow in affected tissue. It also interrupts removal of waste materials from underlying tissue. The deterioration in both energetic input and removal function, in microscopic level lead to deterioration in electrical activity of cells and even cell death, and in macroscopic level cause malignant fibrillation, and pump failure [104].

Electrophysiological changes, in coronary occlusion, particularly within early acute stage of ischemia (first 10 to 12 minutes) is so rapid, which make it difficult for clinical studies to track underlying alterations. However there are some experimental works [74, 104, 133, 134], shown that ischemia laed injured tissue cells to have increased intracellular Na^+, and Ca^{++} , extracellular K^+ ions concentrations respectively. It also causes reduction in amount of intracellular ATP

and PH. These ionic alterations lead to electrical deterioration, that cause AP to have lower amplitude and duration, and higher resting potential values as shown in Figure (2.8).

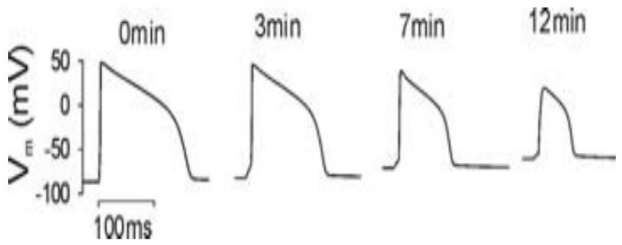

Figure 2.8: Ischemic AP 12 minute after coronary occlusion [104]

2.5 Cardiac Mathematical Modelling

Functional state of the heart starts by electrical wavefront, which causes release of myocyte calcium. Binding of these released calcium to Troponic C and cross-bridge cycling from a basis for movement of contractile proteins, which lead to tension of myocytes and deformation of entire muscle respectively [126]. This principle of cardiac function forms basic of all mathematical modelling, defining two coupled parts; namely, modelling the electrical, and the mechanical functions of the heart. Through mathematical modelling of cardiac tissue, even in most simple description we aim to simulate propagation of an electrical impulse through network of cells or the entire tissue.

Mathematical modelling of electrical activity of the heart can be classified differently [31,102,108]. In this thesis, according to Sachse *et.al.*, [108], the numerical solution was classified into two parts: (1) ionic models, (2) tissue models. The first method mostly focuses on dynamic behaviour of current at cellular level, but the latter focuses on dynamic changes and wavefront propagation at tissue level. Most of the cardiac mathematical models are based on early models of Hodgkin-Huxley on squid giant axon [62]. Therefore, description of Hodgkin-Huxley model prior to other models can be helpful in understanding of them. According to aforementioned explanation, as cardiac function is mostly depen-

dent on electrical activity of the heart, we mostly focus on electrical activity of the heart rather than mechanical activity.

2.5.1 Hodgkin-Huxley Model (1952)

This model was the first model, that describes the dynamic electrophysiological behaviour of giant axon membrane from measurement of active and passive electrical behaviour with remarkable accuracy [62]. The model using transmembrane data and equivalent circuit (Figure 2.9), allows calculation of ionic currents of ions passing through the axon membrane (shown in Figure 2.10) and the transmembrane voltage and can be described as:

$$\frac{\partial V_m}{\partial t} = \frac{1}{C_m}(I_m + I_{stim}) \tag{2.1}$$

where V_m, is transmembrane voltage, and can be calculated by subtracting the extracellular voltage V_e from the intracellular voltage V_i. C_m represents the cell membrane capacitance, I_{stim} is the stimulation current, and I_m is the membrane current, that can be calculated as:

$$I_m = I_{Na} + I_K + I_l + I_c \tag{2.2}$$

With sodium current I_{Na}, potassium current I_K, and leakage current I_l representing sodium, potassium and other ion flows through the membrane. These currents can be calculated using:

$$I_{Na} = g_{Na}(V_m - E_{Na}) \tag{2.3}$$

$$I_k = g_K(V_m - E_K) \tag{2.4}$$

$$I_l = g_l(V_m - E_l) \tag{2.5}$$

Where g_{Na}, g_K, and g_l are conductance, and E_{Na}, E_K, and E_l are Nernst potentials of sodium, potassium, and leakage ions, respectively.

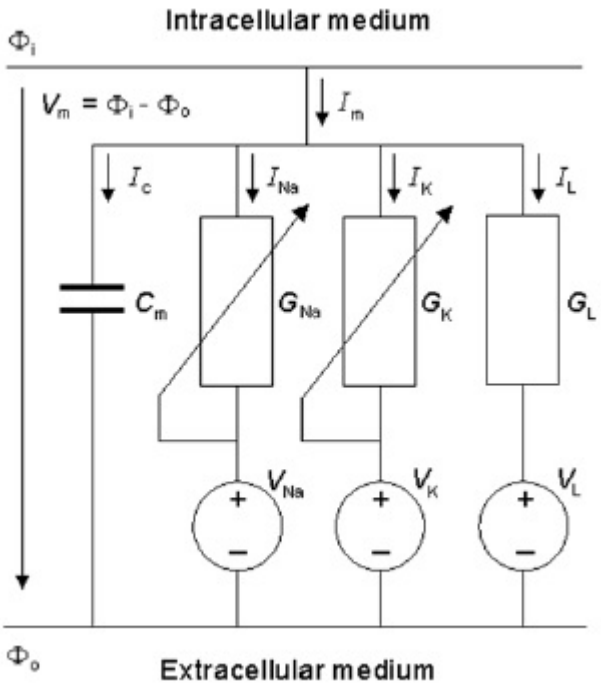

Figure 2.9: Equivalent circuit of axon cell membrane equivalent circuit of axon cell membrane [85]

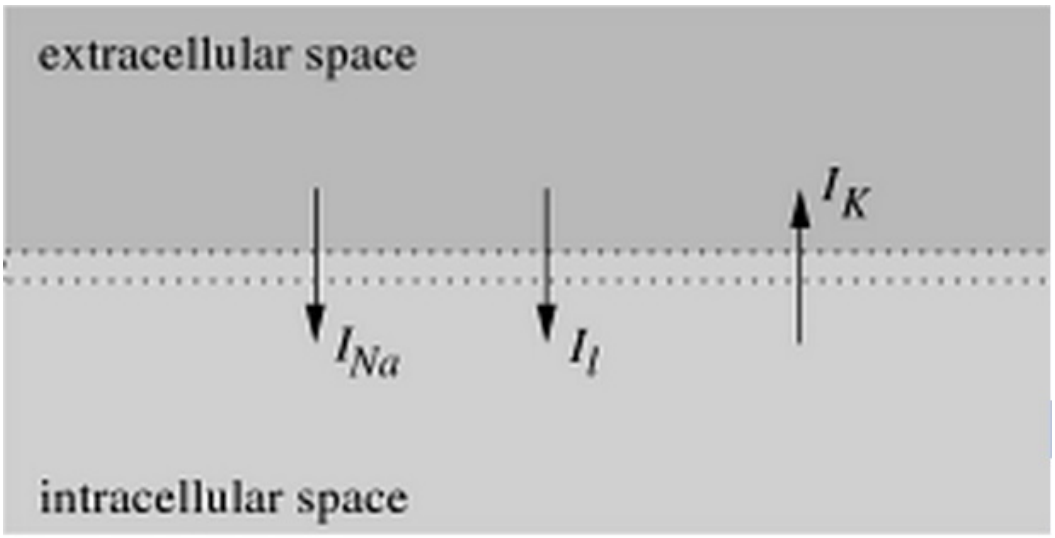

Figure 2.10: Schematic diagram of Hodgkin-Huxley model describing ionic current flow (shown in arrows), and potential across the cell membrane (shown with dashed lines) [108].

2.5.2 Ionic models

These kind of models aim to describe the electrical activity of the cells by focusing on dynamic electrophysiological behaviours at sub-cellular features such as;

ion concentration, cellular channels, pumps and exchangers. Majority of these models have components based on Hodgkin-Huxley model. Since, the heart has several types of excitable cells with different features, during implementation of these models, the original cell, in which model has formed should be considered. According to the scope of this thesis, which is focused on ventricular tissue, a subset of models related to ventricular cells are presented in this section.

Beeler-Reuter Model Beeler and Reuter proposed the first mathematical modelling for mammalian cardiac ventricles. The model is featured by addition of two inward current and two outward currents. Their aim was to add the role of calcium concentration change as a new current variable (Figure 2.11) [16].

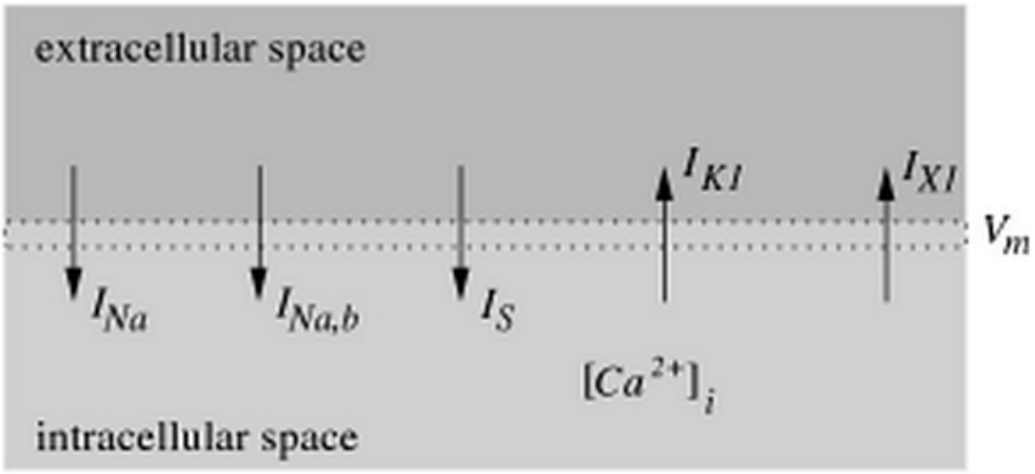

Figure 2.11: Beeler-Reuter Model Variables [108].

Luo-Rudy I Model (LRI) LRI model is based on Beeler-Rueter model. This model presents more recent experimental results by adjusting the activation and inactivation parameters. Furthermore, by addition of new ionic current variables as shown in Figure (2.12), it represents more accurate results [80].

Luo-Rudy II (LRII) This model is widely used in the field of cardiac excitation [108]. The model is based on data from a guinea pig, and its differentiating feature is in including phenomenological details of Calcium-induced and Calcium released. The model includes 15 ionic currents to generate AP [81, 82]. The model was later improved, and its latest version was released by Faber and

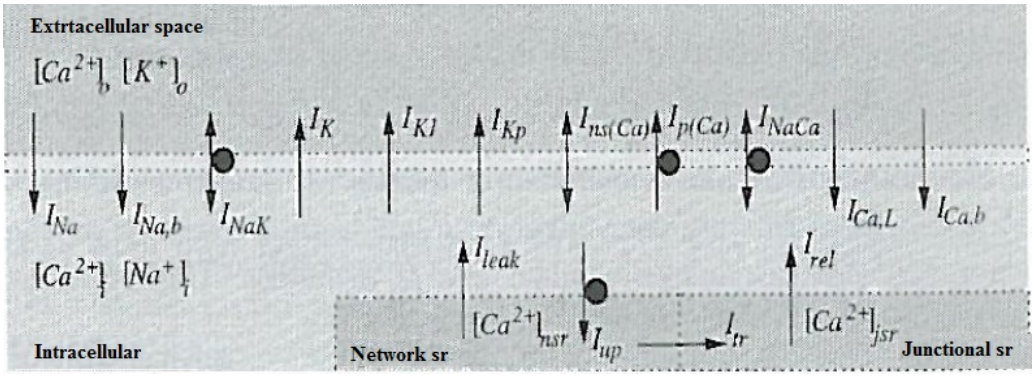

Figure 2.12: LRI Model Variables [108].

Rudy at 2000 [44].

Other Approaches There are a large number of ionic models in literature, that represent electrical activity of the cell, and new models also are appearing continuously by addition of current variables with different level of complexity. The list in Table (2.1) shows other investigations in this field, which can be useful for understanding hierarchical development of ionic models in recent decades.

Table 2.1: Some of ionic models related to ventricular cells [102].

Year	Author	Type	Reference
1977	Beeler & Reuter	canine	[16]
1980	Ebihara & Johnson	chick embryo	[42]
1987	Drouhard & Roberge	mammal	[40]
1991	Noble, Noble, Bett, Earm, Ho & So	guinea pig	[92]
1991	Luo & Rudy	guinea pig	[80]
1993	Nordin	guinea pig	[94]
1994	Luo & Rudy	guinea pig	[81, 82]
1996	Demir, O Rourke, Tomaselli, Marban & Winslow	canine	[36]
1998	Jafri, Rice & Winslow	guinea pig	[65]
1998	Noble	guinea pig	[93]
1999	Wislow, Rice, Jafri, Marban & O Rourki	canine	[138]
2001	Pandit, Clark, Giles & Demir	rat	[96]
2001	Puglisi & Bers	rabbit	[100]
2002	Bernus, Wilders, Zemlin, Verschelde & Panfilov	human	[20]
2003	Sachse, Seemann, Chaiaowong & Weiss	human	[113]
2003	Matsuoka, Sarai, Kuraton, Ono & Noma	guinea pig	[86]
2004	Tusscher, Noble, Noble & Panfilov	human	[122]
2008	A. Mahajan	rabbit	[83]

2.5.3 Tissue Modellings

These kinds of models focus on macroscopic features at tissue level, and can be mainly divided into two categories: cellular automata and reaction-diffusion models. Cellular automata represents underlying spatial structure by either infinite, regular and discrete network or finite automaton working at each node (so called cell) of the network [108]. Reaction-diffusion methods use a system of non-linear partial differential equations to describe the excitation and propagation process in excitable media [108].

2.5.3.1 Cellular Automaton

The first cellular automaton models were proposed in 1946 for propagation and distribution of activation in two dimensional (2D) space [135]. Then, these models were used for modelling atrial fibrillation [89]. These kinds of modelling methods are idealization of physical system, and only take place in discrete space, time, and state. In principle, there are cellular array, that evolve step by step dependent on the state of neighbouring cells.
There are many studies using cellular automaton method for modelling different cardiac features such as; heart beats in fibrillation state, excitable and reaction-diffusion media [5, 68], excitation distribution with simplified action potential, diffusion and speed of electrical wave [4, 51] electrical wave propagation, fibrillation and arrhythmias characterization concerning anisotropic nature of the heart [54], functional approximation of pacemaker [84].

2.5.3.2 Reaction-Diffusion Models

Reaction diffusion systems are models, using non-linear partial differential equations (PDEs) solutions coupling with domain definition for modelling current flow through myocytes that are electrically connected with low resistance gap junctions. The model mostly focuses on dynamic changes and wavefront propagation at tissue level and can be divided into two categories: (1) simplified models, such as two variable FitzHugh-Nagumo [FHN] [47,90], Aliev-Panfilov [6] and

Eikonal [49] models in which variables have no physical meaning, but in terms of computer simulation times this approach is more preferred. (2) Approaches in which electrophysiological cell models are combined with electrical current flow models, namely bidomain and monodomain models [35].

2.5.3.2.1 Simplified Models When the investigation of biophysiological phenomena in larger spatio-temporal scale is a matter of importance, modelling methods with least computational cost, and easiest applicability are more important. Regarding this issue, simplified models of cardiac myocytes regardless of sub-cellular dynamic changes, represent action potential features at the least computational cost.

Polynomial Model The simplest of reaction- diffusion simplified models is polynomial model, that was proposed first by Hunter, and colleagues [64]. The model uses only one variable, which is able to track depolarization phase of AP. Since, this model does not provide information about repolarization phase, it is not suitable for TMP and re-entrant phenomena.

The Eikonal model This model is the other simplest and fastest model, used in cardiac electrophysiology [48]. The model can be expressed as:

$$\nu^2(\bigtriangledown T_d^t D \bigtriangledown T_d) = 1 \tag{2.6}$$

where ν is the local speed, D relates conductivity ratio between transverse and longitudinal directions, and T_d represents depolarization of AP.
Eikonal model, is also simple and fast, and can include anisotropic nature of cardiac tissue, but gives information of just depolarisation phase of wavefront [49, 56]. So, it can be appropriate for getting activation time information, but it is not proper for getting the transmembrane potential and restitution properties, similar to polynomial model.

FitzHugh-Nagumo (FHN) model FitzHugh-Nagumo model [47,90] uses a cubic polynomial, which is able to model both excitation and recovery variables of AP. However, this model fails to represent several quantitative parameters of cardiac tissue such as action potential shape, restitution and anisotropic properties, which limits it to study excitation propagation properties qualitatively rather than quantitatively [6]. This model will be explained in detail in section (3.2).

Aliev-Panfilov Model Aliev-Panfilov model [6] is a modified version of FHN model. By the addition of conductivity tensor and refractory information, this method eliminates those constraints of FHN model. This model will be discussed more in section (3.2).

Other Approaches There are also a number of other studies that use different algorithms of modelling like Rogers-Modified FitzHugh-Nagumo model [105], and Fenton-Karma Model [45] for modelling cardiac AP. The first one is a model based on FHN model, and by removing hyperpolarization of AP made more accurate model. The latter is mostly based on Luo-Rudy [80], and Beeler-Rueter [16] models, which by addition of optical mapping data replaces the complex formulation of those ionic models with relatively similar results for AP.

2.5.3.3 Combination of Electrophysiological Cell Models with Electrical Current Flow Models

These kinds of models couple electrophysiological models of myocardium cells with models of electrical current flow through intracellular and extracellular space. These models can be divided into two different groups according to their domain definition: (1) bidomain models (2) monodomain models.

Bidomain model This model is a volume average (continuum) model that takes into account the anisotropy of both intracellular and extracellular spaces. In other words, this model is a continuum model, which represents the average properties of many cells, rather than describing each cell individually. The bidomain model was first proposed in 1969 [112], and formulated mathematically by Tung [127]. The model is a system of two non-linear partial differential equations, one for each of the intracellular and extracellular potentials, coupled to a system of ordinary differential equations representing the cell ionic activity, which can be represented as [98]:

$$\nabla \cdot (\sigma_i \nabla \phi i) = BI_{tm} \tag{2.7}$$

$$\nabla \cdot (\sigma_e \nabla \phi e) = -BI_{tm} \tag{2.8}$$

Where ϕ_i, and ϕ_e represent intracellular and extracellular potentials, σ_i, and σ_e are intracellular and extracellular conductivity values. Here B is the ratio of myocytes per volume, and I_{tm} is the transmembrane current and can be calculated through:

$$I_{tm} = C_m \frac{\partial V_m}{\partial t} + I_m \tag{2.9}$$

Here C_m, is the membrane capacitance, I_m is the ionic current, and V_m is the transmembrane potential. We can write a reaction diffusion equation in terms of ϕ_e and V_m as:

$$\frac{\partial V_m}{\partial t} = \frac{1}{BC_m}(\nabla \cdot (\sigma_i \nabla (V_m - \phi_e)) - BI_m) \tag{2.10}$$

Then, by addition of (2.7), and (2.8) by considering $\phi_i = \phi_e + V_m$ we can write an implicit equation of bidomain model as:

$$\nabla \cdot ((\sigma_i + \sigma_e) \nabla \phi_e) = -\nabla (\sigma_i \nabla V_m) \tag{2.11}$$

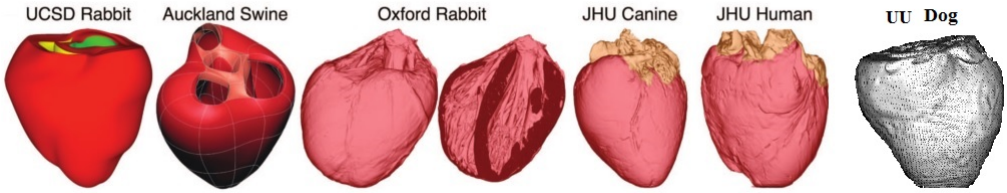

Figure 2.13: Common heart models [126].

Monodomain Model The monodomain model is a reduced form of the bidomain model. If the conductivity tensors of monodomain $\sigma_i^{'}$, $\sigma_e^{'}$ satisfy $\sigma_i^{'} = (1+\zeta)\sigma^{'}$, and $\sigma_e^{'} = ((1+\zeta)/\zeta)\sigma^{'}$ where $\sigma^{'}$ is the bulk conductivity tensor, and ζ is a scalar value, we can obtain monodomain reaction diffusion equation by substituting of $\sigma_i^{'}$, and $\sigma_e^{'}$ in (2.7), and (2.8) as:

$$\frac{\partial V_m}{\partial t} = \frac{1}{BC_m}(\nabla \cdot (\sigma^{'} \nabla V_m) - BI_m) \tag{2.12}$$

The monodomain model is less demanding due to absence of ϕ_e role, and accordingly implicit equation to solve [98].

2.5.4 Geometry and Anatomy Structures Review

Cardiac geometry and its structure with different level of complexity define the main domain of solution on which the models are performed. These geometries can be idealized shapes (e.g. cylindrical or elliptical) [11, 27], or anatomically accurate geometries. The latter itself can be obtained through histologically sectioning [76, 91, 117, 131] or can be individual geometry of the heart [23, 59], such as those obtained through magnetic resonance imaging techniques.
Figure 2.13, describes the most prevailed geometry models for modelling electrical and mechanical activity of the heart. The first two models belong to rabbit and swine cardiac models, which were obtained through histological sectioning in University of California, San Diago [131], and Auckland University [117] respectively. The last four cardiac models are individual cardiac geometries obtained through MRI techniques in Oxford, John Hopkins, and Utah Universities [2,128].

2.5.5 Review of Ventricular Electrophysiology Applications

This part reviws, application of different models on ventricular tissue.

2.5.5.1 Modelling wavefront propagation on normal ventricular tissue

There are just a handful of studies concerning propagation on normal ventricular tissues. These studies mostly concern normal propagation and repolarization rather than modelling of any arrythmia [23, 33, 79, 110, 115]. Among all, two studies are more notable. The first is a work done by Samson and Henriques [110], in which they researched the role of cardiac size, myocardium properties, and spatial distribution of cell types on action potential duration (APD). They asserted that, large size of the heart reduces global electronic properties and reveals APD difference among cells. The second study is by Bishop and collogues [23], that focused on heterogeneity property of ventricular tissue, and describes the effect of micro-structural role in wavefront propagation.

2.5.5.2 Modelling mechanism of the ventricular arrhythmia

Majority of studies related to electrical activity of ventricular tissue, focused on arrhythmia rather than its other functional states. Among those, the characterization of self sustained reentry propagation, and fibrillation have received the most interest. One of the early studies on this field is the work by Panfilov and Keener at University of Utah [6]. Using FHN model, they showed that the organization center of reentry activity can be entirely within the myocardium. The model was then used by others, and revealed different aspects of reentry [57,97]. Through fibrilation and reentry propagation, more realistic MRI models were also developed by Winslow and colleagues [136, 137]. Recently, new models are developed on ventricular fibrillation characterization in human heart [123, 124], which give information about the difference of human heart's ventricular fibrillation organization.

Over the last decades, many studies also have shown interest on restitution as a major factor in determination of arrhythmia onset, and dynamic destabilization of reentry, which lead to ventricular tachycardia and to ventricular fibrillation [19, 43, 71, 72].

2.5.5.3 Modelling of ventricular arrhythmia in diseased heart

Whole-heart modelling studies concerning arrhythmia in diseased heart remains in its infancy [126]. One of the recent studies in this field is the work by Jie and Trayanova [66]. The study characterizes a substrate for an ischmia in rabbit ventricular tissue. They conclude, biphasic alteration in arrhythmia vulnerability with the increase in extracellular potassium due to existing of ischemia. Same electrophysiological properties change were observed in subepicardium and subendocardium for varying degrees of hyperkalemia, but conduction block occurres in the subendocardium due to heterogeneity factors. Other examples in this field are simulation of infarct-related ventricular tachycardia using MR-based heart models [8–10]. Stimulation of different sites from endocardial layer demonstrated that the organizing center in infarct-related ventricular tachycardia is located in the boundary zone regardless of the stimulation site. The output of this model could be useful for ablation planning of these kind of diseases [126].

2.5.5.4 Modelling regarding to anisotropic nature of the ventricular tissue

The aim of these models are to understand effect of anisotropic nature of tissue on electrical activity of the tissue. Electrical conduction anisotropy of the heart was first described by Sano *et.al.*, 1959 [111]. Over the last decades, anisotropy of the heart is the most controversial part, and researches on it has increasingly shown the importance. Many researches and studies have been focused on the effects of anisotropy, comparing with isotropic conduction of the heart. There are many published studies on the effects of anisotropy in the forward solution [13, 32, 50] or inverse solution [34, 88, 95, 116]. The studies mostly focus on epicardial or torso potentials, and take AT [34, 50, 88] , electrocardiogram [26]

or body surface potential [88, 116] as their comparison factor. However, few studies have been done on the effects of anisotropoy on myocardial muscle of the heart [116,120] and take transmembrane potential as comparison factor [95,116]. According to these studies, it has been shown that anisotropy has some effect on forward problem solution of ECG [13, 32, 50]. However, its effect on inverse problem solution of ECG is much smaller than forward problem solution [88]. Results from other anisotropic experimental studies [129] in comparison with isotropic simulations have also shown that APD is larger in the direction of fiber alignment and depolarization wavefront propagation pattern is diametric rather than spherical. It was also shown that APD changes almost $14ms$ in the entire heart and repolarization pattern is almost similar, but not equal to depolarization pattern propagation [120].

2.5.6 Other Approaches

There are a number of other studies on heterogeneity in the conduction system of cardiac tissue [18, 28, 33, 37, 132]. The aim of these studies are understanding underlying electrical difference in different sections of the heart [33], and particularly the role of purkinje fibers on different functional state of ventricular tissue [18, 28, 37, 132].
There are also other approaches that study initiation of arrhythmias with electrical shocks and defibrillation [12, 103, 125], or examine different optical methods using fluorescent mapping [7, 22, 24, 25]. More explanation about these approaches can be found in [126].

CHAPTER 3

MODELLING OF THE TRANSMEMBRANE POTENTIAL DISTRIBUTION

3.1 Introduction

There are abundant of models for simulating electrophysiological activity of the heart, from microscopic activities of ion channels of a cell to macroscopic properties of anisotropic propagation of wavefront on entire heart tissue. Corresponding to objective of this study, which mostly focuses on wavefront properties rather than dynamics of ionic currents, we select reaction-diffusion models, because cell models require small space and time steps integration. So, millions of calculations are required to model each centimeter of the heart muscle [6]. Among all reaction-diffusion models; calculation cost, complexity, and obtained information depth are the most important criteria to be considered for evaluating a model. Among these models bidomain and monodomain models are mostly in coupling with other kinds of membrane models. Comparing these two models, bidomain model represents an accurate modelling of electrophysiological waves taking into account the extracellular and intracellular medium. Moreover, it is capable of reproducing ECG by coupling the heart with thorax [17]. On the other hand, monodomain model, although it has limited capabilities in reproducing ECG, is simpler and faster than bidomain model when coupled to the same membrane model [39]. Considering bidomain and monodomain models as domain definition equations, comparison of FHN, Aliev-Panfilov and Eikonal models as the mostly applied membrane models would be reasonable. Eikonal model, although it is the simplest and fastest among all models and gives in-

formation of depolarisation phase of wavefront, does not give information of recovery time (RT), plateau phase (PPH) and action potential duration (APD). So, it can be appropriate for getting activation time (AT) information, but is not proper for getting the transmembrane potential and restitution properties. Both the excitation (depolarisation) and recovery (repolarisation) properties can be obtained from both FHN and Aliev-Panfilov models, which have the same complexity and calculation cost [39], but FHN model fails to represent several quantitative parameters of cardiac tissue such as action potential shape, restitution and anisotropic properties, which limits it to study excitation propagation properties qualitatively rather than quantitatively [6]. Aliev-Panfilov model similar to FHN model is a low dimensional model, which reduces the complex array of ionic currents into two variables representing excitation and recovery features. Moreover, by addition of conductivity tensor and refractory period, it represents a new model, which is as simple as FHN model, and furthermore, is able to model restitution property of cardiac tissue and adequately represents the shape of AP. So, in this study, we apply Aliev-Panfilov model with bidomain definition with a low calculation cost and complexity to obtain reasonable information depth. The hierarchical method of entire simulation is:

• Step 1: Import cardiac geometry as irregular point cloud, and corresponding fiber orientation at each of these nodes.
• Step2: Convert irregular geometry to regular cubic geometry (new points and fiber orientations defined at these points). If necessary, apply registration to transfer fiber orientations from one heart geometry to the other.
• Step 3: In the regular geometry, calculate the global conductivity tensors for each element in the cubic representation using 3.12.
• Step 4: Calculate the finite difference weight factors using (3.13-3.31).
• Step 5: Using these weight factors, solve Aliev-Panfilov equations (3.7), for every point in the geometry and at each time instant, and obtain normalized TMP.
• Step 6: Convert normalized TMP values to true TMP values.

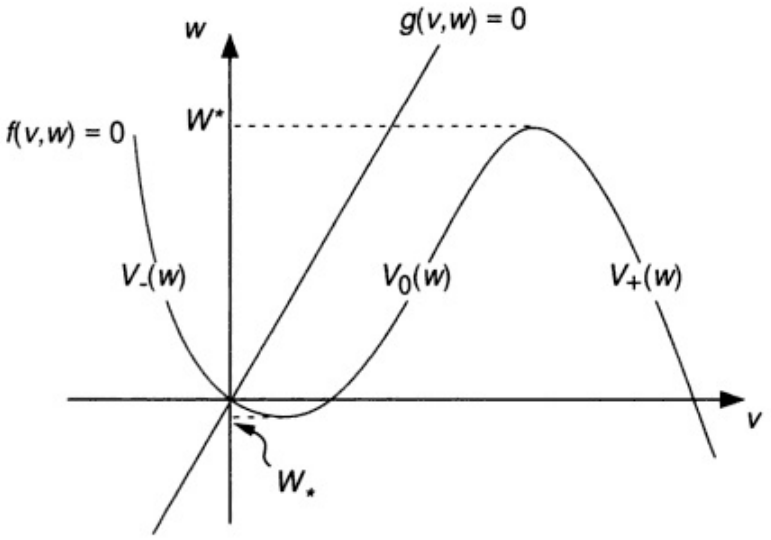

Figure 3.1: FHN phase plane [70]

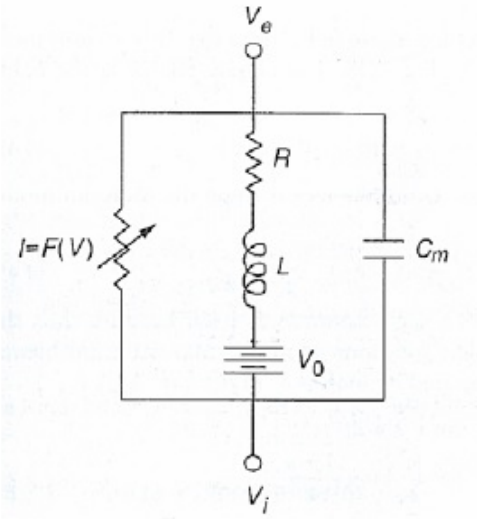

Figure 3.2: FHN membrane circuit [70]

3.2 Aliev-Panfilov Model

Two variable Aliev-Panfilov model is a modified version of FitzHugh-Nagumo (FHN) model [6]. The FHN model motivation was to represent essential features of Hodgkin-Huxley model [61] in a simpler way. They presented most of Hodgkin-Huxley features by fast-slow phase planes depicted in Figure 3.1. The fast phase (v) has cubic nullcline and is called excitation variable, and the slow phase (w) has monotonically increasing nullcline and is called recovery variable. The model can be represented using a cell membrane circuit shown in Figure 3.2. The membrane patch circuit includes a capacitor that represents membrane capacitance, a nonlinear resistor that models the excitable or fast phase, and resistor, battery and inductor branch models the recovery phase. Using Kirchoff's laws we, can describe the circuit as:

$$C_m \frac{dV}{d\tau} + F(V) + i = -I_0$$

$$L\frac{di}{d\tau} + Ri = V - V_0 \tag{3.1}$$

where I_0 is the applied external current, V is the transmembrane potential that can be calculated as $V_i - V_e$, in which V_i and V_e are intracellular and extracellular potential values respectively. V_0 represents the threshold voltage of the membrane, and i is a current passing through the inductor, and the resistor. $F(V)$ is a cubic shape function which has three roots , in which the smallest $V = 0$, and the largest $V = V_1$ are the stable solution for the equation $dv/d\tau = -F(V)$. τ represents time variable.

Let us try to nondimentionalize equation (3.1). Our means by nondimensionalization, is removal of the partial or full units from an equation involving physical quantities by a suitable substitution of variables. Extra explanation about nondimentionalization can be found in Lin, and Segel et al. [77]. If we define

R_1 as a passive resistance of nonlinear element $R_1 = 1/F'(0)$, we can introduce dimensionless variables as:

$$\begin{aligned} \nu &= V/V_1 \\ w &= R_1 i/V_1 \\ f(\nu) &= R_1 F(V_1\nu)/V_1 \\ t &= L\tau/R_1 \end{aligned} \tag{3.2}$$

replacing of (3.2), equation (3.1) becomes:

$$\begin{aligned} \varepsilon\frac{d\nu}{dt} &= f(\nu) - w - w_0 \\ \frac{dw}{dt} &= \nu - \gamma w - \nu_0 \end{aligned} \tag{3.3}$$

where ε, γ, u and ν are dimensionless variables as below:

$$\begin{aligned} \varepsilon &= R_1^2 C_m/L \\ w_0 &= R_1 I_0/V_1 \\ \nu_0 &= V_0/V_1 \\ \gamma &= R/R_1 \end{aligned} \tag{3.4}$$

As explained at the beginning of this section, $f(\nu)$ should have a shape shown in Figure 3.1. Using cubic polynomial we can define it as:

$$f(\nu) = A\nu(\nu - \alpha)(1 - \nu) \tag{3.5}$$

Which gives FHN model, and we can generalize FHN model as:

$$\varepsilon \frac{d\nu}{dt} = f(\nu, w) + I$$
$$\frac{dw}{dt} = g(\nu, w) \tag{3.6}$$

Aliev-Panfilov, modifying FHN model (3.6) also uses a system of non-linear partial differential equations to describe the excitation and propagation process in excitable media. The model uses cubic polynomial to model excitation and includes recovery variable similar to FHN model. Moreover, the model includes the information of conductivity tensor and refractory period [6], in which the courses of excitation and recovery can be calculated as:

$$\frac{\partial \nu}{\partial t} = \frac{\partial}{\partial x_i} \cdot d_{ij} \cdot \frac{\partial \nu}{\partial x_j} - k\nu(\nu - \alpha)(\nu - 1) - \nu w$$

$$\frac{\partial w}{\partial t} = \varepsilon(\nu, w)(-w - k\nu(\nu - \alpha - 1)) \tag{3.7}$$

where $\varepsilon = \varepsilon_0 + (\mu_1 w)/(\nu + \mu_2)$ is a parameter that represents refractory period, and $d_{ij} = d_2\sigma_{ij} + (d_1 - d_2)a_i a_j$ is a parameter that represents conductivity tensor in the longitudinal and the transverse fiber directions. α, k, μ_1, μ_2 and ε_0 are equation parameters to be fixed according to heart's function. σ_{ij} is local conductivity tensor, and describes conductivity at longitudinal a_i and transverse direction a_j. d_1, and d_2 are fiber directions in longitudinal a_i and transverse direction a_j respectively. Moreover, ν, and w are dimensionless variables representing the normalized transmembrane potential and the time dependent recovery values respectively, and actual values of potential (E), and time (τ) can be obtained by:

$$E[mV] = A\nu - E_r \tag{3.8}$$

$$\tau[ms] = 12.9t \tag{3.9}$$

Where A is the maximum amplitude of AP, and E_r is the resting potential of myocardium cells.

3.3 Numerical Implementation of Aliev-Panfilov Model

The two variable Aliev-Panfilov model in two dimensional (2D) space is described in previous section. In our modelling method, we use numerical application of the the model in the 3D space. The numerical implementation of the model is carried out with finite difference method (FDM), in which the time and space domains have been discretized to smaller domains, called elements, and approximate solutions are computed at the element nodes. To do so, we need to divide the domain into uniform meshes.

3.3.1 Finite Difference Equation of Aliev-Panfilov Model

In order to implement (3.7) in three dimensional space, for showing transmembrane potential distribution, we define potential value of each node according to weight values of first neighbourhood nodes, which represent potential effect of those nodes on it. Assuming FDM, each node is common among eight adjacent elements and will be affected by eighteen first order neighbourhood's potential of those element nodes as shown in Figure 3.3. Therefore, we can write numerical form of Aliev-Panfilov model in 3D space as:

$$\frac{\Delta\nu}{\Delta t} = L(i,j,k) - k\nu(\nu-\alpha)(\nu-1) - \nu w$$

$$\frac{\Delta w}{\Delta t} = \varepsilon(\nu,w)(-w - k\nu(\nu-\alpha-1)) \tag{3.10}$$

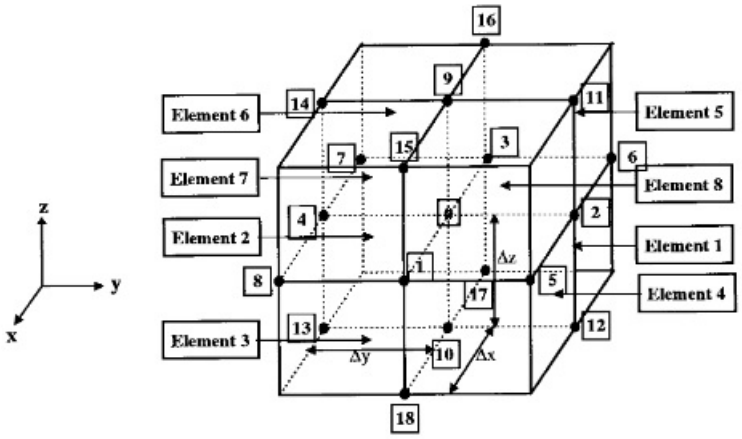

Figure 3.3: First neighbourhood of each point in heart geometry with regular elements [109].

Where L is the Laplace operator and can be calculated as:

$$L(i,j,k) = \sum_{l=0}^{18} W_l \nu(l) \tag{3.11}$$

In which (i,j,k) represents location of the node, l represent index of first order neighbourhood points (shown in Figure 3.3) of each node of interest, and the node itself. W_l represents weight values that describe the effects of neighbourhood voltages on the point of interest, and ν is the normalized voltage value of each node.

Each node on point cloud geometry of cardiac model has its own fiber orientation, which has the main role in determination of weight values. Indeed, in order to find weight values in (3.11), we firstly calculated global conductivity tensor at each mesh element using local conductivity values, and fiber orientation information of each node using (3.12) [58].

$$G = \begin{pmatrix} f_{l_1} & f_{t_1} & f_{n_1} \\ f_{l_2} & f_{t_2} & f_{n_2} \\ f_{l_3} & f_{t_3} & f_{n_3} \end{pmatrix}_{fiber} \begin{pmatrix} \sigma_l & 0 & 0 \\ 0 & \sigma_t & 0 \\ 0 & 0 & \sigma_n \end{pmatrix}_{local} \begin{pmatrix} f_{l_1} & f_{t_1} & f_{n_1} \\ f_{l_2} & f_{t_2} & f_{n_2} \\ f_{l_3} & f_{t_3} & f_{n_3} \end{pmatrix}^T_{fiber} \tag{3.12}$$

where G, represents global conductivity matrix, f_l is fiber orientation in Cartesian coordinate system, f_t, and f_n are transverse directions to fiber orientation. $\sigma_l,\ \sigma_t,\ \sigma_n$ are local electrical conductivity values in the longitudinal and two transverse directions. In this study we assumed transverse conductivities to have same values ($\sigma_t = \sigma_n$). Then, we calculate weight values using (3.13)-(3.31) [109].

$$W_1 = \frac{1}{4\Delta x^2}[\sigma_{11}(3) + \sigma_{11}(4) + \sigma_{11}(7) + \sigma_{11}(8)] \tag{3.13}$$

$$W_2 = \frac{1}{4\Delta y^2}[\sigma_{22}(1) + \sigma_{22}(4) + \sigma_{22}(5) + \sigma_{22}(8)] \tag{3.14}$$

$$W_3 = \frac{1}{4\Delta x^2}[\sigma_{11}(1) + \sigma_{11}(2) + \sigma_{11}(5) + \sigma_{11}(6)] \tag{3.15}$$

$$W_4 = \frac{1}{4\Delta y^2}[\sigma_{22}(2) + \sigma_{22}(3) + \sigma_{22}(6) + \sigma_{22}(7)] \tag{3.16}$$

$$W_5 = \frac{1}{4\Delta x\Delta y}[\sigma_{12}(4) + \sigma_{12}(8)] \tag{3.17}$$

$$W_6 = -\frac{1}{4\Delta x\Delta y}[\sigma_{12}(1) + \sigma_{12}(5)] \tag{3.18}$$

$$W_7 = \frac{1}{4\Delta x\Delta y}[\sigma_{12}(2) + \sigma_{12}(6)] \tag{3.19}$$

$$W_8 = -\frac{1}{4\Delta x\Delta y}[\sigma_{12}(3) + \sigma_{12}(7)] \tag{3.20}$$

$$W_9 = \frac{1}{4\Delta z^2}[\sigma_{33}(5) + \sigma_{33}(6) + \sigma_{33}(7) + \sigma_{33}(8)] \tag{3.21}$$

$$W_{10} = \frac{1}{4\Delta z^2}[\sigma_{33}(1) + \sigma_{33}(2) + \sigma_{33}(3) + \sigma_{33}(4)] \tag{3.22}$$

$$W_{11} = \frac{1}{4\Delta y\Delta z}[\sigma_{23}(5) + \sigma_{23}(8)] \tag{3.23}$$

$$W_{12} = -\frac{1}{4\Delta y \Delta z}[\sigma_{23}(1) + \sigma_{23}(4)] \tag{3.24}$$

$$W_{13} = \frac{1}{4\Delta y \Delta z}[\sigma_{23}(2) + \sigma_{23}(3)] \tag{3.25}$$

$$W_{14} = -\frac{1}{4\Delta y \Delta z}[\sigma_{23}(6) + \sigma_{23}(7)] \tag{3.26}$$

$$W_{15} = \frac{1}{4\Delta x \Delta z}[\sigma_{13}(7) + \sigma_{13}(8)] \tag{3.27}$$

$$W_{16} = -\frac{1}{4\Delta x \Delta z}[\sigma_{13}(5) + \sigma_{13}(6)] \tag{3.28}$$

$$W_{17} = \frac{1}{4\Delta x \Delta z}[\sigma_{13}(1) + \sigma_{13}(2)] \tag{3.29}$$

$$W_{18} = -\frac{1}{4\Delta x \Delta z}[\sigma_{13}(3) + \sigma_{13}(4)] \tag{3.30}$$

$$W_0 = -\sum_{1}^{18} W(i) \tag{3.31}$$

where indices of conductivities represent their location in the global conductivity tensor. The number in parenthesis refer to the element number in the cubic representation, as shown in Figure (3.3). Moreover Δx, Δy and Δz represent the node spacing in x, y, and z directions. W values show the effect of eighteen first neighbourhood points, and central point.

3.4 Geometry of the Heart

In this study, we used two different heart geometries obtained from dogs: (1) Auckland heart model (AHM), in which ventricular muscle geometry and fiber orientation were obtained experimentally by Nielson and colleagues in Auckland University [91]. (2) magnetic resonance (MR) based Utah heart model (UHM) and diffusion tensor (DT) based fiber orientation data [2]. In the following sections we will explain these geometries in detail.

3.4.1 Auckland Heart Model

This model was obtained by Nielson and colleagues [91] in New Zealand Auckland University. The model obtains the geometry coordinates and fiber orientations on 10 dogs ventricular geometry. The measurement was done with different spatial resolution ranging $2.5mm$ to $6mm$. During this study we used a geometry with maximum $6mm$ spatial resolution. The model has $79,860$ points, and dimensions of $8.8cm$ along x axis, $8.5cm$ along y axis and $7.9cm$ along z axis.

3.4.2 Utah Heart Model

This model is available as part of University of Utah, SCI Institute datasets [2]. The model is based on MR images of a dog's heart (ventricular geometry only) and corresponding fibrous structure of the geometry was obtained by diffusion weighted images (DWI). The magnetic resonance (MR) images were already segmented as part of the dataset, hence no additional segmentation was applied to the original MR images. However, in order to make a synchronized point cloud of ventricular geometry and fiber information, we first convert MR images of geometry to a point cloud. Next, we interpolate the point cloud to another point cloud including fiber orientation information using SCIRun software. The final geometry includes 147456 points, and has dimensions of 8.911 cm along the x- and z-axes and 11.17 cm along the y-axis, with in-slice spacing of 1.00 mm.

3.4.3 Conversion of Irregular Geometries to Regular Geometries

According to explanation in section 3.3, we need regular geometry with uniform elements for our numerical solution of Aliev-Panfilov model. Therefore, in order to divide geometry into uniform elements, we firstly inscribe the heart geometries in a cube with regular elements with $1mm$ distance between element nodes. Then, using the inverse distance weighting (IWD) interpolation method [114] we transform those information on irregular geometries into regular cubic mesh

nodes. The IDW interpolation value U from samples $U_i = U(X_i)$ at a given point X can be calculated through (3.32).

$$U(X) = \begin{cases} \frac{\sum_{i=1}^{N} \lambda_i(X) U_i}{\sum_{i=1}^{N} \lambda_i(X)}, & \text{if } d(X, X_i) \neq 0) \\ U_i, & \text{if } d(X, X_i) = 0) \end{cases} \tag{3.32}$$

Where $d(X, X_i)$ is distance between known sample points X_i and element nodes X. λ_i is a weighting value for each of sample nodes with respect to their distance from element node and can be calculated by (3.33).

$$\lambda_i = 1/d(X, X_i) \tag{3.33}$$

Converting AHM, and UHM from irregular geometry to regular geometries, we implemented IDW interpolation with accuracy of $2mm$. It means all points from irregular geometry in $2mm$ distance with a point of interest in regular cubic geometry was considered in (3.32). The final geometry remained unchanged in dimensions, but number of points changed to 252426 and 230162 in AHM and UHM respectively.

3.5 Registeration of Two Cardiac Geometries

In order to make comparison of results between two three dimensional (3D) geometries, or transferring of information from one of these geometries to the other one, we can find corresponding points on both geometries. This concept is known as registration of two geometries.

We apply four steps for registration of two geometries. Our aim is to transfer fiber orientation information from UHM (target geometry) to corresponding points on AHM (reference geometry), which will be discussed in section 4.4. These steps are depicted in Figure 3.4, and are namely; (1) body mass center overlaying (2) resizing (3) rotation and translation (4) interpolation. Note that, nodes on reference geometry (P_i^o), and nodes on target geometry ($P_i^{t_0}$) are input

for the system, and at each step target geometry is the transformed geometry of the previous step.

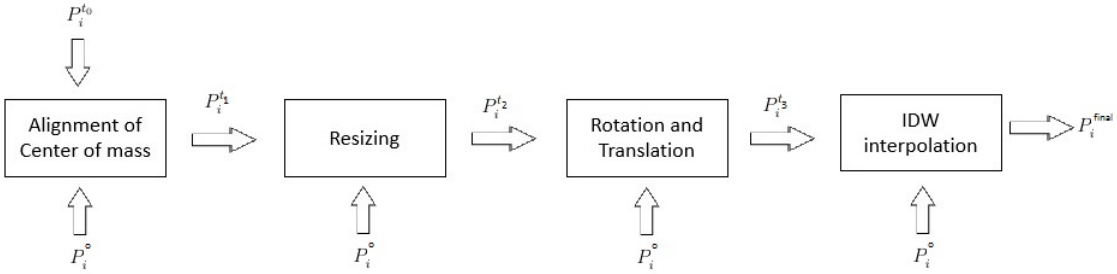

Figure 3.4: Steps for registration of two geometries.

Body mass center overlaying At first step body mass center of both reference geometry and target geometry should be overlaid on each other. To do so, we calculate body mass center of both geometries using (3.34).

$$C = \frac{1}{N}\sum_{i=1}^{N} P_i \quad \text{for } i = 1, 2, 3, ..., N \tag{3.34}$$

Where N is the number of points, and P_i are the nodes with x, y, z coordinates in the geometry. If we define C_o as the mass center of reference geometry, and C_t as the mass center of the target geometry which we want to transform, the difference between mass centers can be calculated as $C_d = C_o - C_t$. Next, by addition of distance between two body mass centers to the point coordinates of target geometry we can overlay body mass centers of both geometries (3.35).

$$P_i^{t_1} = P_i^{t_0} + C_d \tag{3.35}$$

where $P_i^{t_1}$, and $P_i^{t_0}$ are points of transformed and target geometries respectively.

Resizing In order to find corresponding of reference geometry on the target geometry we should also multiply the target geometry points with a scaling factor in order to resize it to the reference geometry's size. We use:

$$S_o(x,y,z) = max(P^o(x,y,z)) - min(P^o(x,y,z)) \tag{3.36}$$

$$S_t(x,y,z) = max(P^{t_1}(x,y,z)) - min(P^{t_1}(x,y,z)) \tag{3.37}$$

$$P_i^{t_2} = (P_i^{t_1} S_o(x,y,z))/S_t(x,y,z) \tag{3.38}$$

Where S_o, and S_t refer to size of reference and target geometries respectively, and $P_{t_2}^r$ are nodes of resized geometry.

Rotation and translation In this step we aim to find the corresponding points of the two geometries by rotating the target geometry until, it overlays with the similar points with least error. This method was successfully done in previous studies [21, 35].
We use quaternion based algorithm for rotation and translation of target geometry. The aim of rotation and translation is to find corresponding points of the target geometry (P^{t_2}) on the reference geometry (P^o). To do so, We calculate optimal unit rotational quaternion vector $\vec{q_r}$, rotational matrix R, and translational vector $\vec{q_t}$, using the method explained in appendix section. Then we can rotate and translate target geometry using:

$$P_i^{t_3} = RP_i^{t_2} + Q_t \tag{3.39}$$

Where $P_i^{t_3}$ is transformed geometry, and Q_t is a matrix obtained by repeating translation vector q_t column-wise to have same dimensions with target geometry's matrix dimensions P^{t_2}.

Interpolation Finally the last step of registration is comparing of results or transferring of information between two geometries. If we want to compare results like TMP distribution on ventricular geometries, finding the nearest point with the least Euclidean distance is reasonable [21]. However, if we want to transfer information like fiber orientation from target geometry to reference geometry IDW interpolation of target geometry information to reference geometry

shows better results, because the registration does not produce a congruence transformed geometry, which can lead to mispositioned transferring of data. Therefore, in this study different from previous works [21, 35] using of IDW in 3.40, we transferred information from not only the nearest point with larger weight value, but also nearest neighbourhood points with smaller weight values, which can minimize the amount of mispositioned transferring of information.

$$P_t^{final}(X) = \begin{cases} \frac{\sum_{i=1}^{N} \lambda_i(X) P_i^{t_3}}{\sum_{i=1}^{N} \lambda_i(X)}, & \text{if } d(P_i^o(X), P_i^{t_3}(X_i)) \neq 0) \\ U_i, & \text{if } d(P_i^o(X), P_i^{t_3}(X_i)) = 0) \end{cases} \tag{3.40}$$

Where P_t^{final} is the final transferred geometry, and λ_i is weight value for each sample nodes from target geometry $P_i^{t_3}$, with respect to their distance from reference geometry's nodes P_i^o. We chose IDW interpolation with $3mm$ accuracy. This amount of accuracy was chosen equal to maximum registration absolute error between AHM and transformed UHM. It means, all information from UHM in $3mm$ distance from points in AHM would be transfered to AHM. Amount of alteration in AHM is shown in Figure 3.5.

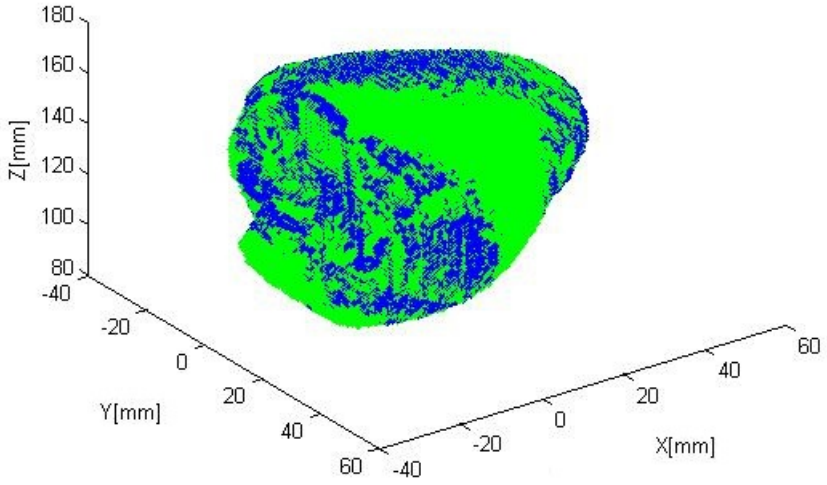

Figure 3.5: AHM (blue) and transformed UHM (green)

3.6 Comparison Metrics

In this study we use different metrics for assessing the amount of alteration in different simulation results. We compute correlation coefficient, representing quality of alteration in patterns of TMP wavefront, AP shape, AT, RT, and APD using:

$$CC = \frac{n\sum xy - (\sum x)(\sum y)}{\sqrt{n(\sum x^2) - (\sum x)^2}\sqrt{n(\sum y^2) - (\sum y)^2}} \tag{3.41}$$

where n is the number of pairs of data, x, and y are results vectors from two different simulations, and CC is correlation coefficient.

In order to compare alteration in magnitude of TMP values, we also compute absolute error (AE), relative error (RE), and norm error values (NE), that show magnitude and ratio of alteration in TMP distribution.

$$AE = |x - y| \tag{3.42}$$

$$RE = |x - y|/|y| \tag{3.43}$$

$$NE = (\sum (x - y)^2)^{1/2}/(\sum (x)^2)^{1/2} \tag{3.44}$$

Finally, we measure amount of variation or dispersion from the average value, using standard deviation (SD):

$$STD = (\frac{1}{n-1}\sum_{i}^{n}(x_i - \bar{x})^2)^{1/2} \tag{3.45}$$

Where i, shows the index of numbers in vector x, and $\bar{x}$ is the average value and can be calculated by:

$$\bar{x} = \frac{1}{n}\sum_{i}^{n}(x_i) \tag{3.46}$$

CHAPTER 4

EFFECT OF FIBER ORIENTATION ON TMP DISTRIBUTION

4.1 Introduction

Anisotropy is a property of being directionally dependent. This property can be seen at every aspect of life ranging from light emission to seismic wavefront propagation. In the heart, anisotropy mostly refers to directional variation of certain properties of propagation, which can be conduction velocity (CV), potential wavefront distribution or mechanical wavefront propagation. Typical heart is composed of fibrous structure, in which myocytes are elongated and aligned axially along these fibers. Myocyte cell, shape, size and directional distribution of gap junction as mediator of intracellular communication are factors that characterize heart as an anisotropic structure [129]. Considering mechanical contraction, is dependent on the electrical activity of the heart, we mostly focus on electrical conduction anisotropy and electrical potential distribution and propagation rather than mechanical wavefront distribution and propagation.

According to explanation in section (2.5.5.4), there is need for a model to give numerical and analytical information for understanding heart myocardial anisotropic nature using transmembrane potential as comparison factor. Because, (1) fibers responsible for contraction of the heart are located in the myocardium (2) myocardium comprise the largest volume of the heart muscle and myocardial infarction and cardiomyopathies are the major causes of heart fail-

ure and arrhythmic sudden death. In addition, TMP patterns (1) provide an accurate and comprehensive information such as action potential features (e.g. AT, DAT, AP morphology, APD, etc.) and restitution properties in addition to AT help us to analyse the wavefront pattern through different phases of AP (2) it can be the best feature to show the direct effect of anisotropy features alteration with the least computational cost and error in comparison to forward and inverse solution of electrocardiography. (3) it provides detailed information about anisotropy features in comparison to ECG, that provides mostly a general description of it.

Taking into account the cardiac anisotropy, the best method for representation of cardiac fiber orientation is the next matter of importance. The mostly used methods for obtaining fiber orientation are ex-vivo experimental fiber detection [91], diffusion tensor magnetic resonance imaging (DT-MRI) [29, 52, 121], and computational estimation of fiber orientation [14,99]. The first is very hard to apply in general, and impossible to apply for in-vivo applications. The second one is hard to apply for in-vivo applications and is subject to patient and respiratory motion artefacts, imaging artefacts and MRI noises [52]. The last method is for estimation of the fiber directions, and is not in scope of this study. Considering the constraints of these methods, the main objective of this section is to study the effects of using incorrect conductivity tensor values (either using isotropy assumption, or using noisy fiber orientations, or fiber orientations taken form another heart). The ultimate goal here is to suggest a method for representation of a sufficient fiber direction which can be obtained or calculated easily and lead to similar or close potential values to experimental potential values. At the end, we should be able to answer questions such as: whether anisotropy of the heart makes a significant alteration in our results or not, whether geometrical error related to DTI acquired fiber data affect the results, finally, whether we can use the same fiber direction for other cardiac geometries. Answering these questions can provide a perspective for the effect of geometry and fiber orientation errors and help us to suggest the easiest and accurate method for modelling anisotropic electrical activity of the heart.

In the first study, we compare the anisotropic versus isotropic simulation of electrical activity of the Auckland heart [91]. The main objective of the first study is to examine the possibility of using heart with isotropic definition. Secondly, we study the effect of the fiber orientation inaccuracy on electrical mapping of the heart by addition of random variation as white noises to fiber angles, obtained through experimental method. Finally, we investigate the possibility of fiber orientation data transfer from a known heart to a heart geometry with unkown fiber orientation.

In our simulations, we use the Auckland heart model as reference model, because this model used an experimental method for obtaining geometry and fiber information, which provides accurate and compact data with the least error [91] in comparison to Utah ventricular geometry which used DTI technique for obtaining fiber direction and is subject to several artefacts and noises [52].

4.2 Isotropy vs. Anisotropy

According to explanations in section (2.5.5.4), it has been shown that anisotropy has some effects on forward problem solution of ECG [13, 32, 50]. However, its effect on inverse problem solution of ECG is much smaller than forward problem solution [88]. Results from other anisotropic experimental studies [129] in comparison with isotropic simulations have also shown that APD is larger in direction of fiber alignment and depolarization wavefront propagation pattern is elliptical rather than spherical. It has been also shown that APD varies as much as $14ms$ in the entire heart and repolarization pattern is almost similar, but not equal to depolarization pattern propagation [120].

However, although these investigations give some qualitative and quantitative information about effects of anisotropic propagation, their information are limited and do not cover a comprehensive comparison on TMP features in detail.

Considering these results, it seems doing a comprehensive quantitative and qualitative comparison concerning all of TMP features between a heart geometry with anisotropic and isotropic conductivity values is a matter of necessity.

In this section we aim to investigate effects of anisotropy on myocardium muscle in comparison to isotropic model. To do so, we first model electrical activity of the heart with anisotropic electrical conductivity values. Doing the same simulation and using isotropic electrical conductivity values, we compare the results in order to understand reliance of TMP on anisotropic nature of the heart. We compare different TMP features such as; AP shape, activation time, recovery time, duration, TMP wavefront propagation velocity, etc.

Different local conductivity values are presented in Table 4.1, in which index (l), and (t) refer to values at the longitudinal and the transverse directions. (e), and (i) stand for values at extracellular and intracellular media. The term (iso) represents values by isotropic assumption of propagation, and the term $(ischemia)$ describes values at a heart with ischemic region. The latter will be explained more at section 5.4. In this study we use conductivity values suggested by Modre and coworkers in [88], because the study has used both the isotropic and anisotropic values which has been also used successfully in earlier works [53, 63]

Through the simulation of electrical activity of the ventricles, we stimulate the geometry from apex (ectopic heart beat). We use simulation method, which was explained in Chapter 3 for calculation of TMP wavefront distribution and propagation. We also assign Aliev-Panfilov parameters as given in Table 4.2

The entire TMP propagation takes approximately 353 ms using anisotropic conductivities and 411 ms using isotropic conductivities to span the entire ventricular volume. 3D TMP distributions are shown in Figure 4.1, and three different cross-sections in Figure 4.2, at four different time instants. The figures represent TMP distribution and propagations, in which reddish color regions describe higher potential values, and bluish regions are describing the lowest potential

Table 4.1: Different local conductivity values, used in some of studies.

conductivity values (S/m)	references
σ_l^i= 1 σ_t^i=0.05 σ_l^e=1 σ_t^e=0.333	[118, 119]
σ_l^i=0.3 σ_t^i=0.03 σ_l^e=0.3 σ_t^e=0.12	[26, 88]
σ_l^i=0.24 σ_t^i=0.024 σ_l^e=0.24 σ_t^e=0.1	[46, 107]
σ_l^i=0.1863 σ_t^i=0.0186 σ_l^e=0.1863 σ_t^e=0.0745	[15]
$\sigma_{l-iso}^i = \sigma_{t-iso}^i = 0.1$ $\sigma_{l-iso}^e = \sigma_{t-iso}^e = 0.1$	[88]
$\sigma_{l-iso}^i = \sigma_{t-iso}^i = 0.3$ $\sigma_{l-iso}^e = \sigma_{t-iso}^e = 0.3$	[26]
$\sigma_{l-ischemia}^i$= 1 $\sigma_{t-ischemia}^i$=0.05 $\sigma_{l-ischemia}^e$= 0.5 $\sigma_{t-ischemia}^e$=0.25	[118, 119]

Table 4.2: Aliev-Panfilov parameters

Parameter	Values
α	0.15
k	8
μ_1	0.006
μ_2	0.7
ϵ_0	0.004

values. Time samples are selected in a way to depict different phases of AP namely: activation, plateau, and recovery phases.

As it can be seen from Figure 4.1 and Figure 4.2 patterns, at time $t = 50$ ms a wavefront representing depolarization of ventricular myocardium spans both ventricular tissue using anisotropic and isotropic conductivity values from the apex to the base. Next, at time 150 ms to time 250 ms almost all of the tissues have been depolarized and are in plateau phase. At time 250 ms, repolarization starts to take place and at 340 ms almost entire tissue have been repolarized. Propagation is slower in isotropic ventricular geometry; propagation velocity

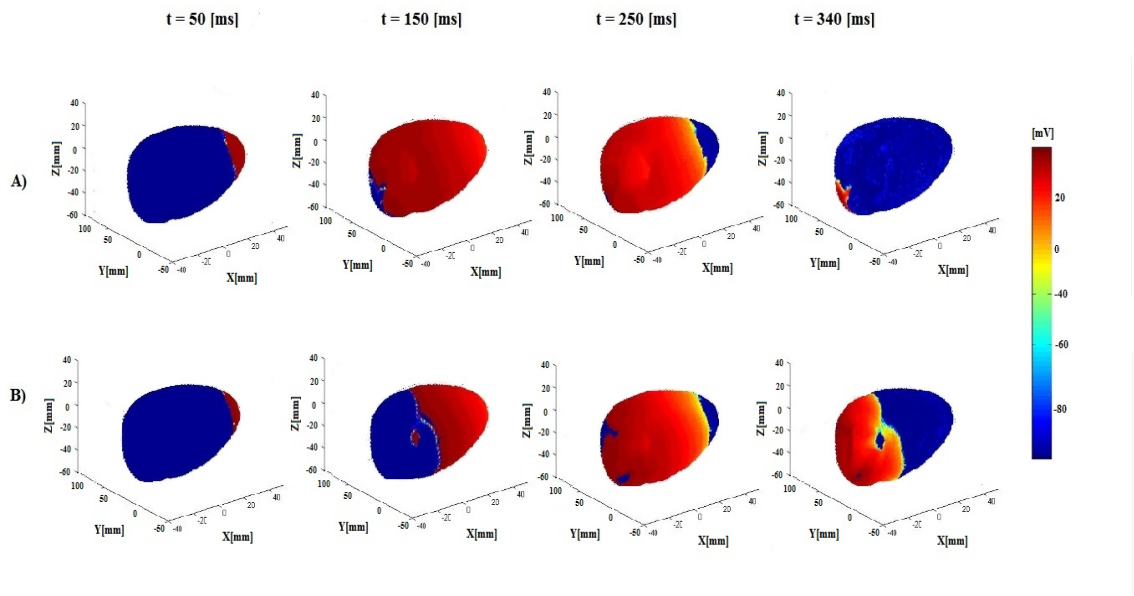

Figure 4.1: 3D TMP distributions of ventricular geometry using anisotrpic conductivity (A), and isotrpic conductivity (B) values through four time instants.

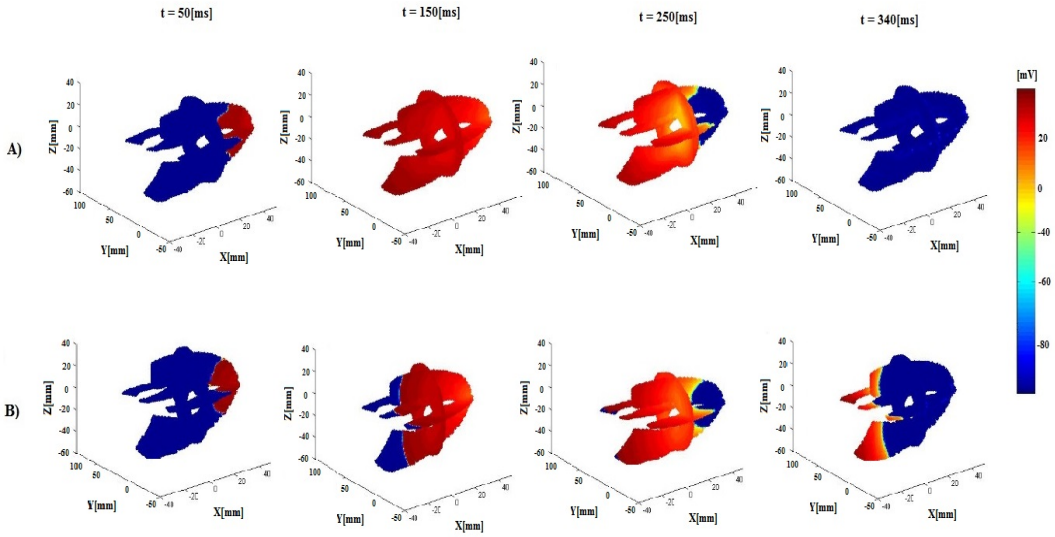

Figure 4.2: TMP distributions from three cross-sectional planes perspective of ventricular geometry using anisotrpic conductivity (A), and isotropic conductivity (B) values through four time instants.

along length of tissue (calculated by dividing propagation span time over length of cardiac tissue), are 2.21 m/s, and 2.58 m/s in isotropic and anisotropic simulations respectively, which cause a minimum 7 ms delay at early excitation time (first 10 ms of propagation) and 48.29 ms delay at late excitation times

(at final 10 ms of propagation) (Figure 4.3). This is mostly due to lower conductivity values at longitudinal direction (from 0.3 S/m in anisotropic geometry to 0.1 S/m in isotropic geometry), and higher conductivity values at transverse direction in isotropic ventricular geometry (from 0.03 S/m in anisotropic geometry to 0.1 S/m in isotropic geometry), which cause the wavefront to have slower propagation, and has mostly spherical patterns rather than diagonal patterns.

Table 4.3: Comparison between anisotropic and isotropic geometries

	TMP (mean values)	AP	AT	RT	APD
CC	0.7050	0.921	0.9745	0.9508	0.0572
MAE	19.52 (mV)	-	29.31 (ms)	28.54 (ms)	0.8810 (ms)
NE	0.4938	-	0.3614	0.1173	0.0053

In Table 4.3, we can see a mean correlation of TMP equal to 0.7050. mean correlation represents relation of alteration in potential values between both geometries from time zero to time 351 ms. However, this value is a comprehensive factor and is affected by alteration of excitation and recovery time delays, AP morphology, duration and propagation pattern that cannot be a good factor for comparison of specific details. So, we use correlation of AP as a factor to describe AP similarity of two corresponding nodes by calculation of correlation starting from excitation time to recovery time. It can be seen that there is good alignment in AP morphology of two geometries with correlation coefficient of 0.921. We also calculated a mean absolute error of 19.52 mV with standard deviation of 0.08 and mean norm error of 0.4938 with standard deviation of 0.1845 respectively. This amount of errors reveal a significant alteration of TMP values, distribution and propagation patterns between isotropic and anisotropic ventricular geometry.

Looking more in depth, in order to better understand the effect of anisotropy, we investigate alteration in AT (Figure 4.4), RT (Figure 4.5), and APD (Figure 4.6) separately. The figures are shown from three perspectives: 3D view (first columns of figures), shows changes on surface of geometries, three cross sectional planes shows (second columns of figures), and x-axis planes cross sections (third

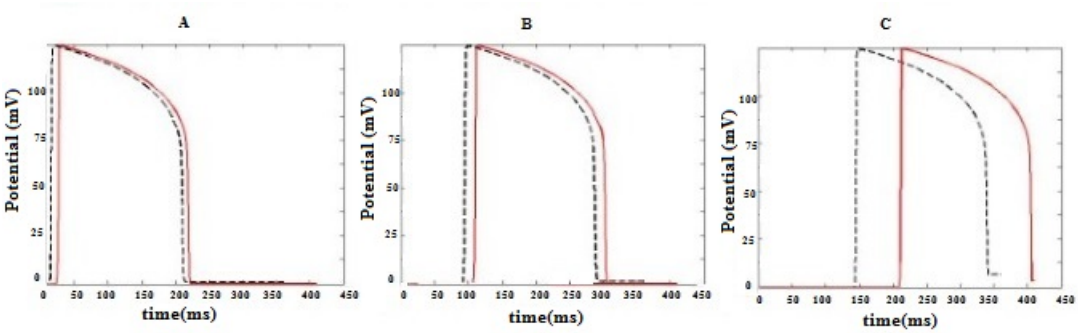

Figure 4.3: AP in ansiotropic(red) and isotropic (black) ventricular tissues through three different positions: (A) apex of tissue (B) between bas and apex of tissue (C) base of tissue.

columns of figures) depict changes within the 3D ventricular volume. The bluish regions show lower value of time scale, and reddish regions relate to higher values of time scale.

We calculated correlation coefficient of 0.9746, and 0.9758 for AT and RT respectively. We also obtained a mean absolute error of 29.31 ms, 28.54 ms, and norm error of 0.3614, and 0.1173 for AT and RT respectively. This amount of alteration shows significant change in AT and RT values, but minor change in patterns of activation, and repolarization time separately similar to results from effect of anisotropy in inverse problem solutions [88]. We also calculated a correlation coefficient of 0.9998 and 1 between excitation and recovery phases for either of anisotropic and isotropic tissues respectively, which show an alignment between excitation and recovery phase patterns similar to previous studies [129].

Moreover, we obtained a correlation coefficient of 0.0507, absolute error of about 0.9 ms, and norm error value of 0.0053 for APD between anisotropic and isotropic tissue. The low value of correlation, mean absolute error, and norm error values are an explanation for irregular, but minor changes of APD patterns. This order of distribution is shown by comparing of AP features from a series of points from ventricles base to ventricles apex (Figure 4.7). It can be seen that AT and RT alteration show a maximum amount of difference at base and minimum difference at apex of the ventricular geometry. However, dura-

tion follows irregular alteration patterns and its values change almost $8.5ms$ in isotropic geometry and $10ms$ in anisotropic geometry. We also recorded a mean amount of $1ms$ decrease in isotropic geometry duration similar to previous studies [120, 129].

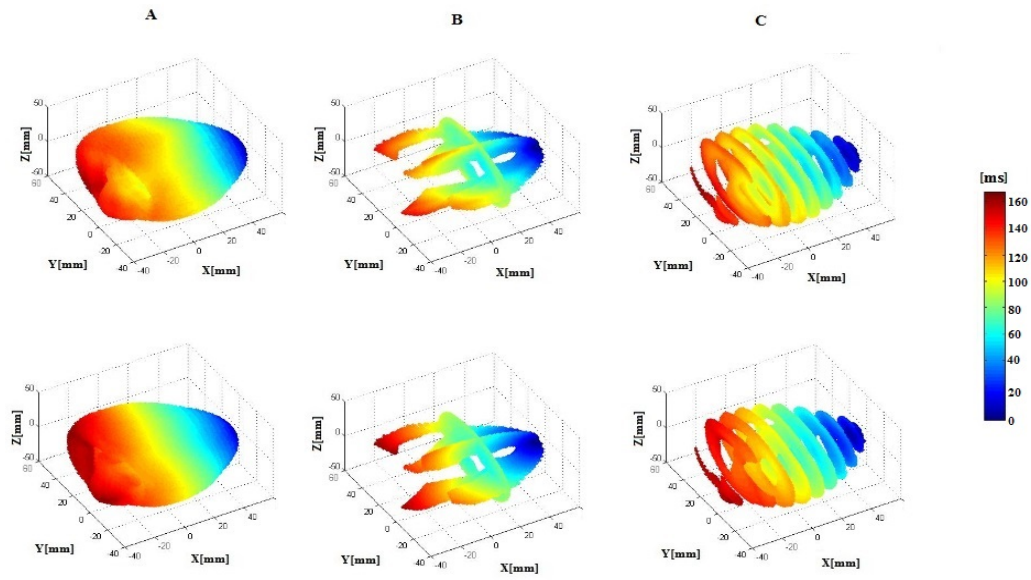

Figure 4.4: AT distribution on three dimensional ventricular geometry using anisotrpic conductivity (first row) and isotropic conductivity (2nd row) values from (A) three dimensional (B) three cross-sectional planes, and (C) several cross-sections from X-planes

4.3 Effect of Fiber Orientations Variations

It was shown that isotropic assumption of electrical conductivity, has effects on TMP distribution and propagation. Accordingly, in this section we investigate effects of fiber alignment on simulation results. Outputs from this section, also can provide an understanding of the effects of geometrical errors in obtaining fiber orientation information through different techniques like diffusion tensor imaging (DTI).

In order to investigate this kind of geometrical alteration we suppose the tissue is fixed, just like what happens in ex-vivo experiments, but its fiber direction changes. To do so, we change fiber direction obtained experimentally [91] by ad-

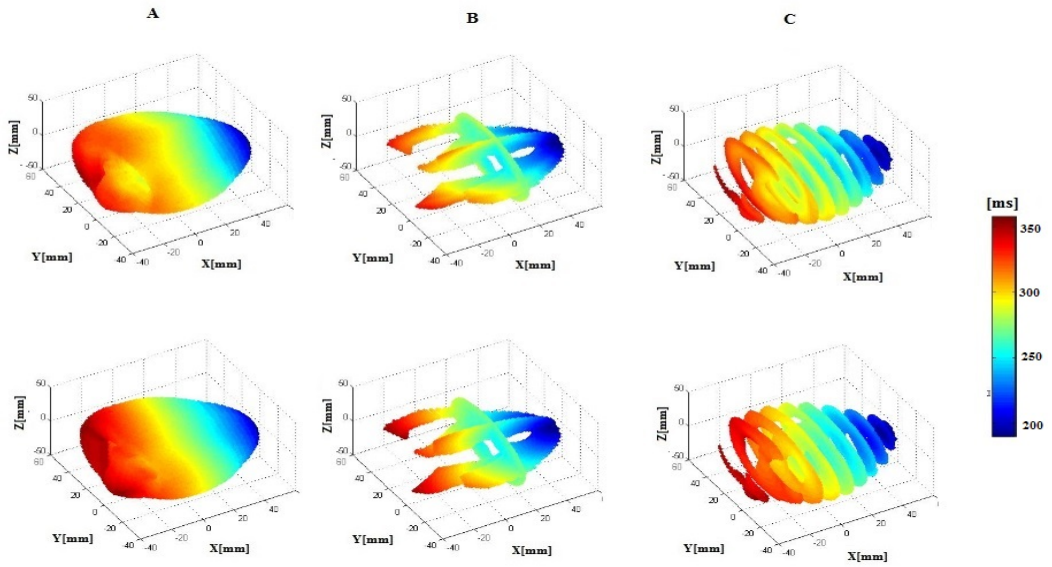

Figure 4.5: RT distribution on three dimensional ventricular geometry using anisotrpic conductivity (first row) and isotropic conductivity (2nd row) values from (A) three dimensional, (B) three cross-sectional planes, and (C) several cross-sections from X-planes

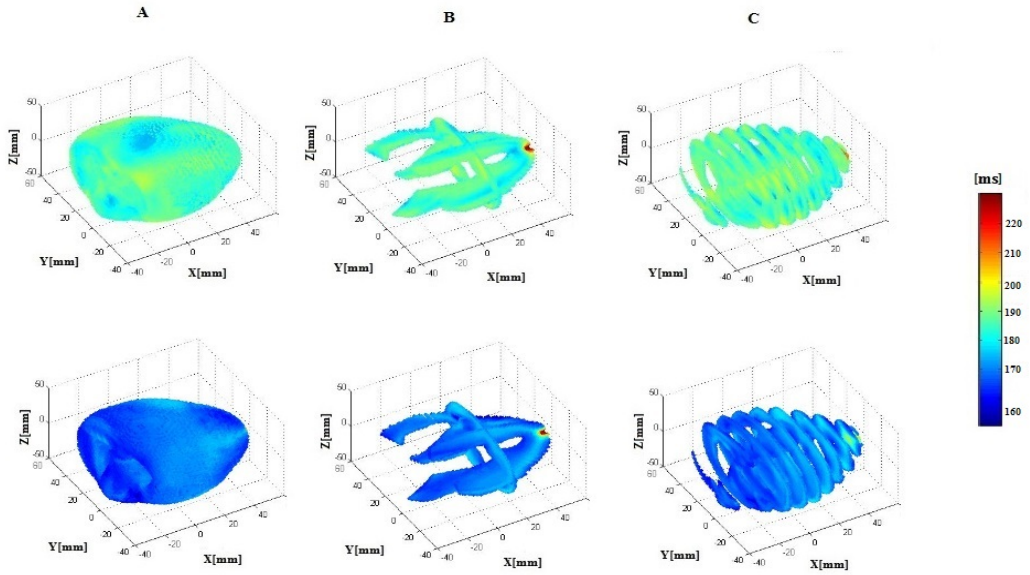

Figure 4.6: APD distribution on three dimensional ventricular geometry using anisotrpic conductivity (first row) and isotropic conductivity (2nd row) values from (A) three dimensional (B) three cross-sectional planes, (C) several cross-sections from X-planes.

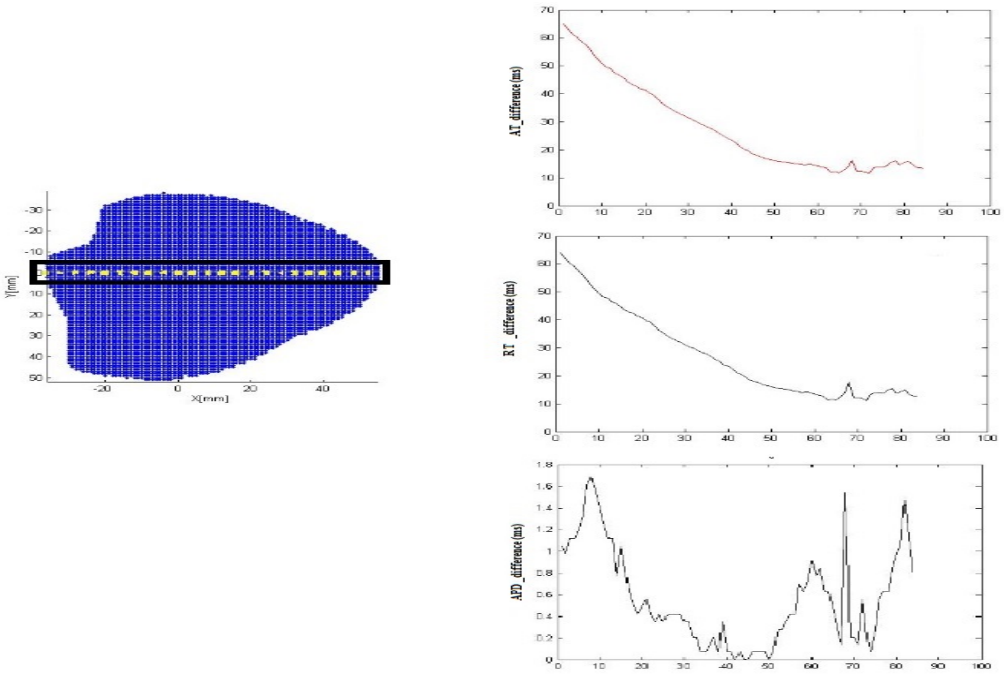

Figure 4.7: Alteration of AT, RT and APD from serial nodes from base to apex of ventricular tissue

dition of different noise values with Gaussian distribution ($n_x, n_y, n_z \sim N(0, \sigma)$) [55], and standard deviations of $\sigma = 0.1, \sigma = 0.3, \sigma = 0.5$, and $\sigma = 0.7$ using :

$$f_{l_{1-new}} = f_{l_1} + n_x \tag{4.1}$$

$$f_{l_{2-new}} = f_{l_2} + n_y \tag{4.2}$$

$$f_{l_{3-new}} = f_{l_3} + n_z \tag{4.3}$$

Where $[f_{l_1}, f_{l_2}, f_{l_3}]$ are fiber orientations in different directions, and $[f_{l_{1-new}}, -f_{l_{2-new}}, f_{l_{3-new}}]$ are new fiber orientations changed with addition of different level of noises. Next, using method explained in Chapter 3 we model ventricular TMP distribution and propagation similar to previous section. We repeated simulation method three times for the same sigma values. The qualitative comparison metrics for all runs were calculated separately, but the average results are represented in Tables 4.4-4.7 and Figures 4.10, 4.14. Our aim by repeating of simulation and representing of average values, is reducing the contribution of error values originated by probabilistic distribution of noise addition to fiber

orientation. Note that, TMP, AT, RT, and APD distribution are depicted for only one of these runs (Figures 4.8, 4.9, 4.11-4.13).

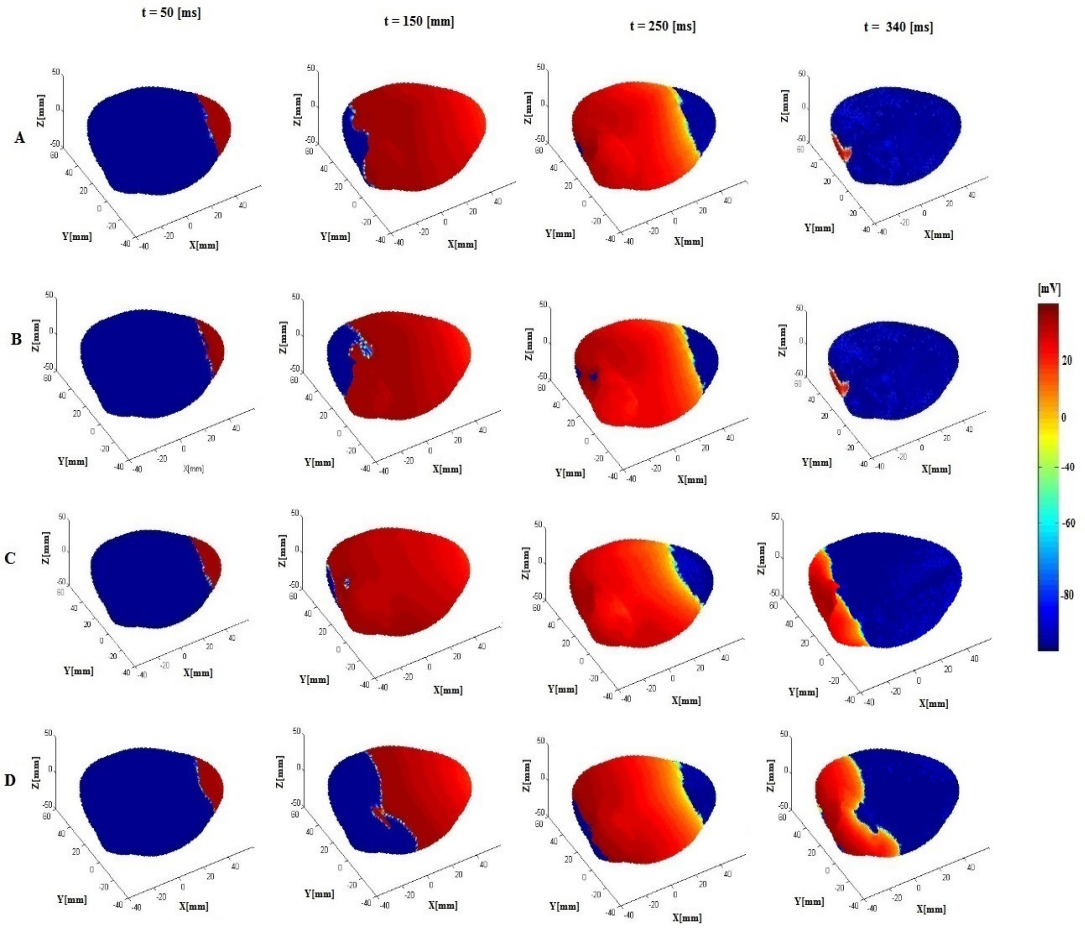

Figure 4.8: TMP distribution on ventricular tissue from 3D view with A) fiber orientations with $\sigma = 0.1$ B) fiber orientations with $\sigma = 0.3$ C) fiber orientations with $\sigma = 0.5$ D) fiber orientations with $\sigma = 0.7$.

Figure 4.8, and Figure 4.9 shows TMP distribution through geometries with four instant fiber variances of $\sigma = 0, \sigma = 0.1, \sigma = 0.3, \sigma = 0.5$, and $\sigma = 0.7$ from three dimensional and cross-sectional perspective similar to previous section. It is obvious that TMP distribution patterns and conduction velocity at low level of noise values (with standard deviation of $\sigma = 0.1$, $\sigma = 0.3$) does not change significantly, but the conduction velocity at higher noise levels (with standard deviation of $\sigma = 0.5$, $\sigma = 0.7$) reduce the conduction velocity in cardiac volume.

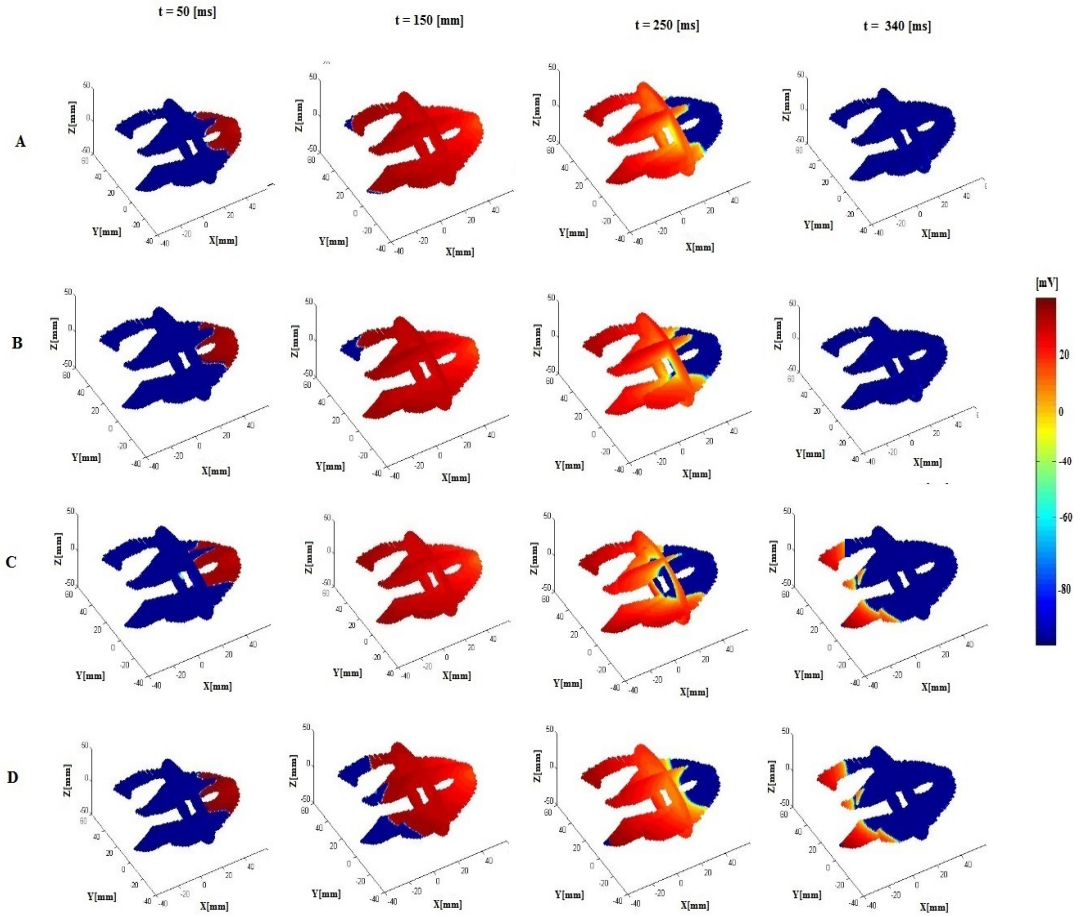

Figure 4.9: TMP distribution on ventricular tissue from three cross-sectional views with A) fiber orientations with $\sigma = 0.1$ B) fiber orientations with $\sigma = 0.3$ C) fiber orientations with $\sigma = 0.5$ D) fiber orientations with $\sigma = 0.7$.

Table 4.4 shows that mean correlation coefficient of TMP distribution does not change significantly, but decreases regularly from 0.9842 to 0.8323 with respect to increase of fiber orientation variance (Figure 4.10.A). In addition, our results show that not just TMP distribution, but also AP morphologies are not changed so much with regular decrease in AP shape with mean correlation coefficient from 0.9851 to 0.9214 (Figure 4.10.B). Moreover, mean absolute error and mean norm error of TMP distribution between original tissue and tissue with fiber orientation variance increase regularly from 1.7 mV and 0.1042 at tissue with $\sigma = 0.1$ fiber orientation variance to 11.68 mV and 0.3497 at tissue with $\sigma = 0.7$ fiber orientation variance respectively (Figure 4.10.C and Figure 4.10.D), which are an explanation for minor alteration of TMP due to fiber orientation

variances.

Span time of TMP wavefront, from apex to base of ventricular tissue by including four level of fiber orientation variances, changes maximally 33 ms, and increase regularly with increasing noise values. Wavefront propagation velocity as a consequence of span time changes between 2.54 m/s to 2.32 m/s, and decrease regularly with respect to increase in noise values.

Table 4.4: Comparison of fiber direction variance effect on TMP using the mean values of each metric over three different experiments.

σ	MCCTMP	MCCAP	MAE(mV)	MNE	WFST(ms)
0.1	0.98 ± 0.0058	0.9851 ± 0.0016	1.7 ± 0.0037	0.1042 ± 0.0226	354.17 ± 10
0.3	0.9321 ± 0.0225	0.9736 ± 0.0116	5.35 ± 0.0121	0.2233 ± 0.0406	362.92 ± 14
0.5	0.8862 ± 0.0259	0.9521 ± 0.0109	8.35 ± 0.0130	0.2876 ± 0.0306	366.31 ± 18
0.7	0.8323 ± 0.0668	0.9214 ± 0.0197	11.68 ± 0.0337	0.3497 ± 0.0823	387.87 ± 12

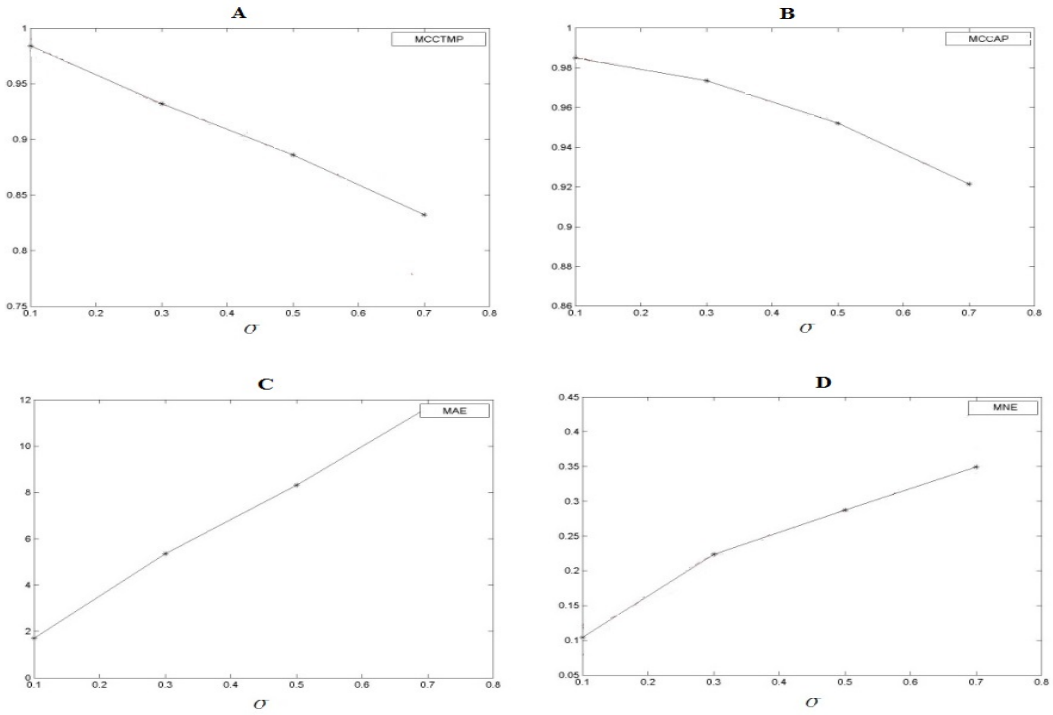

Figure 4.10: Comparison of TMP distribution between ventricular geometries with different fiber orientation variances and original ventricular geometry (A) correlation coefficient between TMP distributions (B) correlation coefficient between AP morphologies (C) absolute error between TMP distributions (D) norm error between TMP distributions.

Looking more in depth, we also investigate effect of micro-structural changes in

detail. Comparison between AT, RT and APD of original ventricular geometry and four different ventricular geometries with fiber orientation with standard deviation of $\sigma = 0.1$, $\sigma = 0.3$, $\sigma = 0.5$, and $\sigma = 0.7$ are shown from different perspectives in Figure 4.11, Figure 4.12 and Figure 4.13 respectively. It can be seen that the pattern changes are not significant in any of these three features of AP. Table 4.5, Table 4.6, and Table 4.7 we can also see a good correlation coefficient of AT, RT, and APD between original tissue and altered geometries. However, the correlations decrease by increase of fiber orientation variance and this amount of decrease is more obvious for APD (Figure 4.14).

Furthermore, we obtained a mean absolute error and norm error with maximum values of 17.07 ms and 0.2214 for AT, 16.90 ms and 0.0730 for RT, and 0.5442 ms and 0.0036 for APD, which shows smaller changes in magnitude of AP features by addition of high level of noise values. Figure 4.10 we can see that amount of alteration in error values decrease by increasing in fiber orientation variance and error values has the least alteration on APD.

Table 4.5: Comparison of AT between original tissue and geometries with different fiber orientation variances using the mean values of each metric over three different experiments.

σ	CCAT	MAE(ms)	NE
0.1	0.9967 ± 0.0014	2.3538 ± 0.06559	0.0305 ± 0.0083
0.3	0.9723 ± 0.0004	9.4246 ± 0.0001	0.0979 ± 0.0277
0.5	0.9554 ± 0.0080	11.8192 ± 0.2539	0.1566 ± 0.0354
0.7	0.9544 ± 0.0122	17.0729 ± 0.6383	0.2214 ± 0.0877

Table 4.6: Comparison of RT between original tissue and geometries with different fiber orientation variances using the mean values of each metric over three different experiments.

σ	CCRT	MAE(ms)	NE
0.1	0.9969 ± 0.0014	$2.3194 \pm 0.0.639$	0.0100 ± 0.0027
0.3	0.9732 ± 0.0009	7.4680 ± 0.2189	0.0322 ± 0.0090
0.5	0.9571 ± 0.0081	0.0516 ± 0.02496	0.0516 ± 0.0117
0.7	0.9559 ± 0.0118	16.9062 ± 0.6384	0.0730 ± 0.0292

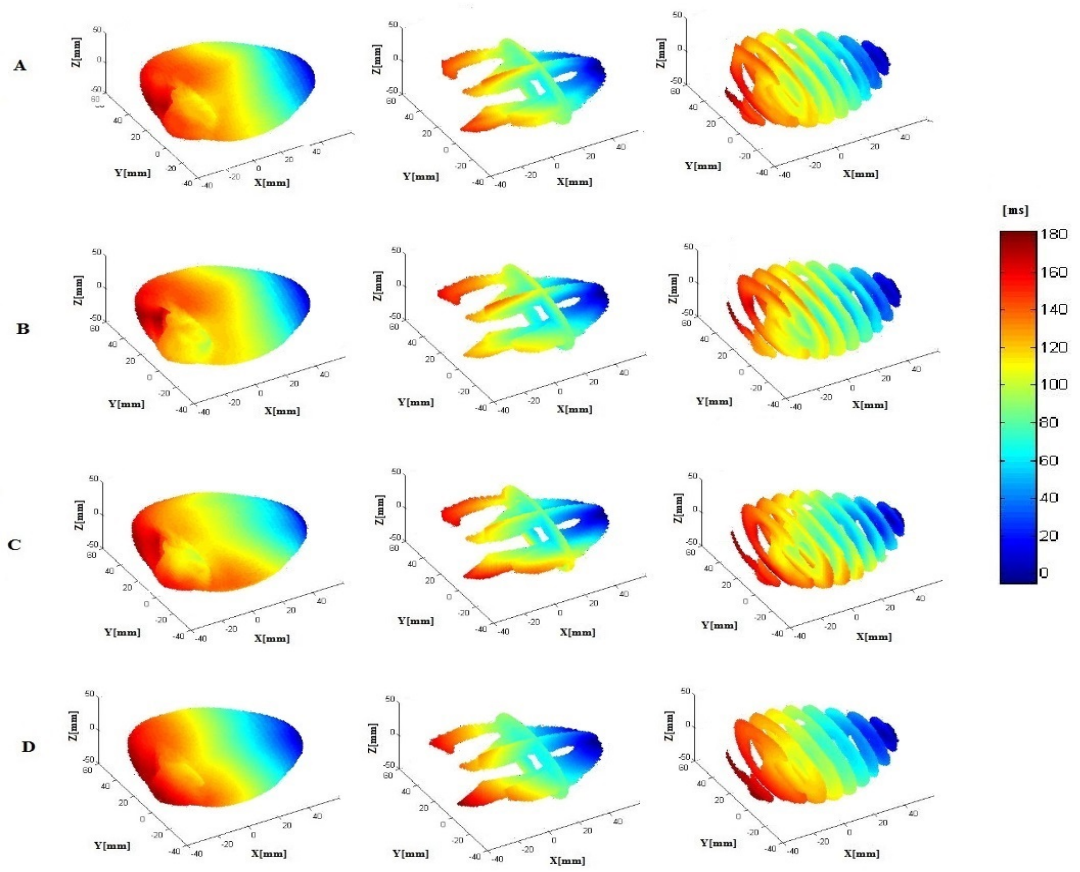

Figure 4.11: AT distribution on geometries with A) fiber orientations with $\sigma = 0.1$ B) fiber orientations with $\sigma = 0.3$ C) fiber orientations with $\sigma = 0.5$ D) fiber orientations with $\sigma = 0.7$.

4.4 Using Fiber Orientation of One Heart to Model Electrical Activity in Another Heart

In this part we study the feasibility of transferring fiber orientation information from a heart to another heart. The main objective here is to estimate electrical activity of a heart without information about its fiber orientation. We chose Auckland heart model (AHM), as the reference geometry, for which we want to estimate the electrical activity, and we transfer the fiber orientation from the Utah heart model (UHM) to the AHM. Then we compare the TMP distribution and propagation in the original AHM, and the AHM with the new fiber orientations. We used a registration method, that was explained before in section

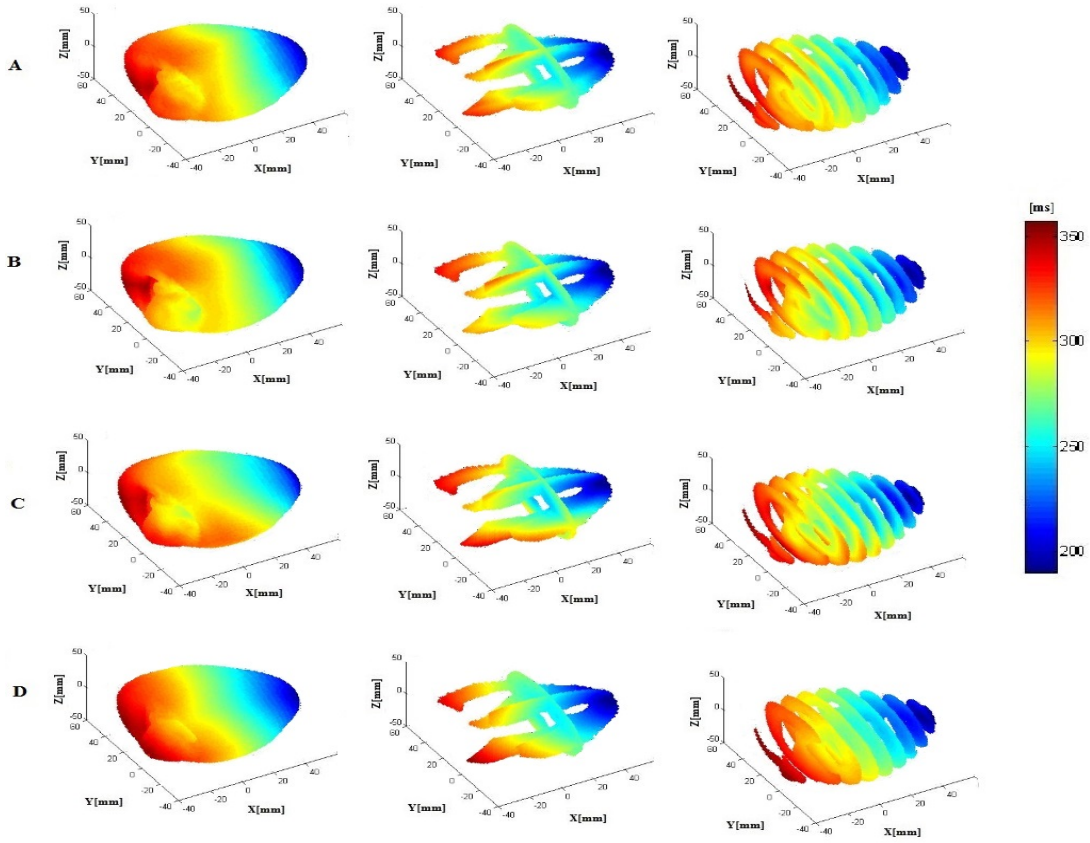

Figure 4.12: RT distribution on geometries with A) fiber orientations with $\sigma =$ 0.1 B) fiber orientations with $\sigma = 0.3$ C) fiber orientations with $\sigma = 0.5$ D) fiber orientations with $\sigma = 0.7$.

3.5 to transfer the fiber orientations of UHM onto AHM. Finally by applying a similar method as in the previous sections we would be able to simulate TMP distribution and propagation (Figure 4.15, and Figure 4.16).

Figure 4.15, and Figure 4.16 show small, but not imperceptible changes in TMP distribution and propagation. The first effect of fiber orientation transfer can be seen on span time of propagation from apex to base of ventricular tissue, which increases from 353 ms to about 370 ms and leads to decrease in propagation velocity from 2.58 m/s to 2.46 m/s. The AP delay time increase from 0.14 ms in apex to 65.03 ms at the base of ventricular tissue with transferred fiber orientations (Figure 4.21).

In Table 4.8, we also obtained a mean correlation of 0.8939, and 0.9692 for TMP

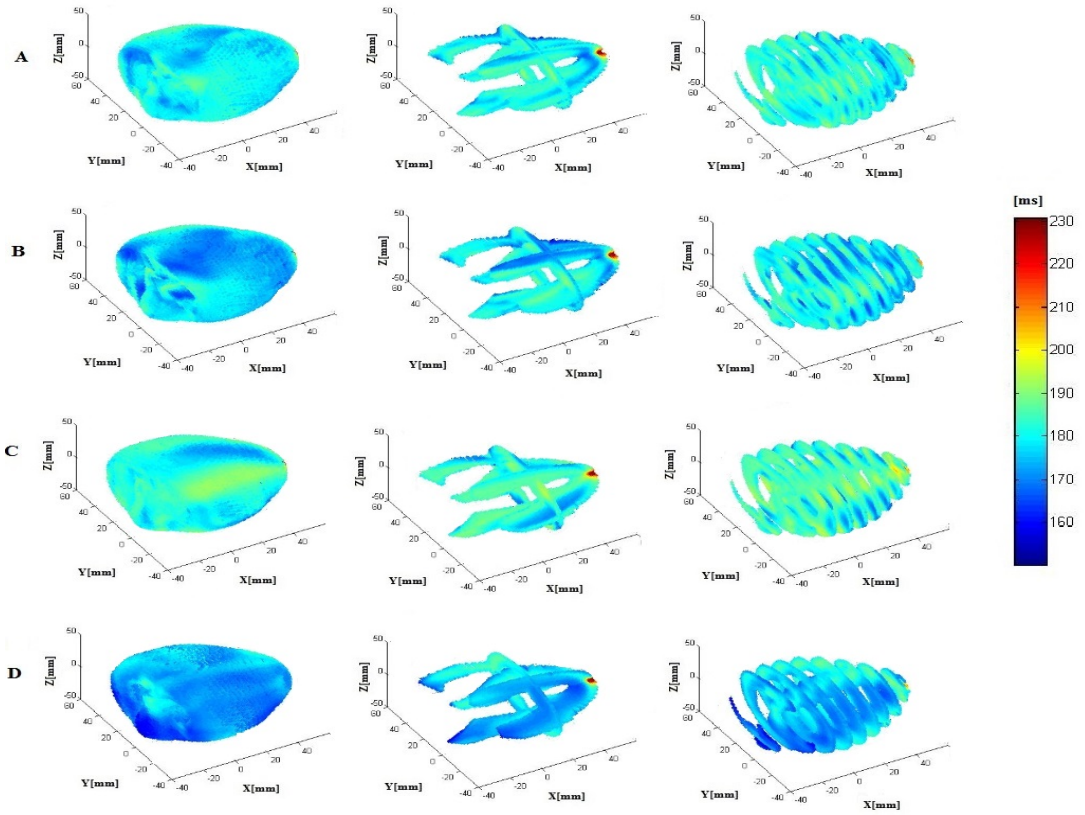

Figure 4.13: APD distribution on geometries with A) fiber orientations with $\sigma = 0.1$ B) fiber orientations with $\sigma = 0.3$ C) fiber orientations with $\sigma = 0.5$ D) fiber orientations with $\sigma = 0.7$.

distribution and AP morphology similarity, respectively. The mean absolute error was 7.89 mV with standard deviation of 0.0436, and the mean norm error was calculated as 0.2828 with standard deviation of 0.1451. This amount of alteration in error values are clue for reasonable estimation of TMP distribution and propagation using registration method.

Comparing effect of registration on AP features in detail, we calculated a correlation of 0.9502, 0.9508, and 0.2429 for AT, DAT, and APD between original and registered geometries. We also calculated mean absolute error of 11.16 ms, 11, 07 ms, and 0.59 ms for AT, DAT, and APD respectively. The norm error for the same features were recorded as 0.1469, 0.00469, and 0.0040. The highest values of correlation coefficient and low error values of AT and RT shows a good estimation of AT and RT. In addition, low amount of APD alteration

Table 4.7: Comparison of APD between original tissue and geometries with different fiber orientation variances using the mean values of each metric over three different experiments.

σ	CCAPD	MAE(ms)	NE
0.1	0.8949 ± 0.0534	0.1637 ± 0.0429	0.0012 ± 0.0003
0.3	0.5990 ± 0.0784	0.3624 ± 0.0454	0.0025 ± 0.0003
0.5	0.3424 ± 0.01159	0.4943 ± 0.0635	0.0034 ± 0.0004
0.7	0.2527 ± 0.01360	0.5442 ± 0.0855	0.0036 ± 0.0004

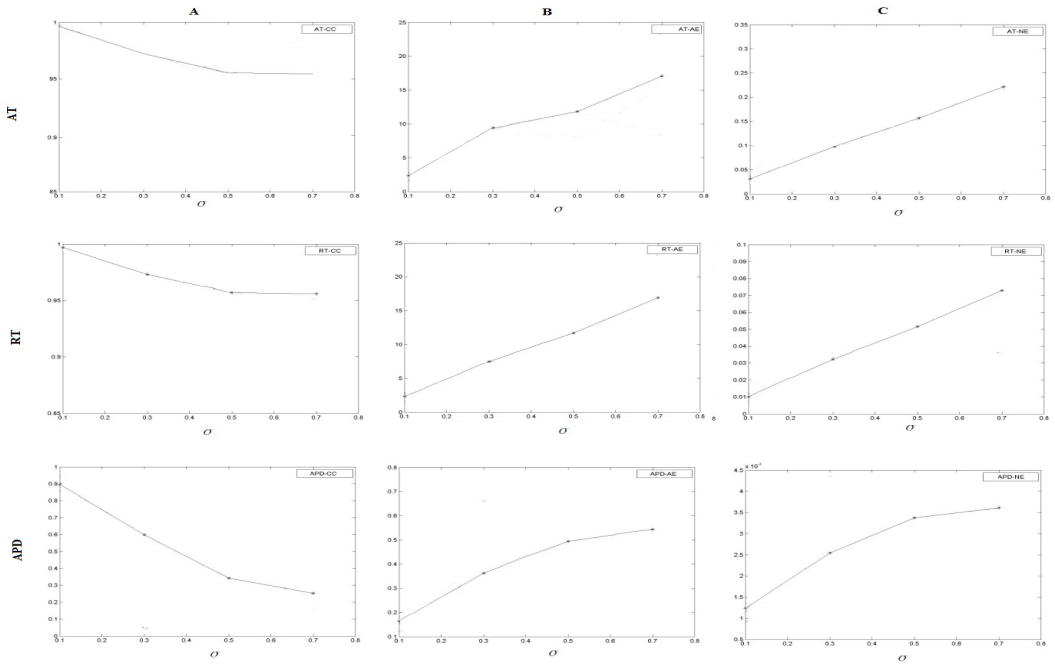

Figure 4.14: TMP distributions on ventricular tissue with (A) real fiber orientation (B) fiber orientations with 0.005 variance (C) fiber orientations with 0.02 variance (D) fiber orientations with 0.05 variance

error values show successful estimation of APD values. Accordingly, recording TMP from points between base and apex (Figure 4.21), depicts regular AT and RT differences between original and registered geometries starting from base to apex. However, changing of APD through the same points do not follow a regular pattern.

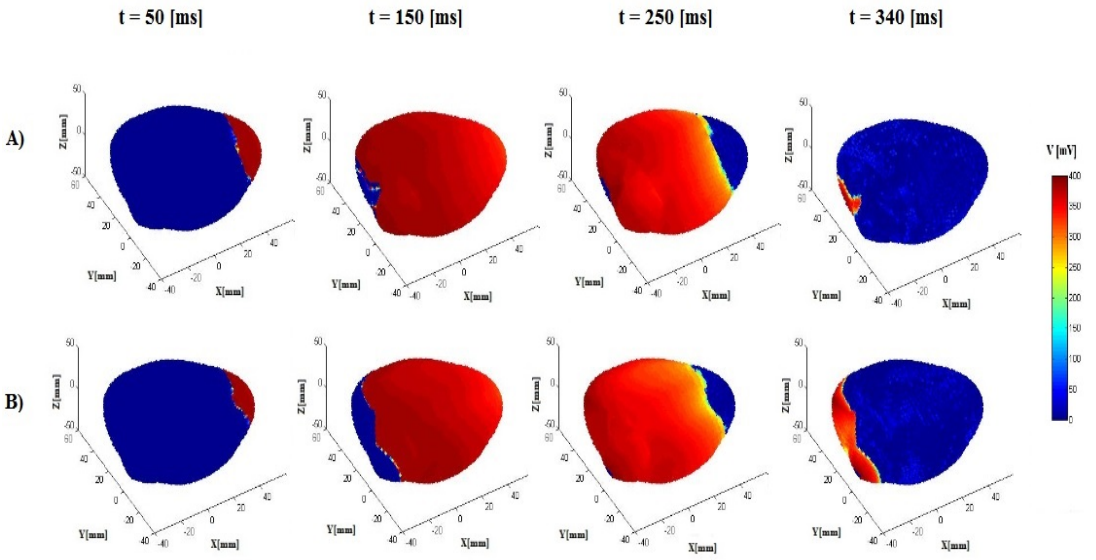

Figure 4.15: TMP distribution through four time instant from 3D perspectives on (A) original ventricular tissue (B) registered ventricular tissue.

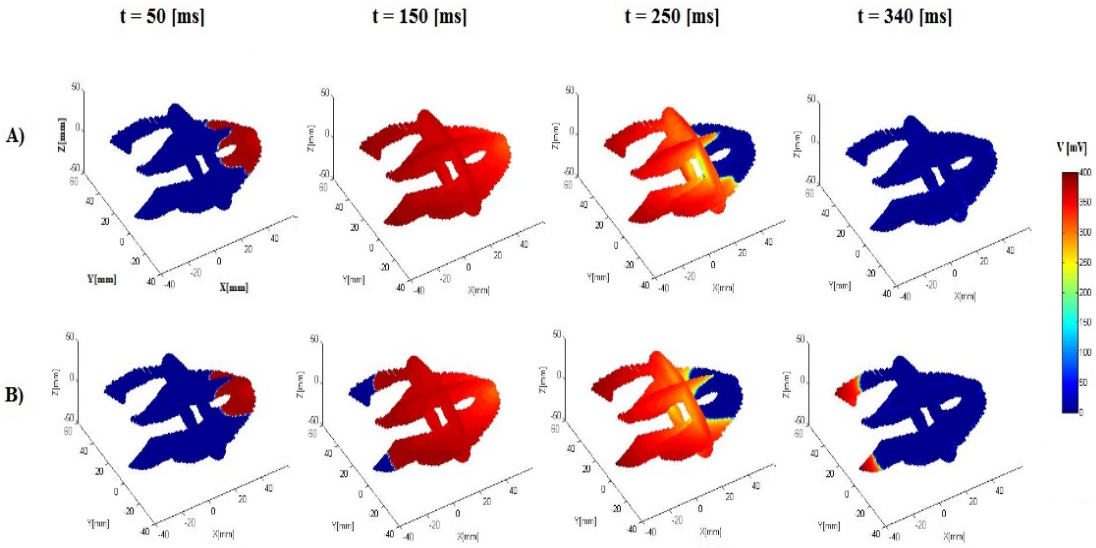

Figure 4.16: TMP distribution through four time instant from three cross-sectional planes on (A) original ventricular tissue (B) registered ventricular tissue.

4.5 Discussion

The main objective of this chapter was to suggest a practical, accurate and easy method for representing the anisotropic nature of cardiac electrical activity. It

Table 4.8: comparison of TMP features between original geometry and transformed geometry.

	TMP (mean values)	AP	AT	RT	APD
CC	0.8939	0.9692	0.9502	0.9508	0.2429
MAE	7.89 (mV)	-	11.16 (ms)	11.07 (ms)	0.5990 (ms)
NE	0.2828	-	0.1469	0.0485	0.0053

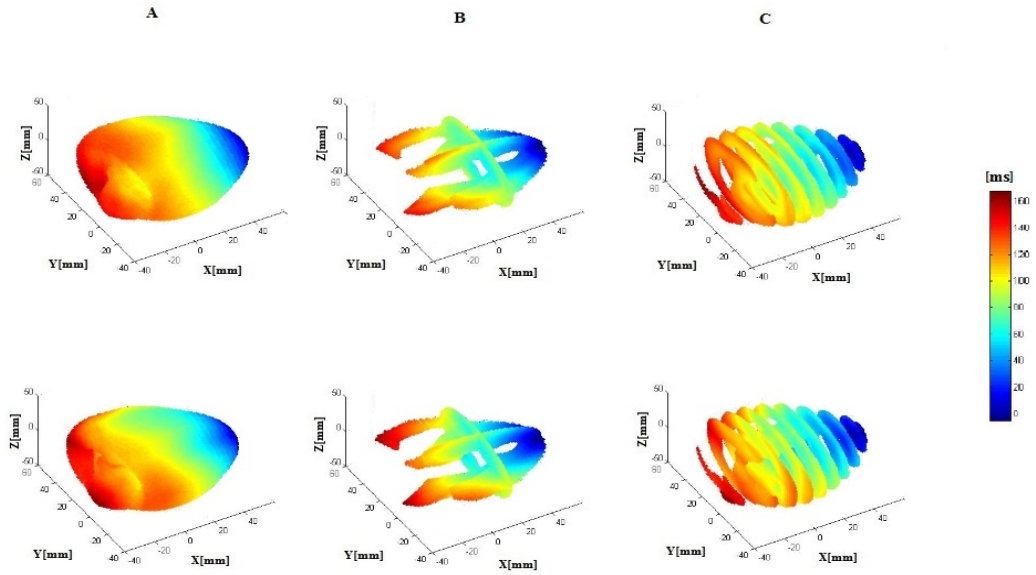

Figure 4.17: AT distribution on three dimensional ventricular geometry on original geometry (first row) and transformed geometry (2nd row) values from (A) three dimensional (B) three cross-sectional planes, and (C) several cross-sections from X-planes.

was shown that isotropic assumption of cardiac tissue can affect TMP simulation results significantly. This alteration was shown chiefly in TMP wavefront propagation velocity, TMP potential value of each point and more importantly APD of AP. However, we observed a good estimation of AP morphology, recovery phase and excitation phase. Conversely, it was shown that fiber orientations variance, resembling geometry errors which happens through different fiber data acquisition methods like DTI, does not affect the results of simulations significantly due to minimal changes in TMP features by altering fiber orientation even with standard deviation of $\sigma = 0.7$. Finally, it was shown that registration of fiber information can be considered as a possible method for easy modelling of electrical activity. This method was successful in modelling of TMP values, AT,

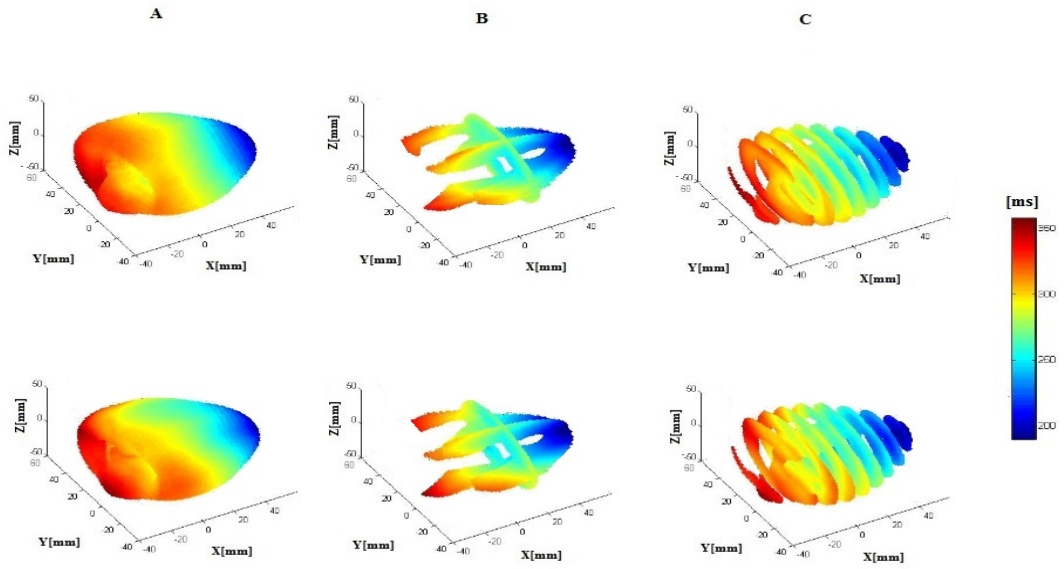

Figure 4.18: RT distribution on three dimensional ventricular geometry on original geometry (first row) and transformed geometry (2nd row) values from (A) three dimensional (B) three cross-sectional planes, and (C) several cross-sections from X-planes.

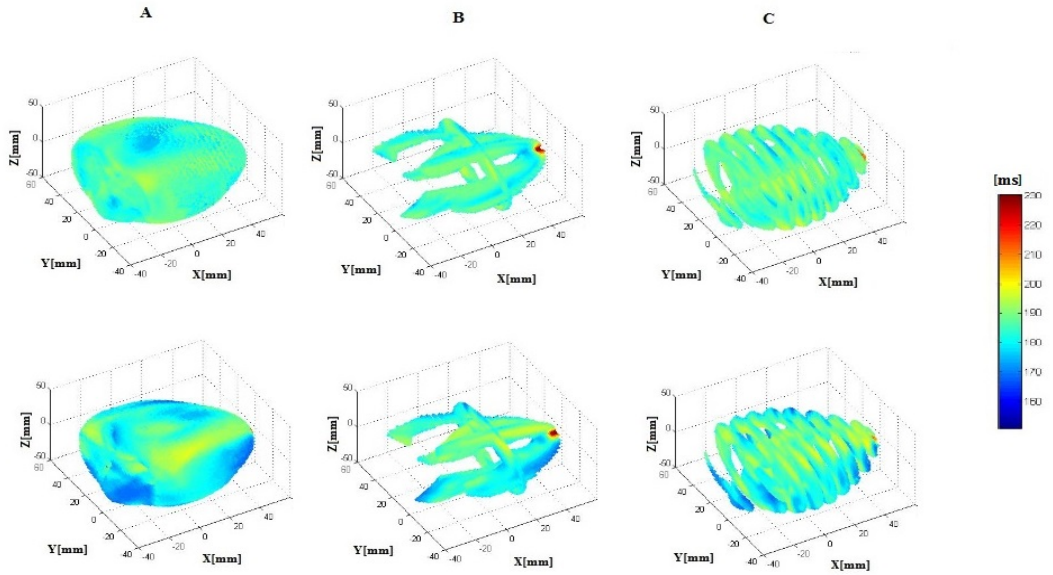

Figure 4.19: APD distribution on three dimensional ventricular geometry on original geometry (first row) and transformed geometry (2nd row) values from (A) three dimensional (B) three cross-sectional planes, and (C) several cross-sections from X-planes.

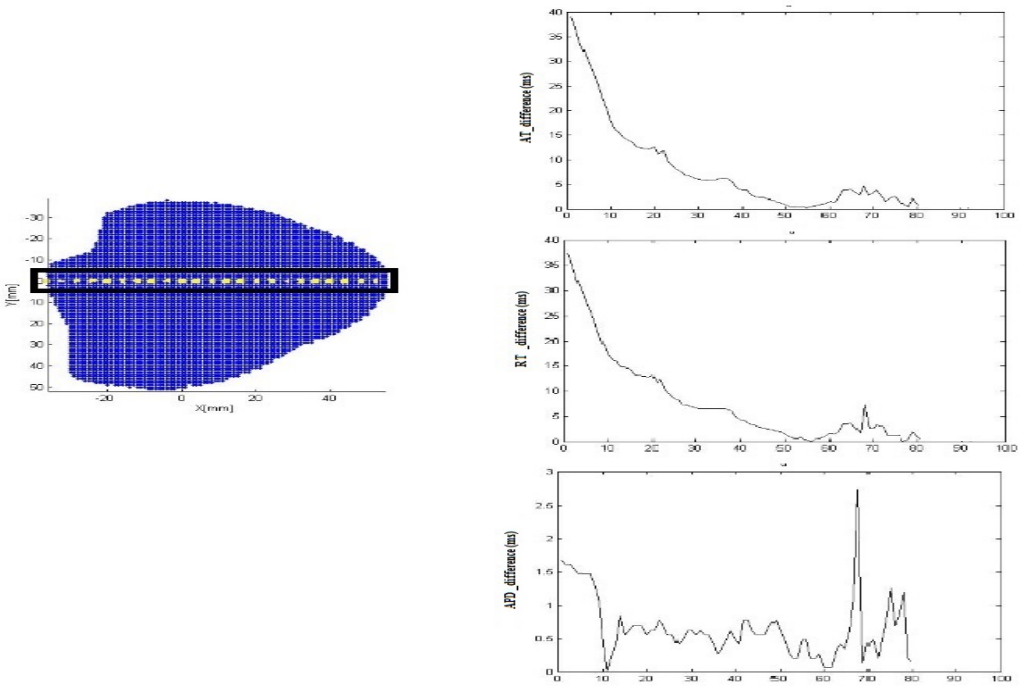

Figure 4.20: Comparison of (A) AT, (B) RT, (C) APD alteration between original and registered geometries from base to apex.

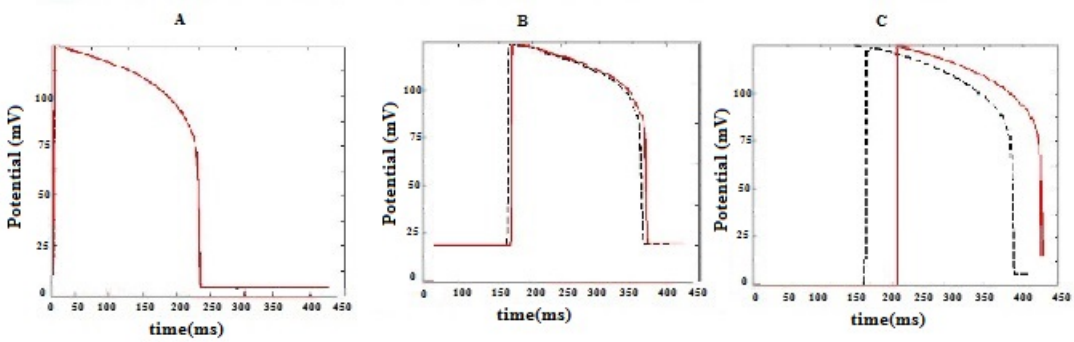

Figure 4.21: AP from three position of anisiotropic(red) and transformed (black) ventricular tissue through three position (A)apex (B) between bas and apex (C) base.

RT and APD distributions with a reasonable correlation and low absolute and norm error values. Besides, the fiber information in target geometry of UHM has been obtained through DTI technique. It means, not just registration itself, but also errors originated from DTI technique, affected the estimation accuracy. The accuracy of the results can be improved even further by using more accurate fiber orientation acquisition method.

CHAPTER 5

SIMULATION OF DIFFERENT HEART CONDITIONS

5.1 Introduction

Previous chapter, it was shown that anisotropy feature of cardiac tissue should be included in modelling of its electrical activity. Furthermore, it was shown that not just anisotropic feature, but also fiber orientation can affect results. However, the alteration due to fiber orientation variance was minor in comparison to isotropic assumption of electrical conductivities.

Following the results from previous chapter, the main objective of this chapter is to introduce a new integrated 3D and patient specific model to simulate different functional states of the left and right ventricular tissue, including anisotropic feature of cardiac tissue based on TMP distributions. To do so, we use UHM, in which geometry and fiber informations are obtained noninvasively through MR, and DTI techniques. Our purpose is to suggest a tool for simulation different cardiac arrhythmias for diagnosis, prediction and estimation of different cardiac diseases.

We first, modeled normal functional state of the heart, in which heart beats arise from the SA node. Next, we focused on focal arrhythmia, in which beats arise from a stimulation site at ventricles, called the ectopic heart beats. We also simulated TMP propagation on a ventricular geometry with partially ischemic region. This kind of cardiac disease results in deterioration of electrical and mechanical activity of the heart, and can be observed as action potential morphology alteration and contraction failure respectively. Finally, another cardiac disorder, called Wolf-Parkinson White (WPW) syndrome, which is caused due

to abnormal electrical conduction pathways was simulated.

5.2 Electrical Activity of the Ventricular Tissue with Normal Heart Beats

In this section, we aim to simulate electrical activity of normal heart beats in the UHM. Since our model encompass electrical activity on the ventricles rather than atria, we need a way to model how the activity passes from the AV node to the ventricles. So, in fact this is a model of ventricular propagation starting with bundles and purkinje fibers. Accordingly, three initial stimulation sites were defined to initiate TMP distribution and propagation on UHM. These sites of stimulation were chosen according to early studies on human isolated heart [41], and is shown in Figure 5.1. To start the propagation, initial stimulation was initiated at the left ventricular septal wall. Then, at time 5 ms to 7 ms a second stimulation was initiated from the anterior of the left ventricle. Finally, from $15ms$ to $17ms$ another stimulation was initiated from the anterior of the right ventricle. Then, using the TMP simulation method explained in Chapter 3, we obtained TMP distribution and propagation. We define intracellular local conductivity as 0.16 S/m in the direction parallel to the fibers and 0.016 S/m in directions perpendicular to fiber. Similarly, we define extracellular longitudinal conductivity as 0.16 S/m and perpendicular conductivities as 0.05 S/m respectively. These conductivity values are calculated by computational evaluation of conductivity values [118], and their relations [119]. We also define Aliev-Panfilov parameters similar to previous simulation in Chapter 4.

Table 5.1: Local conductivity values

Compartment	Conductivity (S/m)	
anisotropic	$\sigma_l^i = 0.16$	$\sigma_t^i = 0.016$
conductivity	$\sigma_l^e = 0.16$	$\sigma_l^e = 0.05$

In Figure 5.2, the TMP distribution and propagation is shown at 5 time instants from 3D view, tree cross-sectional view, and several X-plane cross-sections. The reddish regions are regions with maximum potential values, and bluish regions are related to regions with lowest potential values. Time instants are chosen

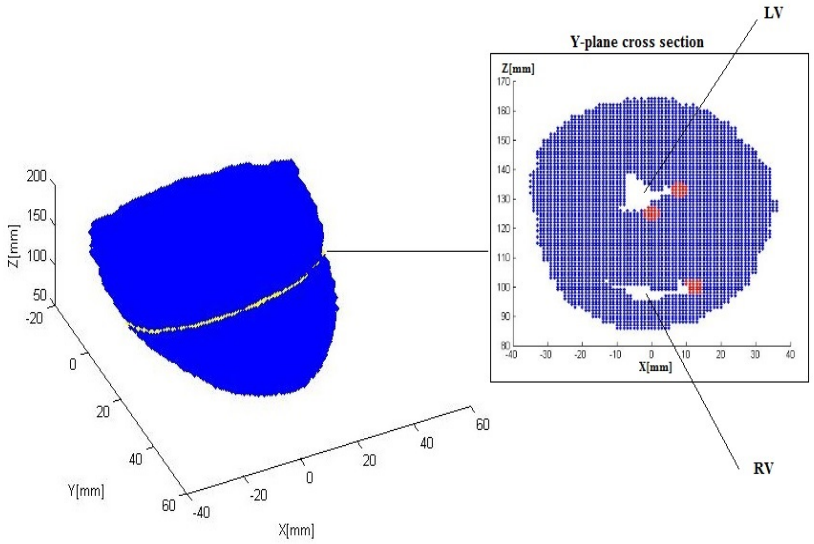

Figure 5.1: Initial stimulation sties on UHM with normal heart beats (shown in red circles).

in a way to depict different phases of AP such as depolarization, plateau, and repolarization phases. It can be seen that at time 30 ms, the depolarization of UHM starts from the subendocardial wall, and at time 45 ms, depolarization starts to cover subepicardial wall of the UHM. Then, at 125 ms, almost entire ventricular tissue has been depolarized, showing plateau phase of AP in cardiac cells. Finally, at 210 ms, repolarization phase starts from the subendoracdial wall, and at 230 ms, almost all tissue has been depolarized. It takes almost 235 ms for TMP distribution to span the entire ventricular tissue. The AP amplitude is 125 mV, mean APD is almost 195 ms, and resting potential is $-85mV$.

Looking at Figure 5.3, it is observed, that the earliest activation occurs at the subendocardial wall and late activation occurs at the subepicardial wall. Similar, but not exactly the same alteration can also be seen in the RT distribution (Figure 5.4). It takes almost 50 ms for activation of all cells in the ventricular tissue. APD values changes approximately by 10 ms among cells and the maximum potential values can be seen in regions near the first stimulated sites (Figure 5.5).

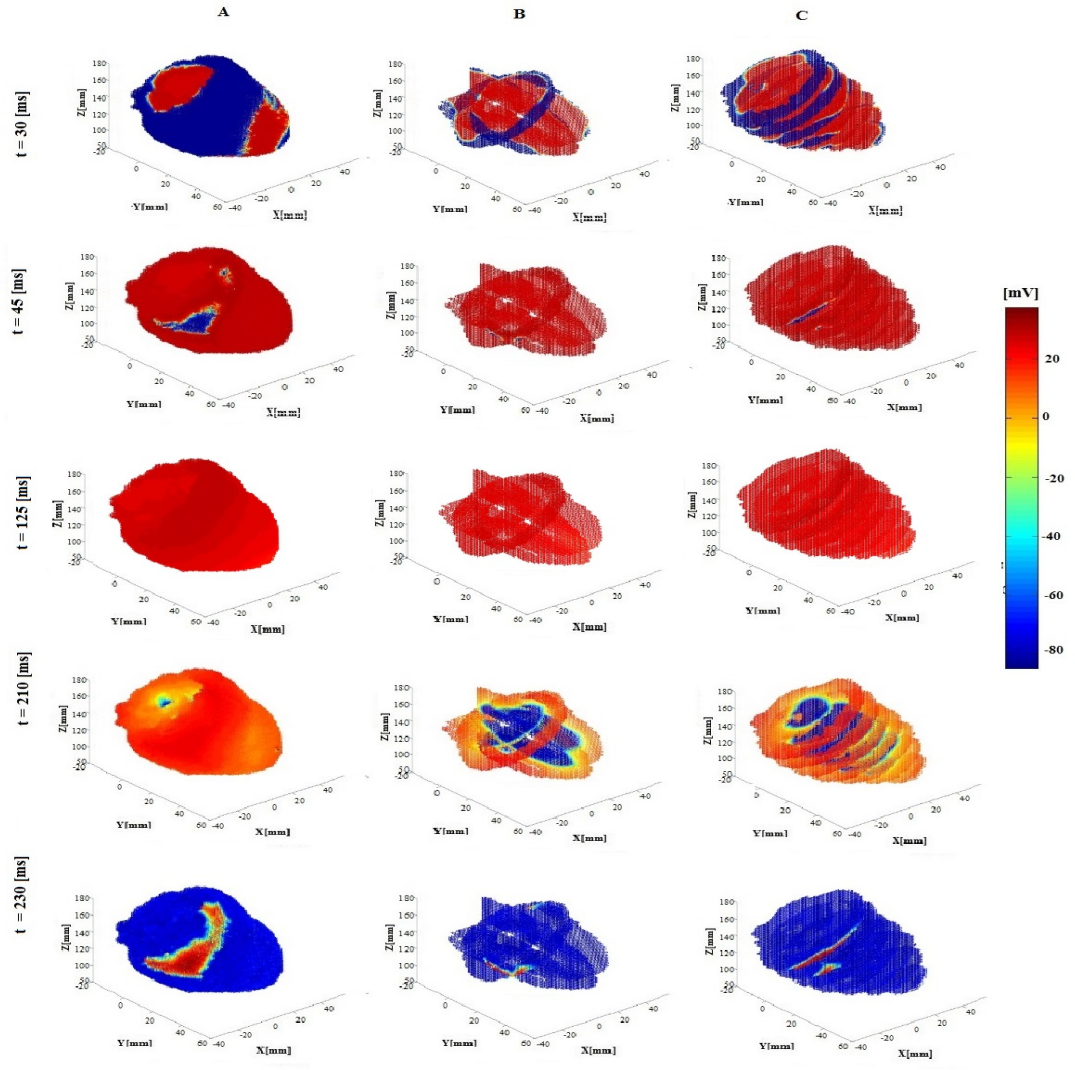

Figure 5.2: TMP distribution and propagation trough five time instants and from (A) tree dimensional (B) three cross-sectional plane, and (C) multiple x plane cross-sections.

5.3 Electrical Activity of Ventricular Tissue with Ectopic Heart Beats

In this section we present TMP distributions and propagation due to an ectopic arrhythmia. To do so, we stimulate the TMP distributions with an initial stimulation site at the apex region as shown in Figure 5.6. The defined stimulation site is an arbitrary initiation of ectopic heart beats similar to previous works [35], rather than having a biological accordance. Then, similar to previous sections, and using the same conductivity values and Aliev-Panfilov parameters same as in section 5.2, we model TMP distribution and propagation through the UHM.

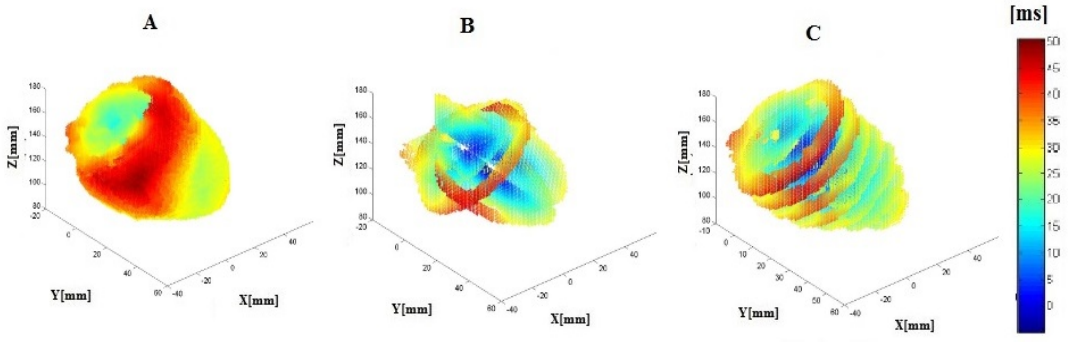

Figure 5.3: AT through (A) three dimensional (B) three cross-sectional plane, and (C) multiple X plane cross-sections.

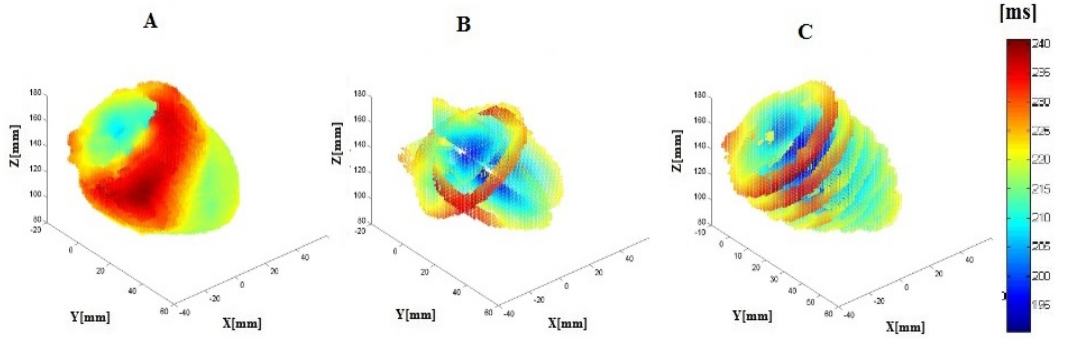

Figure 5.4: RT through (A) three dimensional (B) three cross-sectional plane, and (C) multiple X plane cross-sections.

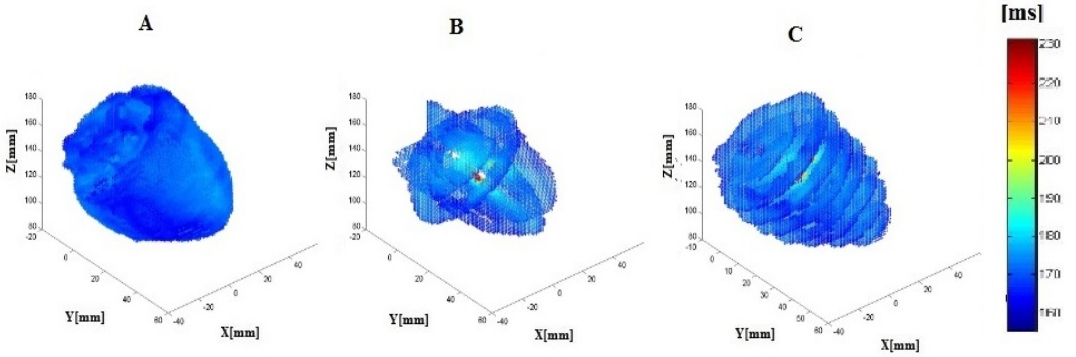

Figure 5.5: APD distribution through (A) three dimensional (B) three cross-sectional plane, and (C) multiple X plane cross-sections.

The Aliev-Panfilov parameters were adjusted such that the APs have a duration of almost 200 ms, amplitude of 125 mV, and the resting potential of -85 mV similar to section 5.2. The entire TMP propagation takes approximately 255 ms to span the entire ventricular volume. TMP wavefront distributions from three different viewpoints are shown in Figure 5.7, at five different time instants.

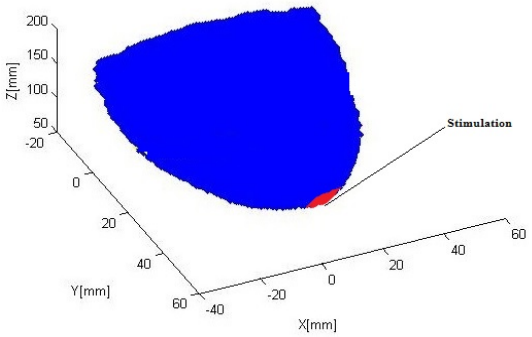

Figure 5.6: Initial stimulation of UHM with ectopic heart beats

As it can be seen from patterns in Figure 5.7, at time 30 ms, a wavefront representing depolarization of ventricular myocardium spans the ventricular tissue from the apex to the base. Next, at time 125 ms, almost all of the tissue has been depolarized, and is in plateau phase. The plateau phase of APs last until 210 ms. Then, at time 210 ms, repolarization starts to take place, and finally at time 245 ms, almost the entire ventricular volume has been repolarized. It is observed that the same AP characteristics (amplitude, resting potential and duration) are achieved at all locations, as expected from our simulation setup.

In Figure 5.8 , we can also see AT distribution through the entire ventricles volume. It can be seen that the early activation occurs at the apex subepicardial region, where initial stimulation site is located, and late activation at the base part of the heart model. It takes almost 65 ms to wavefront for activation of the entire volume. The same pattern of distribution can also be seen in the RT patterns shown in Figure 5.17. However, APD does not change so much through the entire geometry, and its values mostly change between 190 ms to 196 ms (Figure 5.10). The maximum values of APD can be seen at regions close to initial stimulation site just similar to previous sections [120, 129].

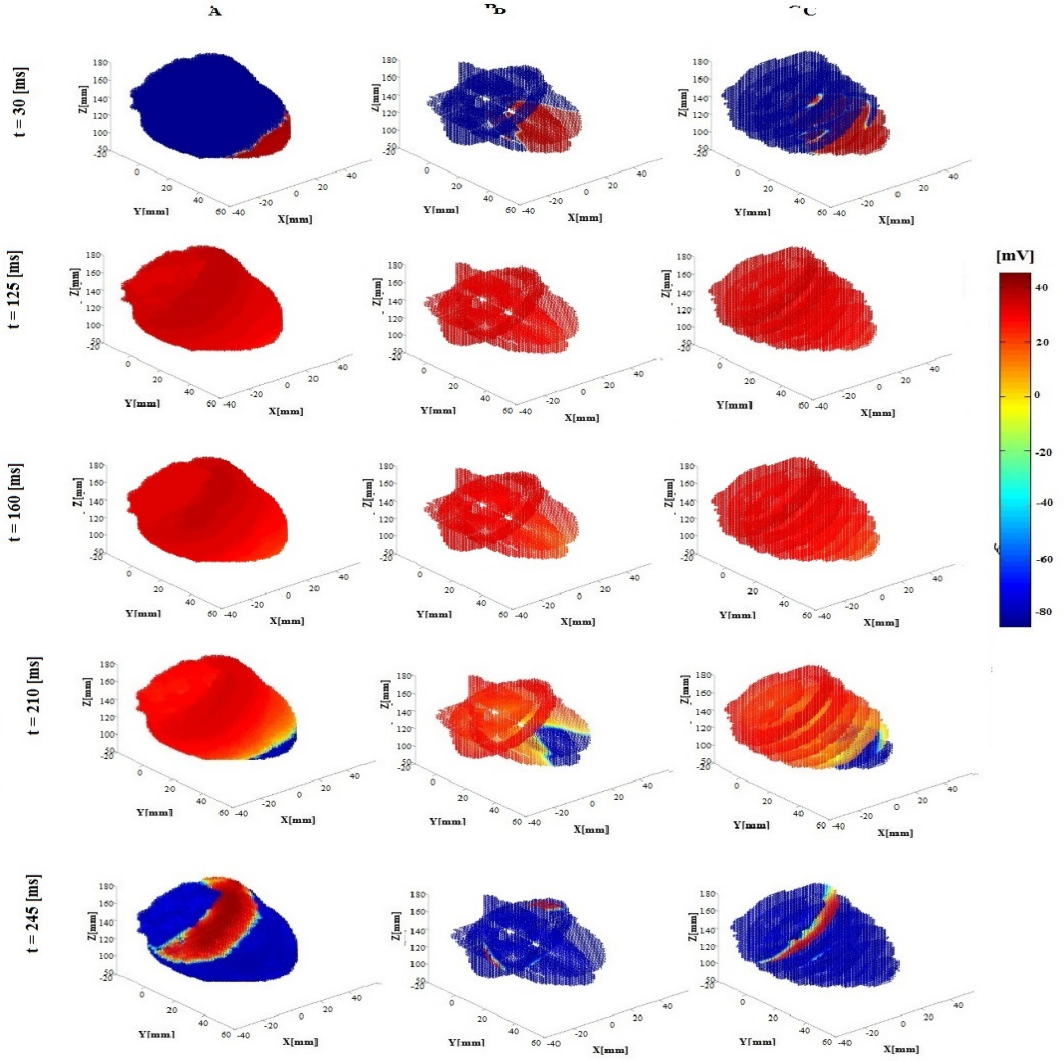

Figure 5.7: TMP distribution and propagation trough five time instants and from A) tree dimensional B) three cross-sectional planes, and C) multiple x plane cross-sections.

5.4 Electrical Activity In Partially Ischemic Tissue

According to experimental recordings and investigations [74, 104, 133, 134], during the first 12 min of ischemia, resting potential is elevated to $-60\ mV$ from its normal value of $-85\ mV$, action potential duration shortens by almost 50% and the amplitude decreases to $88mV$. In our simulations of TMP's in the ischemic tissue, we aimed to produce AP's similar to those experimental findings. We first introduced a region of ischemia within the ventricular geometry, as shown in Figure 5.11. Then, in order to match the experimental APs in the ischemic region,

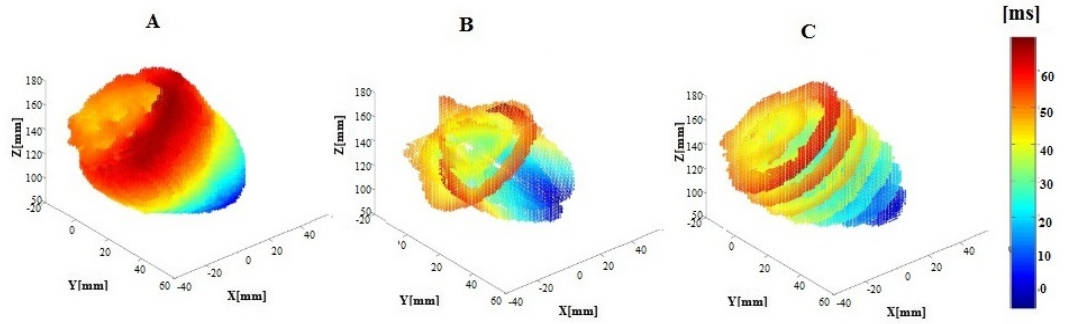

Figure 5.8: AT distribution through (A) three dimensional (B) three cross-sectional planes, and (C) multiple X plane cross-sections.

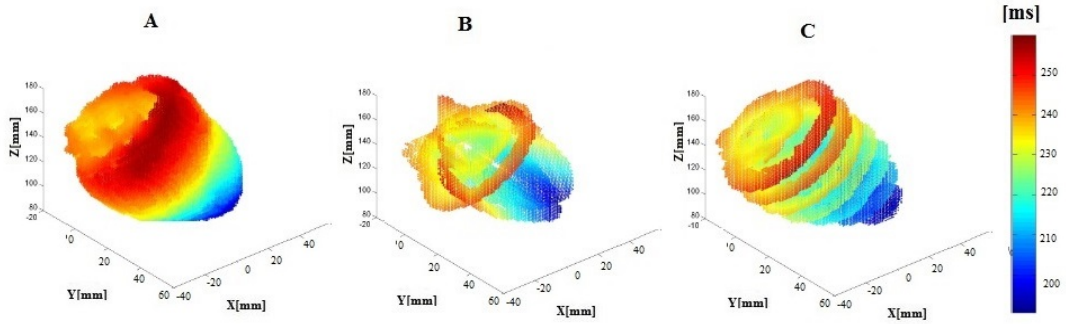

Figure 5.9: RT distribution through (A) three dimensional (B) three cross-sectional planes, and (C) multiple X plane cross-sections.

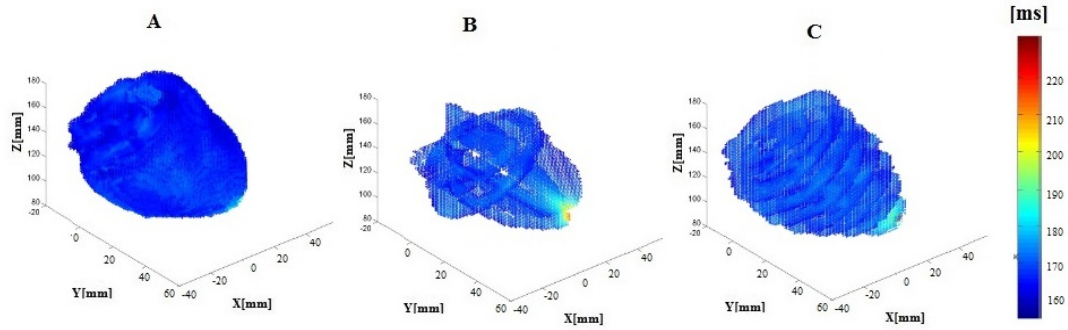

Figure 5.10: APD distribution through (A) three dimensional (B) three cross-sectional planes, and (C) multiple X plane cross-sections.

we first calculated new global conductivity tensor values for each point in the ischemic region. We used the same conductivity values as in section 5.2 for the healthy part of the ventricular tissue. We defined intracellular and extracellular local conductivity values of 0.16 S/m (longitudinal), 0.008S/m (transverse) and 0.08 S/m (longitudinal), 0.03 S/m (transverse), for the ischemic region of the ventricle, respectively. These values are assumed using a computational evaluation of the published conductivity values [118], and the relation between these values [119]. Then, using the new global conductivity values, we calculated new weight values for solving (3.11). Finally, using the ischemic weight values, and ischemic parameters (Table 5.2) in the ischemic regions and the normal weight values and parameters (Table 4.2) for the rest of the volume, we simulated TMP distributions and propagation over the ventricles. Initial stimulation was initiated from the apex region, same as in section 5.3.

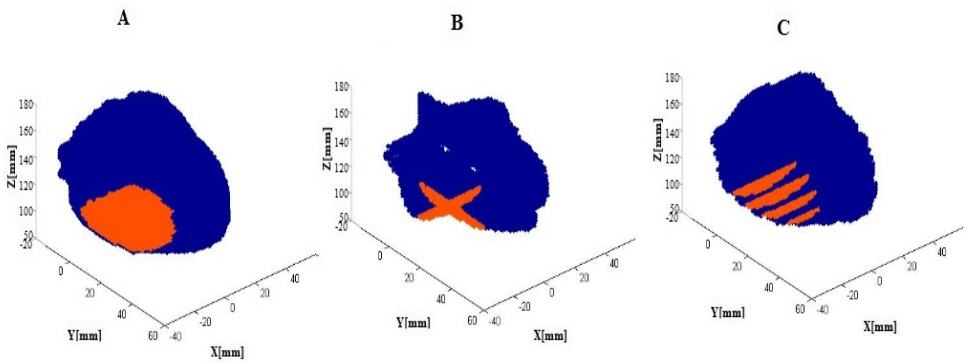

Figure 5.11: Ventricular tissue with partially ischemia (shown in red) from (A) tree dimensional B) three cross-sectional planes, and (C) multiple x plane cross-sections.

Table 5.2: Aliev-Panfilov parameters for ischemic region

Parameter	Values
α	0.017
k	0.6
μ_1	0.6
μ_2	0.7
ϵ_0	0.0158

The result of this simulation, which shows TMP distribution and wavefront propagation, are presented in Figure (5.12) from the same perspectives and at

the same sampled times as in Figure (5.7).

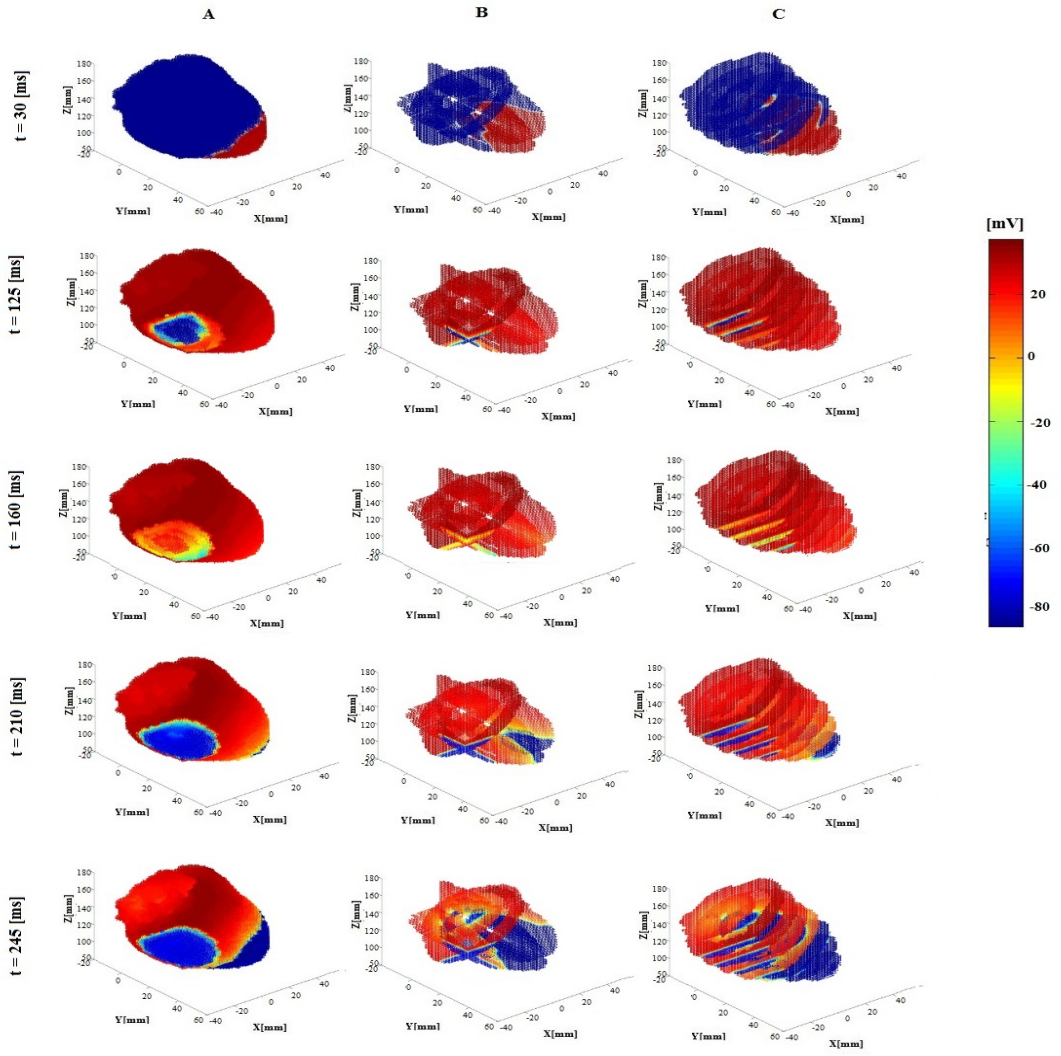

Figure 5.12: TMP distribution and propagation of partially ischemic tissue trough five time instants, and from (A) tree dimensional B) three cross-sectional planes, and (C) multiple x plane cross-sections.

Comparing Figure 5.12, and Figure 5.7, it can be seen that propagation of wavefront is much slower in partially ischemic tissue. It takes almost 308 ms for the TMP wavefront to span the entire tissue volume. Besides, at time 125 ms, late depolarization of ischemic region depicts delayed propagation in ischemic region, when the rest of the tissue is depolarized. At time 210 ms, not only propagation velocity, but also potential values are affected in the presence of ischemia; the maximum amplitude of the APs is less than the maximum amplitude of APs

in healthy regions. Finally, at time 245 ms, it can be seen that tissue in the ischemic region are repolarized faster, which can be a reason for decreasing of duration in ischemic region.

In Figure (5.13), we record the APs waveform at two different points for the normal heart simulation, and for the same points in the presence of ischemia. It can be seen that in the middle of the ischemic region, where ischemia is considered to be most severe, the AP duration has decreased from 200 ms to about 100 ms, the amplitude has decreased from 125 mV to about 88 mV and the resting potential increased from -85 mV to -60 mV. More importantly, an 8 ms delay occurred due to lower velocity of propagation in the ischemic region.

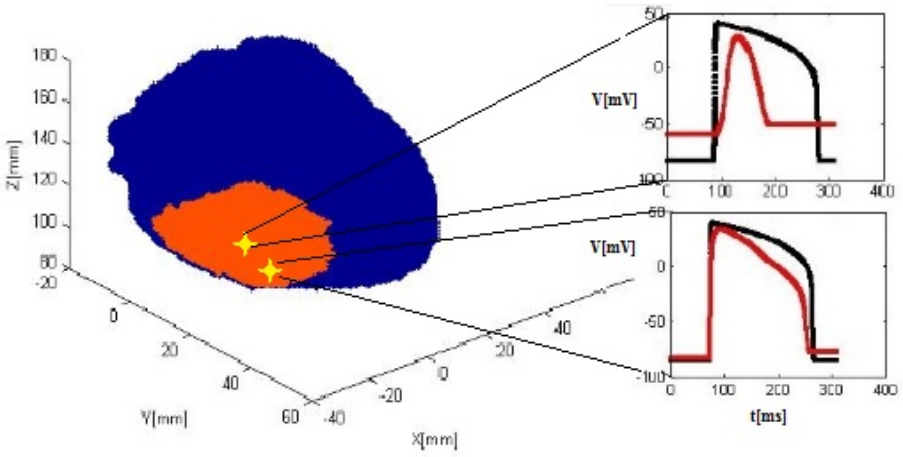

Figure 5.13: APs for two different points at normal tissue (black), and for the same points in presence of ischemia (red).

Figure 5.14, also shows the late activation at ischemic region, in particular in central part of it. However, as shown in Figure 5.15 it is the opposite in the RT, in which ischemic regions have the least RT. Finally, it can be seen in Figure 5.14, that APD has the smallest values in ischemic regions and change from almost 90 ms in the sever parts of ischemia (central part), to maximally 180 ms in the neighbourhood of healthy part of the tissue.

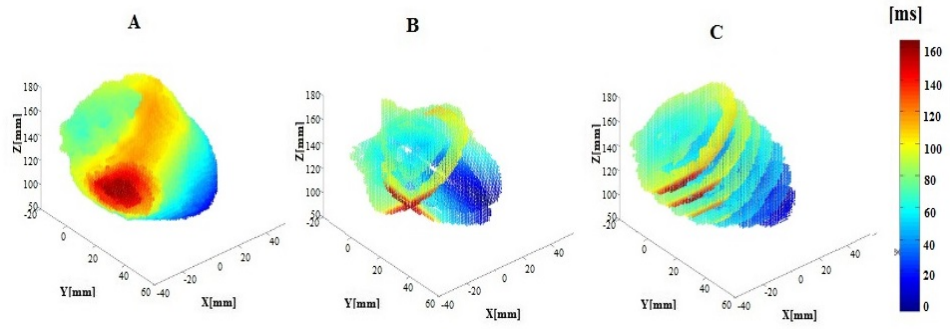

Figure 5.14: AT in ventricular tissue with partially ischemia from (A) tree dimensional B) three cross-sectional planes, and (C) multiple x plane cross-sections.

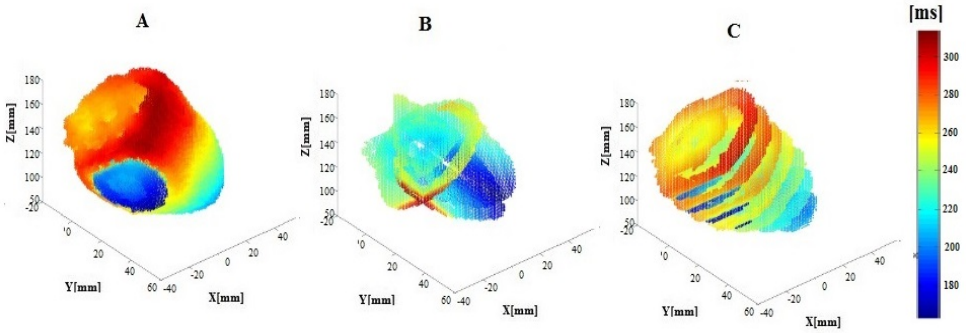

Figure 5.15: RT in ventricular tissue with partially ischemia from (A) tree dimensional B) three cross-sectional planes, and (C) multiple x plane cross-sections.

5.5 Wolf-Parkinson-White Syndrome

According to explanation in section 2.4.5, Wolf Parkinson White (WPW) syndrome is a disorder of electrical conductance of cardiac tissue, in which an abnormal conduction pathway between atria and ventricles cause preexcitaion of the cardiac tissue. In order to model WPW syndrome, we should stimulate tissue from an abnormal conduction pathway in addition to normal excitation pathways. So, we first initiate the stimulation from the lateral part of left ventricular subendocardial wall, which is shown in Figure 5.17, 40 ms before initiation of normal excitation of tissue. This stimulation site is chosen similar to previous studies [78, 88]. Next, at times $40ms$, $45ms$, and $55ms$ we again initiate exci-

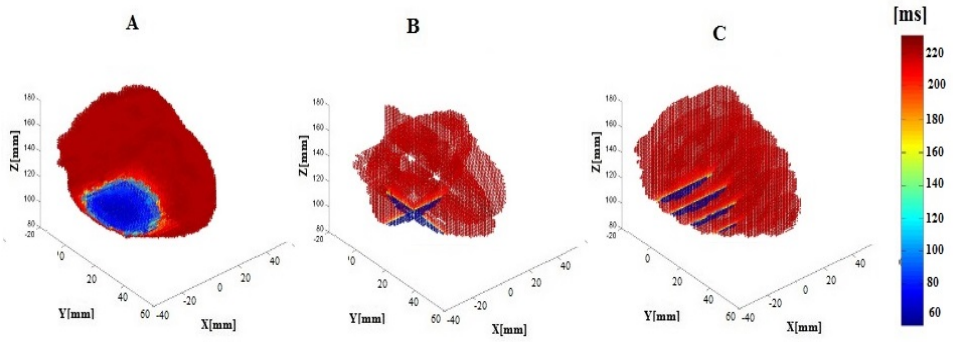

Figure 5.16: APD in ventricular tissue with partially ischemia from (A) tree dimensional B) three cross-sectional planes, and (C) multiple x plane cross-sections.

tation similar to section 5.2. Finally, using the simulation method (explained in chapter 3) we simulate TMP wavefront distribution and propagation through UHM with WPW syndrome.

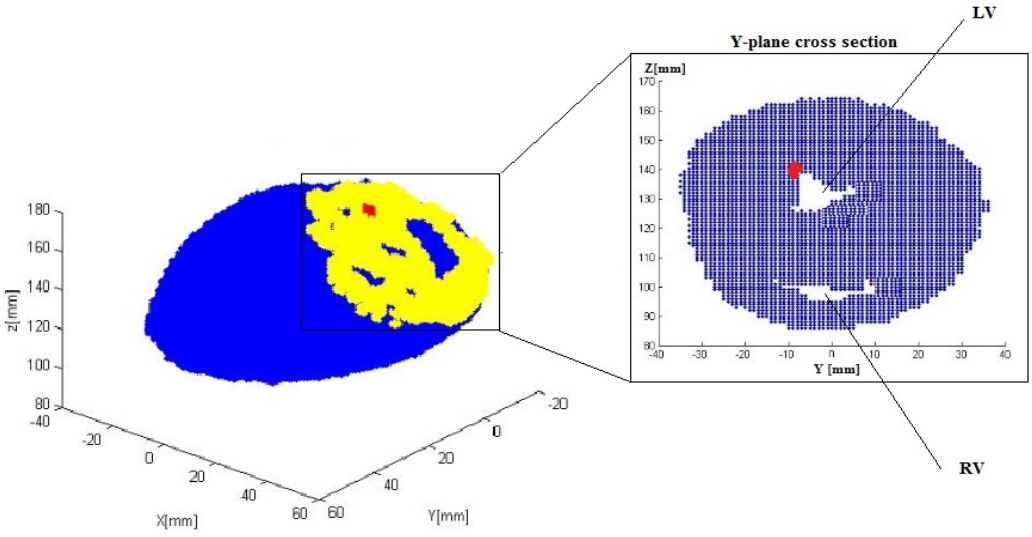

Figure 5.17: Initial stimulation in a ventricular tissue with WPW syndrome

Figure 5.18, TMP distributions at five time instants and from different views are shown. We can see that at time 15 ms, stimulation starts from the lateral part of left ventricle, and at time 40 ms, almost all sites, used for normal excitation of the heart (shown in Figure 5.1) are already depolarized. This can be due

to rapid conduction through abnormal conduction pathway in comparison with normal conduction pathway, in which signal has a delay before conducting to bundle of His and lead to high cardiac beats rate. The plateau phase of tissue continues until 210ms. It can be seen that repolarization starts from the lateral endocardial wall of left ventricular, and at time 240 ms, almost the entire cardiac tissue is repolarized. The entire propagation takes almost 240 ms, a little more than the propagation of a normal heart beat.

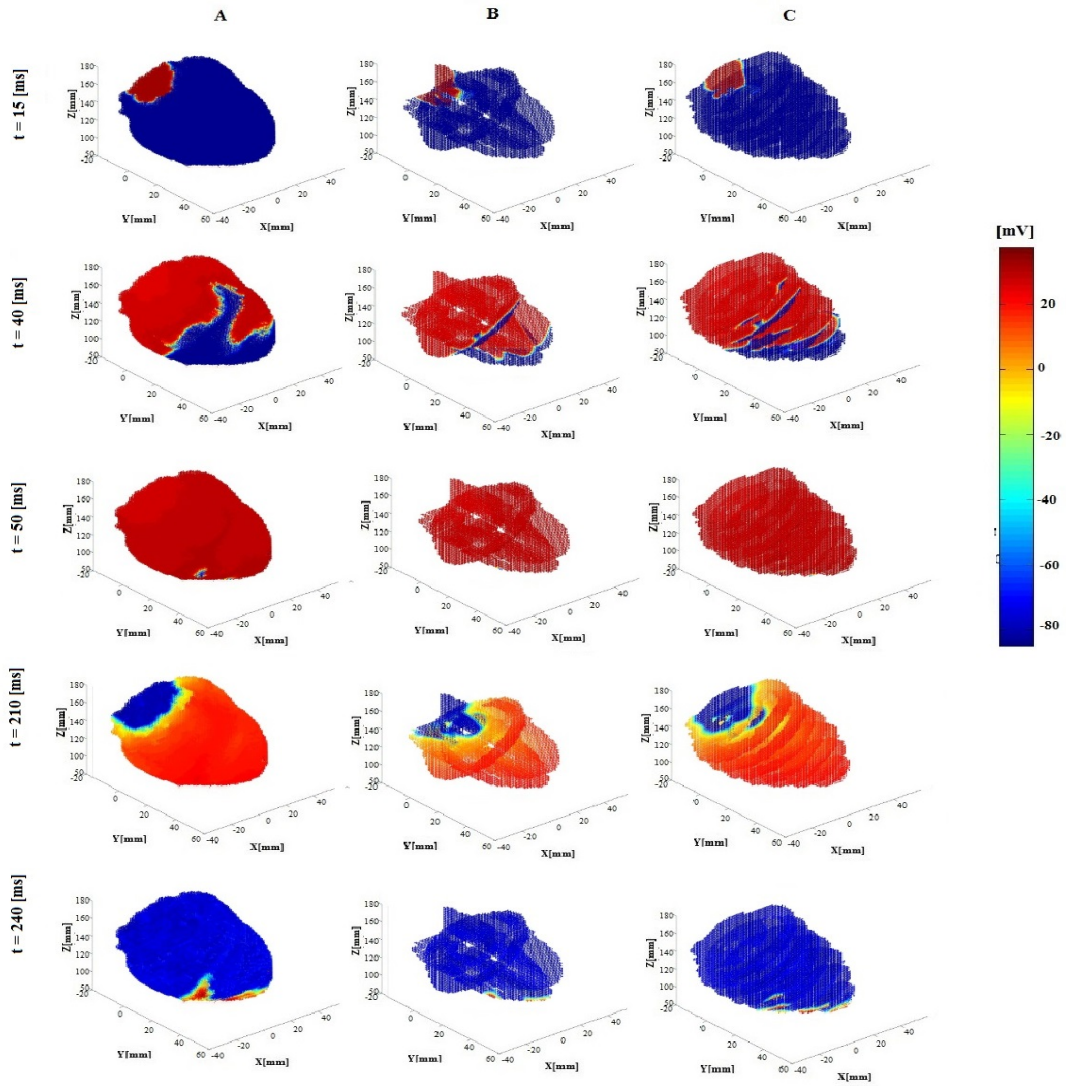

Figure 5.18: TMP distribution and propagation trough five time instant and from (A) tree dimensional B) three cross-sectional planes, and (C) multiple x plane cross-sections.

In Figure 5.21, it can be seen that early activation starts from abnormal conduc-

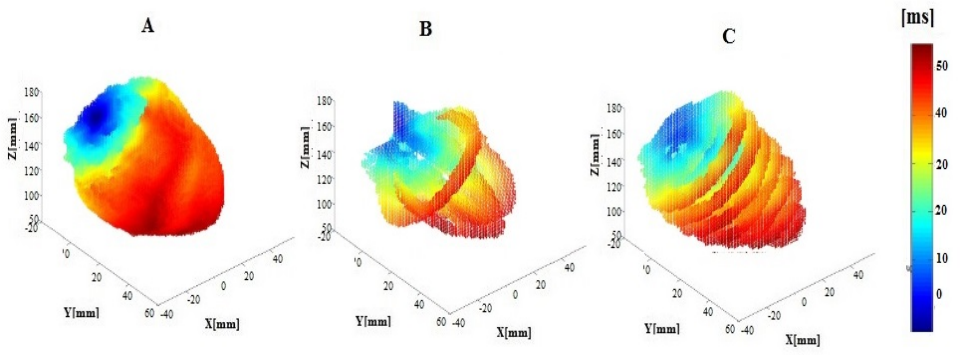

Figure 5.19: AT distribution from (A) tree dimensional B) three cross-sectional planes, and (C) multiple x plane cross-sections.

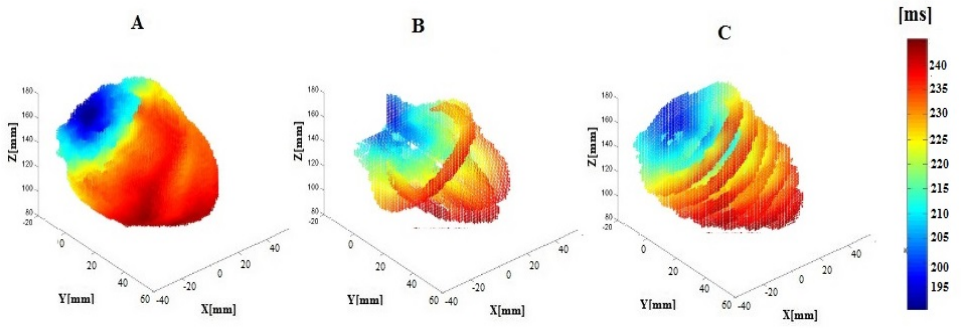

Figure 5.20: RT distribution from (A) tree dimensional B) three cross-sectional planes, and (C) multiple x plane cross-sections.

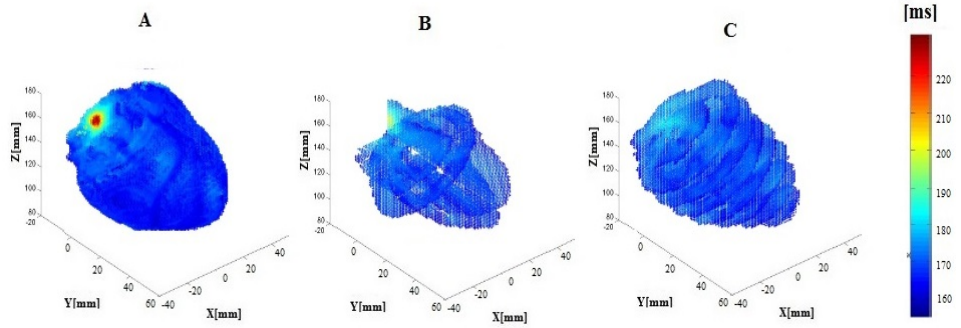

Figure 5.21: APD distribution from (A) tree dimensional B) three cross-sectional planes, and (C) multiple x plane cross-sections.

tion pathway and late activation occurs at the apex region regardless to normal conduction pathway. Similarly, RT follows the same alteration patterns as the AT.

5.6 Discussion

In this study, using simplified Aliev-Panfilov cardiac model, we simulated the electrical activity in different functional states of cardiac tissue. We started from segmented MR images, and readily available fiber orientations from DW images taken from the SCI Institute datasets. In this chapter, we mostly characterized TMP propagation, and propagation qualitatively, rather than quantitatively. Simulation results were successful to mimic different functional state of cardiac tissue. However, the entire activation of cardiac tissue was calculated 50 ms to 65 ms, which is lower than its normal value between 70 ms to 100 ms. This alteration is mostly due to contributing of new conductivity values. These values are chosen according to computational evaluation of conductivity values similar to previous works [118, 119], which enable us to find conductivity values in ischemic regions.

CHAPTER 6

CONCLUSION

In this thesis work, using simplified Aliev-Panfilov model we simulated electrical activity of the heart. The study based on two major parts: (1) investigation on anisotropic nature of cardiac tissue, in which we examined isotropic assumption of cardiac tissue, and one step further, we examined amount of fiber orientation effects on outputs from simulation of electrical activity in cardiac tissue. We also, suggested a new practical, easy, and accurate model for estimation of electrical activity without information about its fiber orientation. (2) modelling different functional states of the heart using the UHM, in which geometry, and fiber informations are obtained using MRI, and DTI techniques. These normal and abnormal functional states are namely: heart with normal heart beats, heart with ectopic beats, tissue with partially ischemia, and cardiac tissue with WPW syndrome.

6.1 Anisotropic nature of cardiac tissue

As shown in chapter 4, anisotropic nature has significant effect on TMP features. Above all, we compared anisotropic results with outcomes from isotropic assumption of conductivity values. It was shown that using isotropic assumption:

• Can not estimate TMP in general due to low correlation and high error values.

•Can estimate AP morphology with acceptable correlation.

• Can have a reasonable estimation about AT, and RT alteration patterns, but can not estimate the exact AT, and RT.

• Can not give any information related to TMP propagation velocity.

Considering these inferences, we can conclude that isotropic assumption can not be substituted with anisotropic nature of cardiac electrical conductivity. Accordingly, we also investigated amount of fiber orientation effects on anisotropy property of cardiac tissue, by addition of different noise values to fiber direction information. The inference were:

• Effects of different fiber variances on TMP distribution patterns, TMP propagation, and AP features are insignificant.

• APD alteration pattern is more vulnerable to fiber variances in comparison to AT and RT pattern alterations.

It can be concluded that effect of fiber variance is much less than isotropic assumption of cardiac conductivities. This also shows minority effects of geometry errors originated from different data acquisition techniques like DTI. These results also led us to propose a new technique to estimate electrical activity of a heart using fiber information of another cognate heart. The inference from this study were:

• The model was successful in modelling TMP values, AP shape, AT, and RT alteration patterns.

• It was not successful in estimation of APD duration patterns, but not worse than isotropic assumption of cardiac tissue.

• However, the magnitude of APD was closer to real APD values with low error value between them.

6.2 Modelling different functional states of cardiac tissue

In this study, using simplified Aliev-Panfilov cardiac model, we simulated the electrical activity in a dog heart geometry. The model although has not physiological meaning, it simulates the overall phenomena adequately and with lower complexity at tissue level and can be used as prediction, diagnostic and treatment tracking tool of heart pathologies. We have carried out our simulations for various cases; normal cardiac tissue with normal and ectopic beats, cardiac tissue with partially ischemia and WPW syndrome. We also applied segmented MR images, and readily available fiber orientations from DW images taken from the SCI Institute datasets. Use of MR-DTI based models has advantage to develop our model specific for patients. This advantages can lead us to characterize, predict, and estimate development of different cardiac diseases specific for patients, using detailed information such as conductivity values, fiber orientation, and cardiac geometry obtained throgh MR-DTI techniques.

We used Aliev-Panfilov model for simulating of whole cardiac tissue. This model represents information about TMP wavefront at tissue level, but does not reveal any information at cellular level. Moreover, the model and its parameters does not carry any physiological meaning. In other word, we set the parameters ourselves to simulate AP similar to experimental APs. As setting of these parameters cannot be ideal to mimic the exact APs on cardiac tissue, the model always has an internal error related to parameters setting.

6.3 Future Works

As future research, we can construct the results of simulations, by contributing error values obtained through investigating of anisotropic feature of cardiac tissue. Furthermore, in this study we investigated micro-structural alteration effects on electrical activity of cardiac tissue, contributing different variance values. Accordingly, using fiber information obtained using two methods: (1) experimentally and by histologically sectioning of cardiac tissue, (2) MR-DTI

techniques, we can calculate a real variance between realistic fiber orientations, and DTI based fiber orientations. Then using methods explained in chapter 4, we would be able to calculate amount of error originated during DTI data acqusition technique. In addition, we can also investigate effect of macro-structural effects on electrical activity of cardiac tissue. Doing so, we investigate role of cardiac size on different features of APs. Moreover, it was shown that registeration method was successful in estimating of electrical activity of dog's heart. In future by developing the method to human's heart models, we would be able to estimate electrical activity of human's cardiac tissue without its fiber orientation information.

In this preliminary work, we can obtain the TMP distributions starting from segmented MR images and the corresponding fiber structure from DW images. In our future work, in order to simulate subject-specific TMP distributions, we will start from the actual medical images and incorporate segmentation as the first step of this work. Another handicap of our study is that in these simulations, we assigned the ischemic region, and ischemic conductivity values ourselves. However, ischemia does not develop similarly among different patients due to their heart geometry and pathology variations. Another step in our future studies is to determine the region and severity of ischemia also from medical images and obtain more realistic, subject specific ischemic models. Finally, since several interferences such as motion artefacts, image artefacts, and MRI artifact affects results from DTI technique. Thus, we need to rely on generic fiber orientations in our studies, which will introduce errors in our models. The nature of this error should also be a topic for future studies.

REFERENCES

[1] Cardiac anatomy, http://www.biosbcc.net/b100cardio/htm/heartant.htm, last visit on 10.02.2015.

[2] Scirun software, www.sci.utah.edu, last visit on 01.02.2015.

[3] World health organization, www.who.int, last visited on 20.01.2015.

[4] D. R. Adam. Propagation of depolarization and repolarization processes in the myocardium-an anisotropic model. *Biomedical Engineering, IEEE Transactions on*, 38(2):133–141, 1991.

[5] A. Adamatzky and O. Holland. Phenomenology of excitation in 2-d cellular automata and swarm systems. *Chaos, Solitons & Fractals*, 9(7):1233–1265, 1998.

[6] R. R. Aliev and A. V. Panfilov. A simple two-variable model of cardiac excitation. *Chaos, Solitons & Fractals*, 7(3):293–301, 1996.

[7] H. Arevalo, M. Bishop, B. Rodriguez, and N. Trayanova. Photon scattering during optical mapping distorts the spatiotemporal organization in vf. *Heart Rhythm*, 5:S359, 2008.

[8] H. Arevalo, P. Helm, and N. Trayanova. Development of a model of the infarcted canine heart that predicts arrhythmia generation from specific cardiac geometry and scar distribution. In *Computers in Cardiology, 2008*, pages 497–500. IEEE, 2008.

[9] H. Arevalo, G. Plank, P. Helm, H. Halperin, and N. Trayanova. Volume of peri-infarct zone determines arrhythmogenesis in infarcted heart. *Heart Rhythm*, 6(5):S232–S233, 2009.

[10] H. Arevalo, F. Vadakkumpadan, and N. Trayanova. Fiber architecture in infarcted hearts does not significantly affect location of reentry isthmus or optimal ablation site. *Heart Rhythm*, 7:S163, 2010.

[11] T. Arts, R. S. Reneman, and P. C. Veenstra. A model of the mechanics of the left ventricle. *Annals of biomedical engineering*, 7(3-4):299–318, 1979.

[12] T. Ashihara, J. Constantino, and N. A. Trayanova. Tunnel propagation of postshock activations as a hypothesis for fibrillation induction and isoelectric window. *Circulation research*, 102(6):737–745, 2008.

[13] P. Bagnoli, N. Malagutti, D. Gastaldi, E. Marcelli, E. Lui, L. Cercenelli, M. L. Costantino, G. Plicchi, and R. Fumero. Computational finite element model of cardiac torsion. *The International journal of artificial organs*, 34(1):44–53, 2011.

[14] D. L. Beaudoin and B. J. Roth. Small random fiber angle variations as a mechanism for far-field stimulation of cardiac tissue. In *Engineering in Medicine and Biology Society, 2004. IEMBS'04. 26th Annual International Conference of the IEEE*, volume 2, pages 3975–3978. IEEE, 2004.

[15] D. L. Beaudoin and B. J. Roth. Small random fiber angle variations as a mechanism for far-field stimulation of cardiac tissue. In *Engineering in Medicine and Biology Society, 2004. IEMBS'04. 26th Annual International Conference of the IEEE*, volume 2, pages 3975–3978. IEEE, 2004.

[16] G. W. Beeler and H. Reuter. Reconstruction of the action potential of ventricular myocardial fibres. *The Journal of physiology*, 268(1):177–210, 1977.

[17] Y. Belhamadia, A. Fortin, and Y. Bourgault. Towards accurate numerical method for monodomain models using a realistic heart geometry. *Mathematical Biosciences*, 220(2):89–101, 2009.

[18] O. Berenfeld and J. Jalife. Purkinje-muscle reentry as a mechanism of polymorphic ventricular arrhythmias in a 3-dimensional model of the ventricles. *Circulation Research*, 82(10):1063–1077, 1998.

[19] O. Bernus, B. Van Eyck, H. Verschelde, and A. Panfilov. Transition from ventricular fibrillation to ventricular tachycardia: a simulation study on the role of ca2+-channel blockers in human ventricular tissue. *Physics in medicine and biology*, 47(23):4167, 2002.

[20] O. Bernus, R. Wilders, C. W. Zemlin, H. Verschelde, and A. V. Panfilov. A computationally efficient electrophysiological model of human ventricular cells. *American Journal of Physiology-Heart and Circulatory Physiology*, 282(6):H2296–H2308, 2002.

[21] P. J. Besl and N. D. McKay. Method for registration of 3-d shapes. In *Robotics-DL tentative*, pages 586–606. International Society for Optics and Photonics, 1992.

[22] M. J. Bishop, D. J. Gavaghan, N. A. Trayanova, and B. Rodriguez. Photon scattering effects in optical mapping of propagation and arrhythmogenesis in the heart. *Journal of electrocardiology*, 40(6):S75–S80, 2007.

[23] M. J. Bishop, G. Plank, R. A. Burton, J. E. Schneider, D. J. Gavaghan, V. Grau, and P. Kohl. Development of an anatomically detailed mri-

derived rabbit ventricular model and assessment of its impact on simulations of electrophysiological function. *American Journal of Physiology-Heart and Circulatory Physiology*, 298(2):H699–H718, 2010.

[24] M. J. Bishop, B. Rodriguez, J. Eason, J. P. Whiteley, N. Trayanova, and D. J. Gavaghan. Synthesis of voltage-sensitive optical signals: application to panoramic optical mapping. *Biophysical journal*, 90(8):2938–2945, 2006.

[25] M. J. Bishop, B. Rodriguez, F. Qu, I. R. Efimov, D. J. Gavaghan, and N. A. Trayanova. The role of photon scattering in optical signal distortion during arrhythmia and defibrillation. *Biophysical journal*, 93(10):3714–3726, 2007.

[26] M. Boulakia, S. Cazeau, M. A. Fernández, J.-F. Gerbeau, and N. Zemzemi. Mathematical modeling of electrocardiograms: a numerical study. *Annals of biomedical engineering*, 38(3):1071–1097, 2010.

[27] P. Bovendeerd, T. Arts, J. Huyghe, D. Van Campen, and R. Reneman. Dependence of local left ventricular wall mechanics on myocardial fiber orientation: a model study. *Journal of biomechanics*, 25(10):1129–1140, 1992.

[28] P. M. Boyle, M. Deo, G. Plank, and E. J. Vigmond. Purkinje-mediated effects in the response of quiescent ventricles to defibrillation shocks. *Annals of biomedical engineering*, 38(2):456–468, 2010.

[29] H. E. Cetingul, G. Plank, N. Trayanova, and R. Vidal. Estimation of multimodal orientation distribution functions from cardiac mri for tracking purkinje fibers through branchings. In *Biomedical Imaging: From Nano to Macro, 2009. ISBI'09. IEEE International Symposium on*, pages 839–842. IEEE, 2009.

[30] A. K. Cheung, M. J. Sarnak, G. Yan, M. Berkoben, R. Heyka, A. Kaufman, J. Lewis, M. Rocco, R. Toto, D. Windus, et al. Cardiac diseases in maintenance hemodialysis patients: results of the hemo study. *Kidney international*, 65(6):2380–2389, 2004.

[31] R. H. Clayton. Computational models of normal and abnormal action potential propagation in cardiac tissue: linking experimental and clinical cardiology. *Physiological measurement*, 22(3):R15, 2001.

[32] P. Colli Franzone, L. Guerri, M. Pennacchio, and B. Taccardi. Spread of excitation in 3-d models of the anisotropic cardiac tissue. iii. effects of ventricular geometry and fiber structure on the potential distribution. *Mathematical biosciences*, 151(1):51–98, 1998.

[33] P. Colli Franzone, L. Pavarino, S. Scacchi, and B. Taccardi. Modeling ventricular repolarization: effects of transmural and apex-to-base heterogeneities in action potential durations. *Mathematical biosciences*, 214(1):140–152, 2008.

[34] P. Colli Franzone, L. Pavarino, and B. Taccardi. Simulating patterns of excitation, repolarization and action potential duration with cardiac bidomain and monodomain models. *Mathematical biosciences*, 197(1):35–66, 2005.

[35] U. Cunedioglu and B. Yilmaz. Combination of computer simulations and experimental measurements as the training dataset for statistical estimation of epicardial activation maps from venous catheter recordings. *Biomedical Engineering, IEEE Transactions on*, 56(3):837–845, 2009.

[36] S. S. Demir, B. O'Rourke, G. F. Tomaselli, E. Marban, and R. L. Winslow. Action potential variation in canine ventricle: a modeling study. In *Computers in Cardiology, 1996*, pages 221–224. IEEE, 1996.

[37] M. Deo, P. Boyle, G. Plank, and E. Vigmond. Arrhythmogenic mechanisms of the purkinje system during electric shocks: a modeling study. *Heart rhythm*, 6(12):1782–1789, 2009.

[38] A. Despopoulos and S. Silbernagl. *Color atlas of physiology*. Thieme, 2003.

[39] P. Deuflhard, B. Erdmann, R. Roitzsch, and G. T. Lines. Adaptive finite element simulation of ventricular fibrillation dynamics. *Computing and visualization in science*, 12(5):201–205, 2009.

[40] J.-P. Drouhard and F. A. Roberge. Revised formulation of the hodgkin-huxley representation of the sodium current in cardiac cells. *Computers and Biomedical Research*, 20(4):333–350, 1987.

[41] D. Durrer, R. T. Van Dam, G. Freud, M. Janse, F. Meijler, and R. Arzbaecher. Total excitation of the isolated human heart. *Circulation*, 41(6):899–912, 1970.

[42] L. Ebihara and E. Johnson. Fast sodium current in cardiac muscle. a quantitative description. *Biophysical Journal*, 32(2):779–790, 1980.

[43] B. Echebarria and A. Karma. Mechanisms for initiation of cardiac discordant alternans. *The European Physical Journal-Special Topics*, 146(1):217–231, 2007.

[44] G. M. Faber and Y. Rudy. Action potential and contractility changes in [na< sup>+</sup>]< sub> i</sub> overloaded cardiac myocytes: A simulation study. *Biophysical Journal*, 78(5):2392–2404, 2000.

[45] F. Fenton and A. Karma. Vortex dynamics in three-dimensional continuous myocardium with fiber rotation: filament instability and fibrillation. *Chaos: An Interdisciplinary Journal of Nonlinear Science*, 8(1):20–47, 1998.

[46] G. Fischer, B. Tilg, R. Modre, G. Huiskamp, J. Fetzer, W. Rucker, and P. Wach. A bidomain model based bem-fem coupling formulation for anisotropic cardiac tissue. *Annals of Biomedical Engineering*, 28(10):1229–1243, 2000.

[47] R. FitzHugh. Impulses and physiological states in theoretical models of nerve membrane. *Biophysical journal*, 1(6):445–466, 1961.

[48] P. C. Franzone and L. Guerri. Spreading of excitation in 3-d models of the anisotropic cardiac tissue. i. validation of the eikonal model. *Mathematical biosciences*, 113(2):145–209, 1993.

[49] P. C. Franzone, L. Guerri, and S. Rovida. Wavefront propagation in an activation model of the anisotropic cardiac tissue: asymptotic analysis and numerical simulations. *Journal of mathematical biology*, 28(2):121–176, 1990.

[50] P. C. Franzone, L. GUERRI, and B. TACCARDI. Potential distributions generated by point stimulation in a myocardial volume. *Journal of cardiovascular electrophysiology*, 4(4):438–458, 1993.

[51] J. Freudenberg, T. Schiemann, U. Tiede, and K. H. Höhne. Simulation of cardiac excitation patterns in a three-dimensional anatomical heart atlas. *Computers in biology and medicine*, 30(4):191–205, 2000.

[52] C. Frindel, M. Robini, P. Croisille, and Y.-M. Zhu. Comparison of regularization methods for human cardiac diffusion tensor mri. *Medical Image Analysis*, 13(3):405–418, 2009.

[53] L. Geddes and L. Baker. The specific resistance of biological material—a compendium of data for the biomedical engineer and physiologist. *Medical and biological engineering*, 5(3):271–293, 1967.

[54] P. B. Gharpure, C. R. Johnson, and N. Harrison. A cellular automaton model of electrical activation in canine ventricles: A validation study. *Annals of Biomed. Eng*, 1995.

[55] S. Ghosh and Y. Rudy. Application of l1-norm regularization to epicardial potential solution of the inverse electrocardiography problem. *Annals of biomedical engineering*, 37(5):902–912, 2009.

[56] R. Glauber, W. Brittin, et al. Lectures in theoretical physics, 1959.

[57] R. Gray and J. Jalife. Ventricular fibrillation and atrial fibrillation are two different beasts. *Chaos: An Interdisciplinary Journal of Nonlinear Science*, 8(1):65–78, 1998.

[58] R. M. Gulrajani. Bioelectricity and biomagnetism. 1998.

[59] V. Gurev, T. Lee, J. Constantino, H. Arevalo, and N. A. Trayanova. Models of cardiac electromechanics based on individual hearts imaging data. *Biomechanics and modeling in mechanobiology*, 10(3):295–306, 2011.

[60] J. E. Hall. *Guyton and Hall Textbook of Medical Physiology: Enhanced E-book*. Elsevier Health Sciences, 2010.

[61] A. L. Hodgkin and A. F. Huxley. Action potentials recorded from inside a nerve fibre. *Nature*, 144(3651):710–711, 1939.

[62] A. L. Hodgkin and A. F. Huxley. A quantitative description of membrane current and its application to conduction and excitation in nerve. *The Journal of physiology*, 117(4):500, 1952.

[63] R. Hren, X. Zhang, and G. Stroink. Comparison between electrocardiographic and magnetocardiographic inverse solutions using the boundary element method. *Medical and Biological Engineering and Computing*, 34(2):110–114, 1996.

[64] P. Hunter, P. McNaughton, and D. Noble. Analytical models of propagation in excitable cells. *Progress in biophysics and molecular biology*, 30:99–144, 1976.

[65] M. S. Jafri, J. J. Rice, and R. L. Winslow. Cardiac ca< sup> 2+</sup> dynamics: The roles of ryanodine receptor adaptation and sarcoplasmic reticulum load. *Biophysical Journal*, 74(3):1149–1168, 1998.

[66] X. Jie and N. A. Trayanova. Mechanisms for initiation of reentry in acute regional ischemia phase 1b. *Heart Rhythm*, 7(3):379–386, 2010.

[67] S. A. Jones. *ECG notes: Interpretation and management guide*. FA Davis, 2009.

[68] K. R. Jun, Y. R. Seong, and T. G. Kim. A cellular automata model of activation process in ventricular muscle. In *SCSC*, volume 94, pages 769–774, 1994.

[69] C. Kähler, E. Schleussner, U. Schneider, and H.-J. Seewald. Prenatal diagnosis of the wolf-parkinson-white-syndrome by fetal magnetocardiography. *BJOG: An International Journal of Obstetrics & Gynaecology*, 108(3):335–336, 2001.

[70] J. P. Keener and J. Sneyd. *Mathematical physiology*, volume 8. Springer, 1998.

[71] R. H. Keldermann, K. H. Ten Tusscher, M. P. Nash, C. P. Bradley, R. Hren, P. Taggart, and A. V. Panfilov. A computational study of mother rotor vf in the human ventricles. *American Journal of Physiology-Heart and Circulatory Physiology*, 296(2):H370–H379, 2009.

[72] R. H. Keldermann, K. H. ten Tusscher, M. P. Nash, R. Hren, P. Taggart, and A. V. Panfilov. Effect of heterogeneous apd restitution on vf organization in a model of the human ventricles. *American Journal of Physiology-Heart and Circulatory Physiology*, 294(2):H764–H774, 2008.

[73] R. Klabunde. *Cardiovascular physiology concepts*. Lippincott Williams & Wilkins, 2011.

[74] A. G. Kléber, C. B. Riegger, and M. J. Janse. Extracellular k< sup>+</sup> and h< sup>+</sup> shifts in early ischemia: Mechanisms and relation to changes in impulse propagation. *Journal of molecular and cellular cardiology*, 19:35–44, 1987.

[75] R. O. Kuenzler, R. S. MacLeod, B. Taccardi, Q. Ni, and R. L. Lux. Estimation of epicardial activation maps from intravascular recordings. *Journal of electrocardiology*, 32(2):77–92, 1999.

[76] I. LeGrice, P. Hunter, and B. Smaill. Laminar structure of the heart: a mathematical model. *American Journal of Physiology*, 272:H2466–H2476, 1997.

[77] C. Lin and L. A. Segel. *Mathematics Applied to Deterministic Problems*. SIAM, 1974.

[78] M. Lorange and R. M. Gulrajani. Computer simulation of the wolff-parkinson-white preexcitation syndrome with a modified miller-geselowitz heart model. *Biomedical Engineering, IEEE Transactions on*, (9):862–873, 1986.

[79] M. Lorange, R. M. Gulrajani, R. A. Nadeau, and I. Préda. A computer heart model incorporating anisotropic propagation: Ii. simulations of conduction block. *Journal of electrocardiology*, 26(4):263–277, 1993.

[80] C.-h. Luo and Y. Rudy. A model of the ventricular cardiac action potential. depolarization, repolarization, and their interaction. *Circulation research*, 68(6):1501–1526, 1991.

[81] C.-h. Luo and Y. Rudy. A dynamic model of the cardiac ventricular action potential. i. simulations of ionic currents and concentration changes. *Circulation research*, 74(6):1071–1096, 1994.

[82] C.-H. Luo and Y. Rudy. A dynamic model of the cardiac ventricular action potential. ii. afterdepolarizations, triggered activity, and potentiation. *Circulation Research*, 74(6):1097–1113, 1994.

[83] A. Mahajan, Y. Shiferaw, D. Sato, A. Baher, R. Olcese, L.-H. Xie, M.-J. Yang, P.-S. Chen, J. G. Restrepo, A. Karma, et al. A rabbit ventricular action potential model replicating cardiac dynamics at rapid heart rates. *Biophysical journal*, 94(2):392–410, 2008.

[84] D. Makowiec. The heart pacemaker by cellular automata on complex networks. In *Cellular Automata*, pages 291–298. Springer, 2008.

[85] J. Malmivuo and R. Plonsey. *Bioelectromagnetism: principles and applications of bioelectric and biomagnetic fields*. Oxford University Press, 1995.

[86] S. Matsuoka, N. Sarai, S. Kuratomi, K. Ono, and A. Noma. Role of individual ionic current systems in ventricular cells hypothesized by a model study. *The Japanese journal of physiology*, 53(2):105–123, 2003.

[87] I. Menown, G. Mackenzie, and A. Adgey. Optimizing the initial 12-lead electrocardiographic diagnosis of acute myocardial infarction. *European heart journal*, 21(4):275–283, 2000.

[88] R. Modre, M. Seger, G. Fischer, C. Hintermuller, D. Hayn, B. Pfeifer, F. Hanser, G. Schreier, and B. Tilg. Cardiac anisotropy: is it negligible regarding noninvasive activation time imaging? *Biomedical Engineering, IEEE Transactions on*, 53(4):569–580, 2006.

[89] G. K. Moe, W. C. Rheinboldt, and J. Abildskov. A computer model of atrial fibrillation. *American heart journal*, 67(2):200–220, 1964.

[90] J. Nagumo, S. Arimoto, and S. Yoshizawa. An active pulse transmission line simulating nerve axon. *Proceedings of the IRE*, 50(10):2061–2070, 1962.

[91] P. Nielsen, I. Le Grice, B. Smaill, and P. Hunter. Mathematical model of geometry and fibrous structure of the heart. *Am. J. Physiol*, 260(29):H1365–H1378, 1991.

[92] D. Noble, S. Noble, G. Bett, Y. Earm, W. Ho, and I. So. The role of sodium-calcium exchange during the cardiac action potentiala. *Annals of the New York Academy of Sciences*, 639(1):334–353, 1991.

[93] D. Noble, A. Varghese, P. Kohl, and P. Noble. Improved guinea-pig ventricular cell model incorporating a diadic space, ikr and iks, and length- and tension-dependent processes. *The Canadian journal of cardiology*, 14(1):123–134, 1998.

[94] C. Nordin. Computer model of membrane current and intracellular ca2+ flux in the isolated guinea pig ventricular myocyte. *American Journal of Physiology-Heart and Circulatory Physiology*, 34(6):2117–2136, 1993.

[95] H. S. Oster, B. Taccardi, R. L. Lux, P. R. Ershler, and Y. Rudy. Electrocardiographic imaging noninvasive characterization of intramural myocardial activation from inverse-reconstructed epicardial potentials and electrograms. *Circulation*, 97(15):1496–1507, 1998.

[96] S. V. Pandit, R. B. Clark, W. R. Giles, and S. S. Demir. A mathematical model of action potential heterogeneity in adult rat left ventricular myocytes. *Biophysical Journal*, 81(6):3029–3051, 2001.

[97] A. V. Panfilov. Spiral breakup as a model of ventricular fibrillation. *Chaos: An Interdisciplinary Journal of Nonlinear Science*, 8(1):57–64, 1998.

[98] M. Potse, B. Dubé, J. Richer, A. Vinet, and R. M. Gulrajani. A comparison of monodomain and bidomain reaction-diffusion models for action potential propagation in the human heart. *Biomedical Engineering, IEEE Transactions on*, 53(12):2425–2435, 2006.

[99] S. F. Pravdin, V. I. Berdyshev, A. V. Panfilov, L. B. Katsnelson, O. Solovyova, and V. S. Markhasin. Mathematical model of the anatomy and fibre orientation field of the left ventricle of the heart. *Biomedical engineering online*, 54(12):21, 2013.

[100] J. L. Puglisi and D. M. Bers. Labheart: an interactive computer model of rabbit ventricular myocyte ion channels and ca transport. *American Journal of Physiology-Cell Physiology*, 281(6):C2049–C2060, 2001.

[101] A. Pullan, D. Paterson, and F. Greensite. Non-invasive imaging of cardiac electrophysiology. *Philosophical Transactions: Mathematical, Physical and Engineering Sciences*, pages 1277–1286, 2001.

[102] A. J. Pullan, L. K. Cheng, and M. L. Buist. *Mathematically modelling the electrical activity of the heart: from cell to body surface and back again.* World Scientific, 2005.

[103] B. Rodríguez, B. M. Tice, J. C. Eason, F. Aguel, and N. Trayanova. Cardiac vulnerability to electric shocks during phase 1a of acute global ischemia. *Heart Rhythm*, 1(6):695–703, 2004.

[104] B. Rodriguez, N. Trayanova, and D. Noble. Modeling cardiac ischemia. *Annals of the New York Academy of Sciences*, 1080(1):395–414, 2006.

[105] J. M. Rogers and A. D. McCulloch. A collocation-galerkin finite element model of cardiac action potential propagation. *Biomedical Engineering, IEEE Transactions on*, 41(8):743–757, 1994.

[106] M. H. Rosner, W. J. Brady Jr, M. P. Kefer, and M. L. Martin. Electrocardiography in the patient with the wolff-parkinson-white syndrome: diagnostic and initial therapeutic issues. *The American journal of emergency medicine*, 17(7):705–714, 1999.

[107] B. J. Roth. Electrical conductivity values used with the bidomain model of cardiac tissue. *IEEE transactions on bio-medical engineering*, 44(4):326–328, 1997.

[108] F. B. Sachse. *Computational Cardiology*. Springer, 2005.

[109] H. I. Saleheen and K. T. Ng. New finite difference formulations for general inhomogeneous anisotropic bioelectric problems. *Biomedical Engineering, IEEE Transactions on*, 44(9):800–809, 1997.

[110] K. J. Sampson and C. S. Henriquez. Electrotonic influences on action potential duration dispersion in small hearts: a simulation study. *American Journal of Physiology-Heart and Circulatory Physiology*, 289(1):H350–H360, 2005.

[111] T. SANO, N. TAKAYAMA, and T. SHIMAMOTO. Directional difference of conduction velocity in the cardiac ventricular syncytium studied by microelectrodes. *Circulation research*, 7(2):262–267, 1959.

[112] O. H. Schmitt. Biological information processing using the concept of interpenetrating domains. In *Information processing in the nervous system*, pages 325–331. Springer, 1969.

[113] G. Seemann, F. B. Sachse, D. L. WEIß, and O. DÖSSEL. Quantitative reconstruction of cardiac electromechanics in human myocardium. *Journal of cardiovascular electrophysiology*, 14(s10):S219–S228, 2003.

[114] D. Shepard. A two-dimensional interpolation function for irregularly-spaced data. In *Proceedings of the 1968 23rd ACM national conference*, pages 517–524. ACM, 1968.

[115] K. Simelius, J. Nenonen, and M. Horacek. Modeling cardiac ventricular activation. *International Journal of Bioelectromagnetism*, 3(2):51–58, 2001.

[116] O. Skipa, M. Nalbach, and O. Dössel. The effect ok cardiac anisotropy on the reconstruction of transmembrane voltages in the heart. *Biomedizinische Technik/Biomedical Engineering*, 48(s1):472–473, 2003.

[117] C. Stevens, E. Remme, I. LeGrice, and P. Hunter. Ventricular mechanics in diastole: material parameter sensitivity. *Journal of biomechanics*, 36(5):737–748, 2003.

[118] J. G. Stinstra, S. Shome, B. Hopenfeld, and R. S. MacLeod. Modelling passive cardiac conductivity during ischaemia. *Medical and Biological Engineering and Computing*, 43(6):776–782, 2005.

[119] D. Swenson, J. Stinstra, B. Burton, K. Aras, L. Healy, and R. MacLeod. Evaluating the effects of border zone approximations with subject specific ischemia models. In *World Congress on Medical Physics and Biomedical Engineering, September 7-12, 2009, Munich, Germany*, pages 1680–1683. Springer, 2010.

[120] B. Taccardi, B. B. Punske, F. Sachse, X. Tricoche, P. Colli-Franzone, L. F. Pavarino, and C. Zabawa. Intramural activation and repolarization sequences in canine ventricles. experimental and simulation studies. *Journal of electrocardiology*, 38(4):131–137, 2005.

[121] D. Tang, C. Yang, T. Geva, and J. Pedro. Patient-specific mri-based 3d fsi rv/lv/patch models for pulmonary valve replacement surgery and patch optimization. *Journal of biomechanical engineering*, 130(4):041010, 2008.

[122] K. Ten Tusscher, D. Noble, P. Noble, and A. Panfilov. A model for human ventricular tissue. *American Journal of Physiology-Heart and Circulatory Physiology*, 286(4):H1573–H1589, 2004.

[123] K. H. ten Tusscher, A. Mourad, M. Nash, R. H. Clayton, C. P. Bradley, D. J. Paterson, R. Hren, M. Hayward, A. V. Panfilov, and P. Taggart. Organization of ventricular fibrillation in the human heart: experiments and models. *Experimental physiology*, 94(5):553–562, 2009.

[124] K. H. Ten Tusscher, A. V. Panfilov, et al. Organization of ventricular fibrillation in the human heart. *Circulation research*, 100(12):e87–e101, 2007.

[125] N. Trayanova, J. Eason, and F. Aguel. Computer simulations of cardiac defibrillation: a look inside the heart. *Computing and Visualization in Science*, 4(4):259–270, 2002.

[126] N. A. Trayanova. Whole-heart modeling applications to cardiac electrophysiology and electromechanics. *Circulation Research*, 108(1):113–128, 2011.

[127] L. Tung. *A bi-domain model for describing ischemic myocardial dc potentials.* PhD thesis, Massachusetts Institute of Technology, 1978.

[128] F. Vadakkumpadan, H. Arevalo, A. J. Prassl, J. Chen, F. Kickinger, P. Kohl, G. Plank, and N. Trayanova. Image-based models of cardiac structure in health and disease. *Wiley Interdisciplinary Reviews: Systems Biology and Medicine*, 2(4):489–506, 2010.

[129] M. Valderrábano. Influence of anisotropic conduction properties in the propagation of the cardiac action potential. *Progress in biophysics and molecular biology*, 94(1):144–168, 2007.

[130] S. J. H. Vander A. J. and L. D. S. *Human Physiolog.* McGraw-Hill New York, NY;, 2000.

[131] F. J. Vetter and A. D. McCulloch. Three-dimensional analysis of regional cardiac function: a model of rabbit ventricular anatomy. *Progress in biophysics and molecular biology*, 69(2):157–183, 1998.

[132] E. J. Vigmond and C. Clements. Construction of a computer model to investigate sawtooth effects in the purkinje system. *Biomedical Engineering, IEEE Transactions on*, 54(3):389–399, 2007.

[133] J. Weiss and K. I. Shine. Extracellular k+ accumulation during myocardial ischemia in isolated rabbit heart. *Am J Physiol*, 242(4):H619–H628, 1982.

[134] J. N. Weiss, N. Venkatesh, and S. T. Lamp. Atp-sensitive k+ channels and cellular k+ loss in hypoxic and ischaemic mammalian ventricle. *The Journal of physiology*, 447(1):649–673, 1992.

[135] N. Wiener and A. Rosenblueth. The mathematical formulation of the problem of conduction of impulses in a network of connected excitable elements, specifically in cardiac muscle. *Archivos del instituto de Cardiología de México*, 16(3):205–265, 1946.

[136] R. Winslow, D. Scollan, A. Holmes, C. Yung, J. Zhang, and M. Jafri. Electrophysiological modeling of cardiac ventricular function: from cell to organ. *Annual review of biomedical engineering*, 2:119, 2000.

[137] R. L. Winslow, P. Helm, W. Baumgartner, S. Peddi, T. Ratnanather, E. McVeigh, and M. I. Miller. Imaging-based integrative models of the heart: Closing the loop between experiment and simulation. In *'In Silico'Simulation of Biological Processes: Novartis Foundation Symposium 247*, pages 129–143. Wiley Online Library, 2002.

[138] R. L. Winslow, J. Rice, S. Jafri, E. Marban, and B. O'Rourke. Mechanisms of altered excitation-contraction coupling in canine tachycardia-induced heart failure, ii model studies. *Circulation Research*, 84(5):571–586, 1999.

APPENDIX A

REGISTERATION AND TRANSLATION

We use quaternion based algorithm for actual rotation of target geometry. In this algorithm, we first try to minimize the Euclidean distance of geometries maximum points on a definite axis $\vec{U} = (\vec{U_x}, \vec{U_y}, \vec{U_z})$ by rotation of target geometry by $\theta = 2$ angle steps. The unit rotation quaternion for rotation of θ angle through $\vec{U}$ axis is defined as:

$$q_R = [\cos(\frac{\pi\theta}{2}) \;\; \sin(\frac{\pi\theta}{2})U_x \;\; \sin(\frac{\pi\theta}{2})U_y \;\; \sin(\frac{\pi\theta}{2})U_z]^t \tag{A.1}$$

Let unit $\vec{q_R}$ be defined as $q_R = [q_0 \;\; q_1 \;\; q_2 \;\; q_3]^t$. The rotation matrix generated by unit quaternion is then given as:

$$R = \begin{bmatrix} q_0^2 + q_1^2 - q_2^2 - q_3^2 & 2(q_1q_2 - q_0q_3) & 2(q_1q_3 + q_0q_2 \\ 2(q_1q_2 + q_0q_3) & q_0^2 + q_2^2 - q_1^2 - q_3^2 & 2(q_2q_3 - q_0q_1) \\ 2(q_1q_3 - q_0q_2) & 2(q_2q_3 + q_0q_1) & q_0^2 + q_3^2 - q_1^2 - q_2^2 \end{bmatrix} \tag{A.2}$$

If we define the translation matrix as $\vec{q_t} = [q_4 \;\; q_5 \;\; q_6]^t$, the overall registration vector will be $\vec{q} = [\vec{q_r}|\vec{q_t}]$. Let $P^o = \{\vec{P_i^o}\}$, be nodes on reference geometry, and to be in alignment with $\vec{P^{t_2}} = \{\vec{P_i^{t_2}}\}$ on target points set, where the number of two point sets are the same and index of points are in correlation with each other. We should minimize the mean of error square with:

$$f(\vec{q}) = \frac{1}{N_{p^o}} \sum_{i=1}^{Np^o} \left\| \vec{P_i^{t_2}} - R(\vec{q_r})\vec{p_i^o} - \vec{q_t} \right\|^2 \tag{A.3}$$

To minimize it, we calculate cross covariance of two point sets using:

$$\sum_{px} = \frac{1}{N_{p^o}} \sum [\vec{p_i^o} \vec{p_i^{t_2}}] - \vec{C_{p^o}} \vec{C_{P^{t_2}}} \tag{A.4}$$

where $\vec{C_{p^o}}$, and $\vec{C_{P^{t_2}}}$ are body mass index of reference and target geometries and can be obtained using (3.34).
Then an anti-symmetric matrix of $A_{ij} = [\sum_{px} - \sum_{px}^{t}]_{ij}$ is used to generate a column vector of $\Delta = [A_{23}\ A_{31}\ A_{12}]$, that itself lead to form a symmetric matrix as:

$$Q(\sum_{px}) = \begin{bmatrix} tr(\sum_{px}) & \Delta^T \\ \Delta & \sum_{px} + \sum_{px}^{T} - tr(\sum_{px}) I_3 \end{bmatrix} \tag{A.5}$$

where I_3 is identity matrix. The unit rotational quaternion q_r corresponding with maximum eigenvalue of $Q(\sum_{px})$ is desired rotation. Accordingly, an optimal translation can be calculated as:

$$\vec{q_t} = \vec{C_{P^{t_2}}} - R(\vec{q_r})\vec{C_{p^o}} \tag{A.6}$$